On the Multiscale, Mechanical Behaviors
of
Mineralized Bone

vorgelegt von
Jong Seto
aus Los Angeles, Kalifornien, Vereinigte Staaten

Von der Fakultät III- Prozesswissenschaften
der Technischen Universität Berlin
zur Erlangung des akademischen Grades
Doktor der Ingenieurwissenschaften
-Dr.-Ing.-

genehmigte Dissertation

Promotionsausschuss:

Vorsitzender: Prof. Dr.-Ing. Frank-Juergen Methner
Gutachter: Prof. Dr. rer nat. Peter Fratzl
Gutachter: Prof. Dr. rer nat. Leif-Alexander Garbe
Gutachter: Prof. Dr. rer nat. Roland Lauster

Tag der wissenschaftlichen Aussprache: 19.04.2010

Berlin 2010
D 83

"*It takes all the running you can do to keep in the same place*"

-Red Queen in Lewis Carroll's *Through the Looking Glass*

"*Revolution ist nicht ein kurzer Akt, wo mal irgendwas geschieht und dann ist alles anders. Revolution ist ein langer komplizierter Prozess, wo der Mensch anders werden muss.*"

-Rudi Dutschke

To Mom, Dad, and the Songs—for keeping up with me from the start.

Abstract

Nature has fashioned mineralized tissues into every imaginable morphology—possessing abilities that allow either for tremendous toughness, extreme extensibility, or superior strength—enabling organisms use of these devices to endure in ever-changing environments. The origins of these extraordinary properties in these materials are an outcome of the composition and organization of constituent elements into an integrated, functional tissue. The prevailing theme of this work is to delineate these structure-function relationships across multiple length-scales in mineralized tissues, specifically in the hierarchically structured bone. Through use of in situ micro-mechanical characterization coupled with X-ray scattering and diffraction techniques, processes that occur during mechanical deformation, from the molecular scale to the tissue level, are investigated in bone.

The material bone is a biological composite structured in a hierarchical manner to provide ever so distinct materials properties at every length-scale. In its arrangement, weak elements are shielded from high loads by organizing weak elements within stronger elements. Bone compartmentalizes weak components of the material such that mechanical loads are distributed disproportionately throughout the tissue, enabling stronger elements to assume more mechanical stress than its weaker counterparts. Specifically, the distribution of stress from the tissue to the mineral platelets is found in this work to be highly dependent on the various hierarchical structuring schemes employed at these different length-scales. A vital component of this hierarchical structuring is the inclusion of oriented, weak interfaces at every length-scale, serving to increase the amount of compliance between the hard and soft elements. The orientation of these weak interfaces is crucial in regulating excess strains especially at the micro-scale, where weak interfaces contribute to large degrees of mechanical anisotropy found in the elastic modulus and strength. These design schemes enable bone to minimize tissue density while retaining its characteristic materials properties.

In utilizing genetically modified mice models, localized dysfunction are introduced and studied to determine the mechanisms in which skeletal disease affects the normal strengthening schemes in bone. In investigating the micro- and the nano- structural properties of these genetically modified samples, the mineral, cellular components, or organic matrix are probed and comparatively studied with non-diseased analogs. Specifically, this work examines Schnurri (Shn3), Neurofibromatosis-1 (NF1), and α-HS glycoprotein (Ahsg) mice models—models that have disrupted mineralization phenotypes. By investigating the structural properties of murine bone under conditions of disease, the mechanisms of degeneration in bone can be elucidated.

Bone is a complex tissue—undergoing growth and development as well as maintaining homeostasis in an environment that is constantly under mechanical loading. Whether it is in tension or compression, Nature has developed strategies to distribute excess mechanical stress to the diverse structures that are found throughout the hierarchical structured tissue, from the level of the tissue- to the nano- scales. By elucidating these mechanisms that prevent catastrophic material failure in bone tissue, insights into the structural origins of properties in the material bone like strength and toughness can be revealed.

Zusammenfassung

Die Natur bildet eine Reihe von mineralisierten Geweben mit verschiedenster Morphologie. Diese Materialien weisen eine enorme Zähigkeit, große Dehnbarkeit oder große Festigkeit auf und behalten diese auch bei veränderlichen Umgebungsbedingungen. Diese außergewöhnlichen Eigenschaften sind ein Ergebnis der Zusammensetzung und der Organisation von Elementen in ein einheitliches, funktionelles Gewebe.

Das Ziel dieser Arbeit ist es, Beziehungen von Struktur und Funktion über mehrere Längenskalen in mineralisierten Geweben -speziell im hierarchisch aufgebauten Knochen- aufzeigen. Durch Kombination von Röntgenstreuung mit mikromechanischen in-situ Charakterisierungsmethoden werden Prozesse untersucht, die während der mechanischen Deformation im Knochen ablaufen.

Knochen ist ein hierarchisch strukturierter, biologischer Verbundwerkstoff, der verschiedene Materialeigenschaften auf unterschiedlichen Längenskalen aufweist. Durch die spezielle Anordnung von Elementen mit geringerer und hoher Festigkeit, können weichere Elemente gegenüber hohen Lasten abgeschirmt werden. Diese Anordnung ermöglicht es, mechanische Lasten ungleichmäßig im Gewebe zu verteilen, d.h. festere Elemente nehmen eine höhere mechanische Belastung auf als die weniger festen Elemente. Besonders die Lastübertragung von der organischen Matrix auf die Mineralplättchen ist stark von den verschiedenen Charakteristiken der hierarchischen Strukturierung abhängig. Ein grundlegender Bestandteil dieser hierarchischen Strukturierung sind orientierte, schwache Schnittstellen auf jeder Stufe der Längenskala, die die Nachgiebigkeit zwischen den harten und weichen Elementen vergrößern. In der Arbeit konnte gezeigt werden, dass die Orientierung dieser schwachen Schnittstellen bei der Regulierung von Überbeanspruchungen insbesondere auf der Mikroskala entscheidend ist. Dort tragen diese schwachen Schnittstellen zu großer mechanischer Anisotropie bei, die im Elastizitätsmodul und der Kraft repräsentiert ist. Ein andere Untersuchung zeigt, dass sich bei makroskopischer Deformation die jeweiligen Dehnungswerte nacheinander in Richtung kleinerer Längenskalen im Knochen (Gewebe → organische Matrix → Mineralplättchen) vermindern. Dieses Designprinzip ermöglicht Knochen die Gewebedichte zu minimieren während die charakteristischen Materialeigenschaften unverändert bleiben.

In dieser Arbeit werden auch genetisch veränderte Maus-Modelle mit Funktionsstörungen untersucht um die Mechanismen der Mineralisierung und die Ausbildung der Knochenfestigkeit bei Skelett-Krankheiten zu verstehen. Es werden die Mikro- und Nano-Strukturen dieser genetisch veränderten Proben untersucht, wobei die Mineral- und Zellbestandteile sowie die organische Matrix mit gesunden Referenzproben verglichen werden. In der vorliegenden Arbeit werden Schnurri (Shn3), Neurofibromatosis-1 (NF1), und α-HS Glycoprotein (Ahsg) Maus-Modelle untersucht, bei denen der Prozess der Mineralisation gestört ist. Auf der Materialebene zeigen sich keine signifikanten Unterschiede in den Eigenschaften, was zum Schluss führt dass diese Mechanismen der Mineralisierung und die Ausbildung der Knochenfestigkeit sehr komplex sind.

Knochen ist ein komplexes Gewebe, unterliegt ständigem Wachstum und muss die Mineralhomöostase in einer Umgebung aufrecht erhalten, die sich unter dauerhafter mechanischer Belastung befindet. Die Natur hat Strategien entwickelt, um mechanische Überbelastung auf verschiedenen Sub-Strukturen zu verteilen, die überall im hierarchisch strukturierten Gewebe wiedergefunden werden können. Durch ein besseres Verständnis dieses Prinzips kann aufgeklärt werden, in welchen Strukturelementen die Ursprünge für die vielseitigen Knocheneigenschaften liegen.
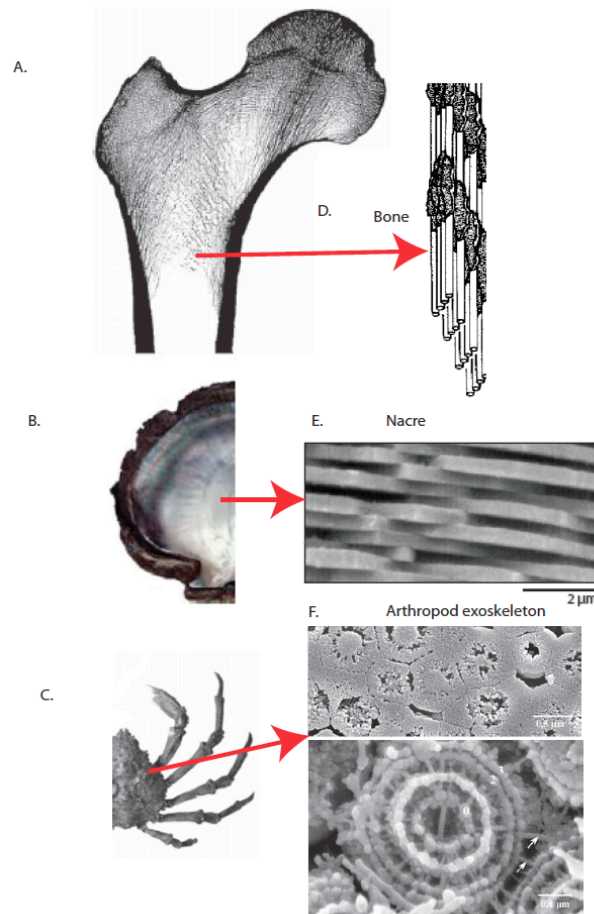
Table of Contents

1   Introduction

Hierarchical structures in mineralized tissues enable a synergistic co-existance of the biological and materials worlds—the ability to construct and adapt tissues via cell processes while retaining the necessary materials and mechanical properties to be

Figure 1.1 Hierarchical structures in mineralized tissues (A.) Bone (B.) Nacre (C.) Arthropod cuticle (D.) Oriented arrangement of the collage fibers and mineral platelets in bone along main loading direction (E.) Stacking of calcium carbonate mineral along a specific crystallographic axis in nacre (F.) Plywood arrangement of a chitin-protein matrix in arthopod cuticle [(A.) adapted from Huiskies J. Anat. 2000, (B.) and (E.) adapted from Ji and Gao Prog. Mat. Sci. 2010, (C.) adapted from Meyer et al. Prog. Mat. Sci. 2008, (D.) from Landis Conn Tiss Res 1996, (F.) from Fabritius et al. JSB 2005].

functional. The schemes utilized in structuring mineralized tissues are diverse and often vary from one length-scale to another. However, the common theme found in hierarchial structured mineralized tissues is their ability to undergo processes of growth and development, a process lacking in all synthetic materials.

Several examples of mineralized tissues with various strategies of hierarchical structuring are presented in **Figure 1.1**. From bone to nacre, each design strategy used in the observed tissues is best suited for a specific function. In the case of bone, mechanical loads are always directed along its longitudinal axis. At the nano-scale, the material bone is composed of a highly aligned organic matrix composed primarily of collagen and nano-scale mineral platelets arranged along this main loading axis. The orientation and arrangement of both the mineral and organic components enables the tissue to effectively resist the applied loads (**Figure 1.1(D.)**). Unlike bone, a brick-and-mortar structure of calcium carbonate mineral is found in nacre. The organizational scheme employed in nacre is such that the hard brick-like calcium carbonate mineral is stacked along a specific crystallographic axis with alternating soft layers of an organic matrix (**Figure 1.1(E.)**). Also utilizing calcium carbonate mineral, the arthropod exoskeleton is structured by a mineralized organic matrix composed of chitinaceous-protein components. This organic component is organized in a plywood structure with the ability to further structure itself in a layer-by-layer arrangement. Each chitin-protein fibril is reinforced by calcium carbonate by embedding mineral throughout its plywood structure (**Figure 1.1(F.)**). From these select tissues, bone will be the material of primary focus due to its complexity and relevance. In the following paragraphs, a primer on bone and its mechanical behavior is briefly presented.

1.1   Bone

Endoskeletons found in mammals are composed of bone and tissues that connect them. Unlike the exoskeletons found in arthropods, endoskeletons have evolved ways to compartmentalize forces—mechanisms to direct forces to specific components in the skeleton. Specifically, examining our own bones, two main types of bones are found: (1.) Cancellous bone (2.) cortical bone (**Figure 1.2**) [1] [2] [3] . Cancellous bone is a porous

Compact bone
(Osteon, Haversian system)

Osteon

Cement line

Haversian canal

Concentric lamellae

Collagen fibers

Resorption cavities

Interstitial lamellae

Periosteal vessel

Lacuna

Canaliculi

Inner circumferential lamellae

Cancellous bone (Trabeculae)

Outer circumferential lamellae

Volkmann's canal

Concentric lamellae
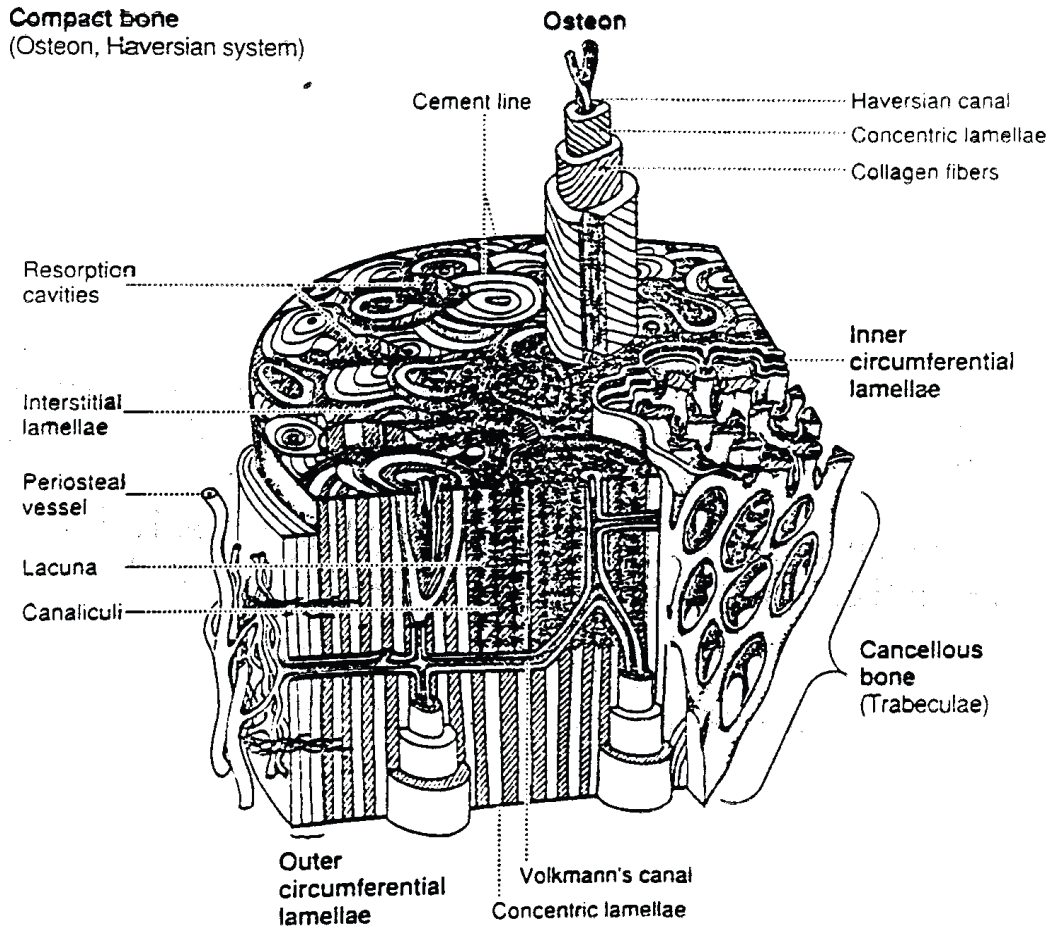
Figure 1.2. A cross-section of the structure of fully developed adult long bone. Of note are the spatial differences as well as the morphological and orientational differences between compact and cancellous bone. Specifically, compact bone is the main load bearing bone type and is typically found in regions of high load, the periphery. This differs to cancellous bone which is more porous and strut-like and found on the endosteal side of tissue as well as at the heads of long bones. [Adapted from Currey Bones 2002].

structure that are found in joints and the "round" bones. The characteristic "strut-like" structure in cancellous bone is directed in orientations where there is a mechanical stimulus. This enables for a type of material that is able to resist loads in specific loading directions and be less dense as a result of the innate porosity in the tissue. This type of structure is witnessed throughout Nature and appropriately termed "cellular solids" due to their associated biological function [2]. This porosity in cancellous bone is important since it allows biological processes to occur in these spaces, like the chondrocyte acitivity in the growth plate enabling for longitudinal bone growth. This differs to the dense tissue

found in cortical bone. Cortical bone is composed of dense mineralized material in the mid-shaft of long bones and maintains a characteristic oriented collagen fiber matrix typically aligned to the main loading axis. The two types of bones, cancellous and compact bones, are different structurally, but occupy similar roles in maintaining mechanical homeostasis. In the following chapters, an in depth investigation of these mechanisms utilized in regulating the mechanical behaviors in cortical bone will be examined.

1.2 Primer on Bone Mechanics

Precise measurements of whole bone materials properties have been performed by many groups for decades to evaluate the behavior of the tissue to specific loads—from simple uni-axial tension and compression to three- and four- point bending measurements [4-8] [9-11]. From these experiments on bone, characteristic materials properties like its strength, the amount of stress the tissue is able to withstand without failure, is determined under different modes of loading such as compression, tension, as well as shear (**Table 1.1**). Another characteristic materials property of a material is its strain, the amount of displacement occurring in the tissue before failure. In bone, whether it is loading via compression or tension, the initial stress- strain relationship is described as part of a

Table 1-1 Strength in Bone. A comparison of strength values from whole human and bovine bones under various modes of mechanical loading. [Cowin and Doty Tissue Mechanics 2006]

Ultimate Strength (MPa)	Human	Bovine
Tensile	133	156
Compressive	195	237
Shear	69	73

Table 1-2 Elastic Modulus in Bone. Comparing the elastic moduli from different modes of mechanical testing on whole human and bovine bones. [Cowin Bone Mechanics Handbook 2001]

Elastic Modulus (GPa)	Human	Bovine
Longitudinal	17.4	20.4
Transverse	9.6	11.7
Bending	14.8	19.9
Shear	3.51	4.14
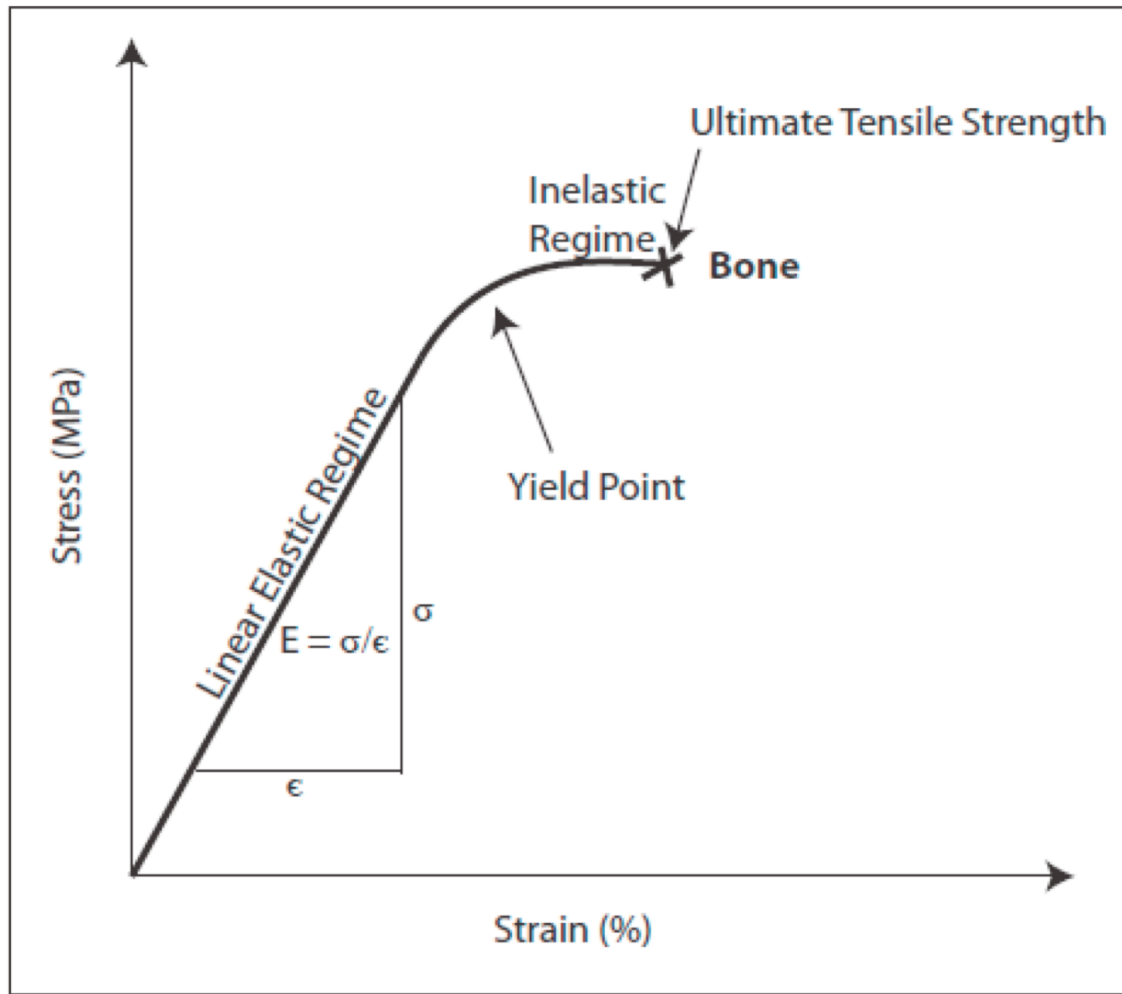
Figure 1.3 Understanding the components of bone's materials properties From this idealized stress-strain plot of bone under tension, several materials properties can be analyzed and obtained such as the elastic modulus (E), ultimate tensile strength (UTS), and yield point.

linear elastic regime. During this regime, stress and strain are proportional, the stress applied to the tissue results with a proportional increase in its strain and this behavior is reversible. This stress-strain relationship is defined by a value known as the modulus of elasticity, also termed Young's modulus. The elastic modulus $E = \dfrac{\sigma}{\varepsilon}$, where σ is the stress and ε is the strain, such that each material has a characteristic elastic modulus (**Table 1.2**). When increasing stress or strain beyond the linear elastic regime, a threshold is reached to signify the start of the inelastic deformation regime in bone. This point is referred to as the yield point. When inelastic deformation occurs in the tissue, permanent damage in the material bone develops. By increasing the stress or strain further, damage

in the material bone accumulates and eventually leads to catastrophic fracture. For simplicity sake, the following hypothetical stress-strain plot visually describes the material bone in tension and the various components of its materials and mechanical character (**Figure 1.3**).

Throughout this work, additional terms are mentioned to describe materials properties in the material bone. This includes hardness of a material which is a value that describes a material's resistance to deformation and is expressed as a force per unit area. Hardness is a versatile value that is used frequently due to its ease of measurement by way of indentation method and can be used as an estimate for other properties. Also discussed here is a material's toughness and more specifically, its relation to fracture. Toughness is the amount of strain energy required to fracture the material and is often expressed in terms of the amount of work to fracture per unit volume. Anisotropy is another term that will be used throughout this work to describe the orientation depedent behavior of a material to mechanical loading. The anisotropy is measured by a quantity dubbed the Poisson's ratio which takes measure of the transverse strain and axial strain such that the Poisson's ratio $\nu = -\dfrac{\varepsilon_{transverse}}{\varepsilon_{axial}}$.

While much has been accomplished on the mechanics of bone, recent advances in dissection and sample preparation methods enable the isolation of individual components in the hierarchical bone structure. This allows for the ability to probe the various structural constituents that make up the material bone at several length-scales. As observed in **Figure 1.3**, the mechanical behavior of bone is directly related to its composite nature—its composition as well as organization of the constituent elements. By isolating individual elements in the material bone, the contribution of these constituent elements are better understood with respect to the mechanical behavior of the tissue. In the following pages, the hierarchical structure in bone tissue will be dissected and mechanically investigated in order to assess the properties of the material bone at the micro- and nano- length-scales.

1.3 Scope of this work

As mentioned in the previous sections, biological materials incorporate a wide range of strategies to accommodate function. Whether it is the ability to build brick and mortar structures (nacre) or organized sheets of mineral (arthropod cuticle), optimized structure-function relationships are witnessed throughout these materials. In this dissertation, a focus on mineralized tissues, mainly cortical bone, their structures and mechanical behaviors will be investigated to understand the functionalities enabled by structural properties incorporated in this mineralized material by Nature.

The focus of this research presented in the subsequent chapters is an attempt to elucidate the origins of mechanical properties in mineralized tissues, specifically in cortical bone. The complexity of this work comes from the structural hierarchy that is integrated within and throughout the whole tissue. Together with its multi-component composition (organic and inorganic) and hierarchical architecture, bone tissue is able to continuously grow and develop as an organ as well as simultaneously maintaining mechanical homeostasis in the surrounding environments i.e. resisting catastrophic material damage from cyclic mechanical loading involved in daily activities of the organism. Structure is innately tied to mechanical behavior as observed in the mechanisms utilized to inhibit micro-cracks and cracks from formation and propagation at the micro-scale. Furthermore, bone is filled with cells, such as osteo- blasts, clasts, and cytes, which continually maintain and renew the bone mineral and organic matrix. All these components contribute to a structuring in the material necessary to accommodate both the biological as well as the mechanical activities. Whether these observed trends in the structure of mineralized tissues are utilized across many species is a question addressed by the systematic materials characterization discussed in later chapters. In this dissertation, the relationship of structure and materials behavior in mineralized tissues is established by the general scope of the following specific objectives:

- Establish methodologies to access the multiple structural hierarchies in mineralized tissues

- Characterize materials properties and mechanical behaviors at the meso- and nano- length-scales
- Investigate deformation behaviors of bone at the micro-scale
- Characterize non-collagenous proteins controlling materials properties in murine bone via genetic pathways
- Determine structural themes in strength and toughening mechanisms in bone

The remainder of this dissertation will examine the effects of anisotropy, structural assemblies and architecture in cortical bone with respect to materials and mechanical behaviors in tension. By investigating the mechanical behavior of mineralized tissues, the reaction of a tissue to a pre-defined mechanical force, the mechanisms which allow the tissue to circumvent permanent material damage and enable continuation of its function is probed. In combination with in-situ techniques, the effect of structure on the materials properties including the strengthening processes in mineralized tissues is fully delineated at several length-scales.

2 The material bone

Bone is a composite material composed of a phosphate mineral and an organic component, namely collagen. Unlike the properties of phosphate mineral or type I collagen alone, bone derives it's materials properties from both these constituents—it's stiffness from the mineral components and it's elasticity from the organic components. In fact, the organization of bone is diverse and widely different at every length-scale. This structuring of bone from the nano- to tissue- scales, as shown in **Figure 2.1**, is implicated in enhancing the materials properties of the tissue [1] [12]. At the nano-scale, mineral platelets that are several nanometers thick, are co-aligned with collagen fibrils (**Figure 2.1(A.)**). The mineral platelets and collagen are organized into ordered structures like mineralized collagen fibers and further structured into various structural motifs (**Figure 2.1(B.)**). Interestingly, the various structural motifs themselves organize accordingly into different tissue types. For example, in a parallel stacking arrangement of these mineralized collagen fibers, parallel-fibered arrays are created to form fiber bundles (**Figure 2.1(C.)**). Stacking of organized fiber bundles lead to lamella at a higher length-scale which is the basis of osteonal bone tissue as well as fibrolamellar bone (**Figure 2.1(D.),(E.)**). By organizing these distinct structures in combination with a diversity of constituent elements, mineral, collagen, and non-collagenous proteins, an integrated, hierarchical structured tissue is formed possessing unique materials and mechanical properties (**Figure 2.1(F.)**). In the following sections, the major components of bone are further examined and their roles in the tissue discussed.
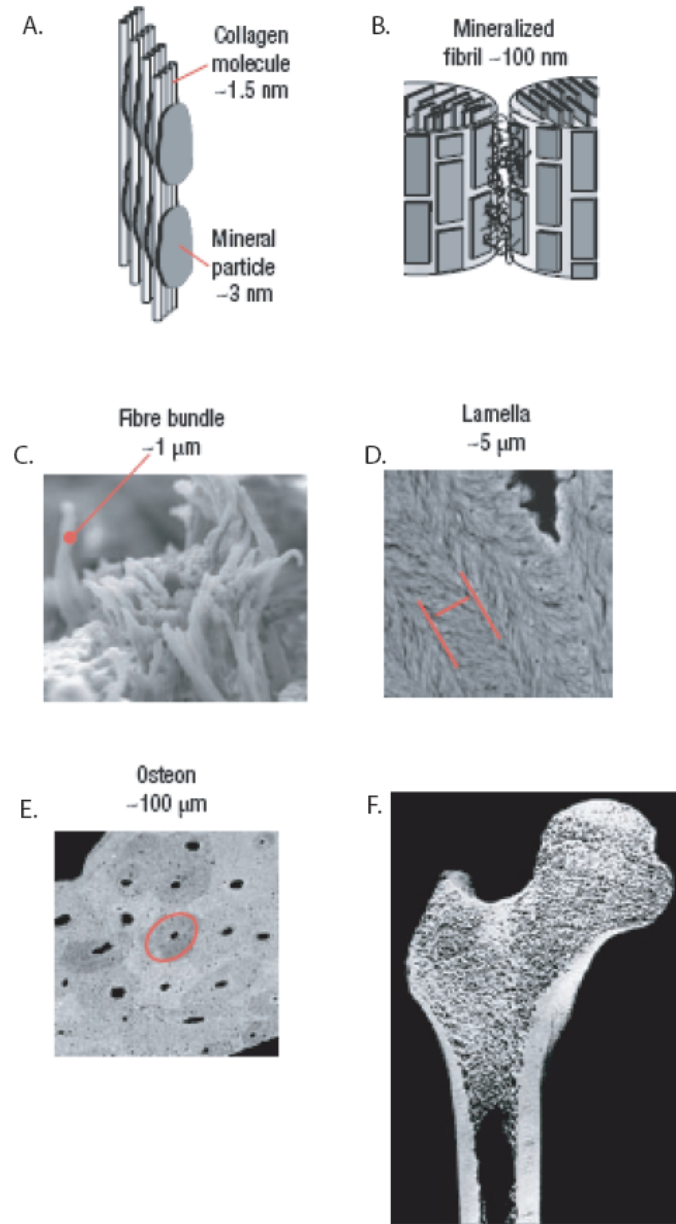
Figure 2.1 Constituents of bone from the nano- to the tissue- levels. (**A.**) Mineralized collagen fibrils are impregnated with apatite mineral platelets, both intra- and extra-fibrillarly (**B.**) The fibrils are organized to form a fiber (**C.**) The fibers themselves assemble into bundles that are arranged in distinct organizational schemes depending on the bone tissue (**D.-E.**) Lamellar and osteonal types compose the range of tissue types in cortical bone (**F.**) At the tissue level, cortical bone is distinguished by its mechanical properties [Adapted from Fratzl and Weinkamer Prog Mat Sci 2007].

2.1 Collagen: Bone at the molecular scale

At the molecular scale, collagen molecules are composed of a primary structure -Gly-X-Y- (where X-Y is any of the 20 amino acids available) whereby the most frequent sequence –Gly-Pro-Hyp- (10.5%) repeat is interspersed with other triplet sequences like -Gly-Pro-Ala-, -Gly-Ala-Hyp-, -Gly-Leu-Hyp- (3.4-5.5%), as well as -Gly-Glu-Lys-, -Gly-Pro-Lys- (2-3%) to form collagen telopeptide fragments that are roughly 11-26 residues long [13]. These small polypeptide chains, with the aid of the C-terminal specific propeptide domains in each chain, assemble into triple helical tropocollagen complexes. The various combinations of amino acids as well as the subsequent diverse supramolecular arrangements confer the structural diversity found in collagen molecules. In the case of Type I collagen, the main constituent in skin, tendon, and bone, the C-propeptide domain directs the assembly of a heterotrimer with two identical alpha helical chains and a third distinct alpha helical chain into a right-handed, triple helical agglomeration. Characteristic of this arrangement is the burying of all glycine residues within the core of the supramolecular chain. This nascent protein is termed tropocollagen [14]. From the predominant -Gly-Pro-Hyp- triplet sequence, non-polar, charge interactions that aid in the organization of the initial triple helices that is characteristic of Type 1 collagen derived tissues.

These tropocollagen complexes further assemble into longer chains to form fibrillar, procollagen chains. With the aid of cellular processing and metalloproteinases, the N- and C- terminal ends of procollagen chains are modified to produce fibrils that are spaced approximately ~67 nm periodically from each other (**Figure 2.2(A.)**). This 67 nm periodicity is the basis of the gap zones believed to be involved in the Hodge-Petruska model of mineralization in collagenous tissues [15-17]. These fibrils continue to self organize into higher levels of structures, eventually becoming tissues containing several length-scales of structural hierarchy (**Figure 2.2(B.)**). The interest in collagen's structure is due to its ability to pack efficiently, into fibrils and further into bundles as observed in bone and tendon. In addition, the assembly process of these collagenenous tissues occur in the extracellular space, whereby water and the small chain peptides associated with the extracellular matrix interact with the nascent tissues. Interestingly, a monolayer of
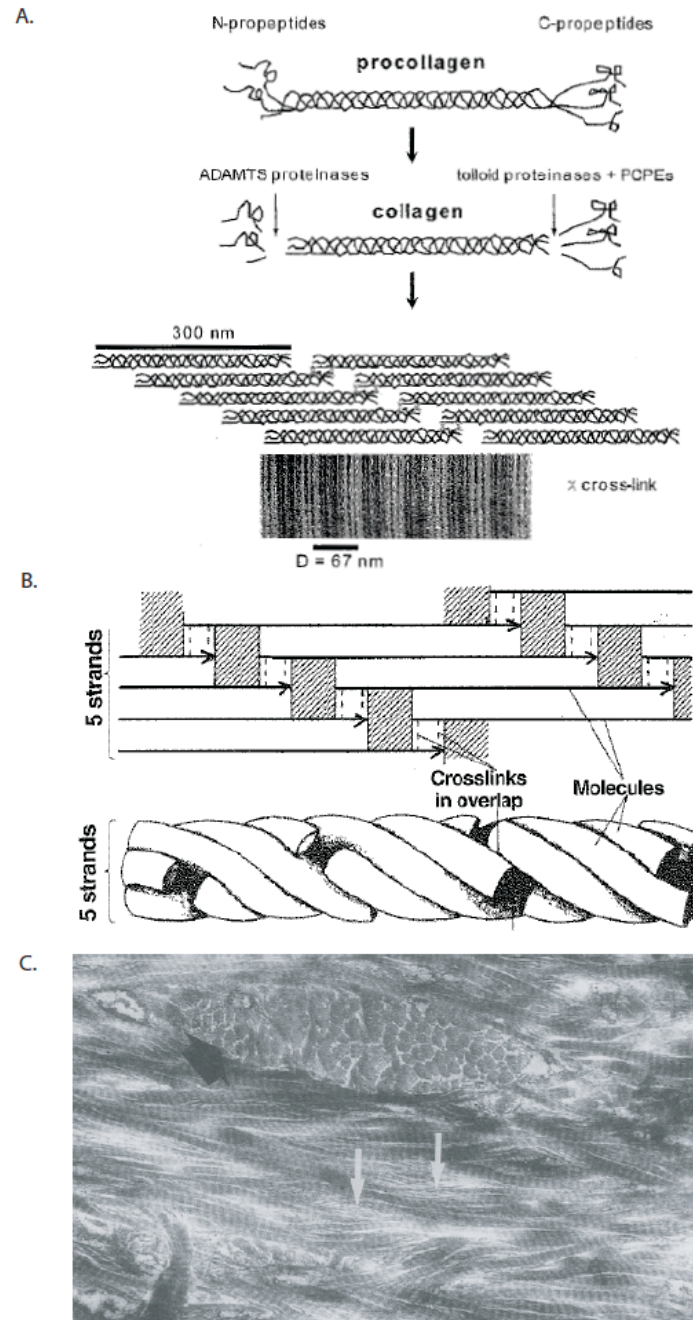
Figure 2.2 Collagen fibril formation and structure (A.) Proper formation of nascent collagen fibrils requires processing steps from proteinases and cells (B.) Organization of the fibrils in collagen fibril bundles displays the characteristic ~67 nm periodic gap spacing between fibrils (C.) After demineralization, the collagen fibrils denuded of mineral from both intra- and extra- fibrillar regions in TEM readily show the close packing nature of the fibrils as well as the 67 nm periodic stagger of the constituent collagen microfibrils (white arrows). Black arrow shows orthogonally oriented collagen fibrils indicating domains that can have abrupt variations. [(A.) and (B.) from Cowin and Doty Tissue Mechanics 2006, (C.) from Giraud-Guille Calc Tiss Int 1988].

structural water is also found to be tightly associated to the packing of the collagen fibrils. It is very likely that water is itself another stabilizing molecule in the collagen structure [18]. Furthermore, the presence of short chain peptides with glycoaminoglycans domains at the fibrillar surface enhances the inter-fibrillar and extracellular interactions as these molecules in concert (1.) provide components to improve mechanical compliance (2.) stabilize a molecular interface by interacting with the extra-cellular space and the collagen fibrils. In general, these weak interactions are effective in integrating the various components in bone, as well as bridging the constituents at the different length-scales (**Figure 2.2(C.)**).

2.2 Non-collagenous proteins: the other organic component in bone

Non-collagenous proteins (NCPs), including the aforementioned glycoproteins and proteoglycans, are as their name suggests are the proteins that comprise the rest of the organic component in bone. These molecules make up approximately 5-7% of the total protein component in bone [19], with collagen composing the rest of the organic matrix. Several NCPs are found to be extensively involved in signaling and regulatory functions, but only the structural aspects will be discussed here [20, 21].

2.2.1 Proteoglycans

Unlike collagen, proteoglycans are short-chained molecules which do not serve in any direct structural role. However, these molecules are often implicated in functionalizing substrates, mainly the ECM, and confer specific binding abilities to cells as well as to other molecules. In bone, proteoglycans are found throughout the intra- and inter-fibrillar spaces of collagen fibrils [22] [23, 24]. The general structure of a typical proteoglycan molecule is a glycosaminoglycan (GAG) moiety bonded to a protein core. The GAG component is itself diverse, containing several variations of polysaccharide arrangements and composition. A typical GAG residue contributes to the acidic, hydrophobic, and negatively charged behavior associated to proteoglycans. Furthermore, the protein core residue not only acts as a repository of GAG moieties, but also includes regions that are

able to interact and anchor to substrates such as extracellular matrices as well as cellular membranes. It is believed that the GAG and core protein moieties work in concert to determine proteoglycan functionality. This variation in both the GAG and protein moieties gives rise to a diversity of proteoglycan structures with various functionalities. For example, protein core moieties that associate with the ECM tend to have GAG residues that interact more with the extracellular elements like water and ions by way of weak electrostatic interactions, whereas the protein moieties that are located at the cell surfaces have GAG residues that able to interact with membrane proteins and cell signaling molecules to regulate processes like growth and proliferation of cells. The abundance and structural diversity of proteoglycans in bone implicates these molecules in a variety of bone-related functions. These include facilitating supramolecular organization, increasing mechanical compliance, and as well as mediating cell proliferation. Specifically, the ability of proteoglycans to modulate these activities depends on the composition of its GAG residues and protein moeities. In the following paragraphs, a brief description of two proteoglycan categories found in bone are presented.

A class of proteoglycans includes the membrane anchored proteoglycans. These proteoglycans directly bind to growth hormones and/or signaling proteins to stimulate or inhibit cellular activity and proliferation. The structural roles of these proteoglycans occur indirectly via regulating TGF-β and the FGF growth factor signaling in osteoblasts and osteoclasts. One predominant proteoglycan in this category is the heparin sulfate proteoglycan which is found on cellular membranes and binds to small growth factor molecules in bone. For the sake of brevity and relevance, the focus on membrane anchored proteoglycans will be limited and shifted to another category of proteoglycans more applicable to the structural aspects of bone, the small leucine-rich repeat proteoglycans.
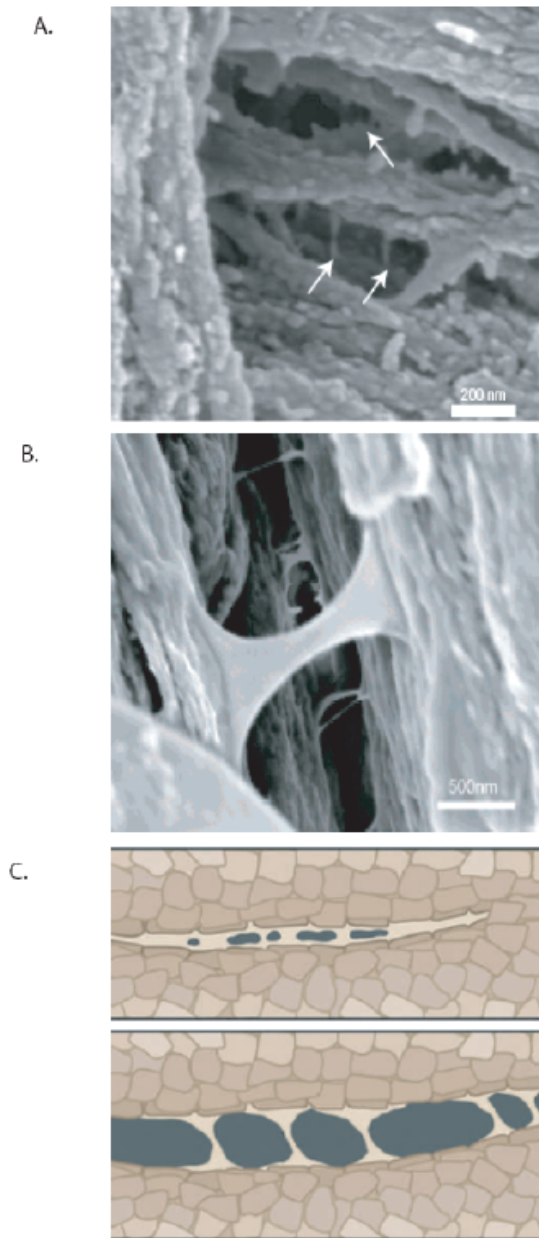
Figure 2.3 A non-collagenous protein (NCP) component comprised of over a dozen distinct proteins make up the rest of the organics in bone (A.) Many of these NCPs reside in the interfibrillar regions of the collagen fibrils (B.) These NCPs are postulated to not only nucleate mineralization, but also possess mechanical function in bone (C.) A schematic of these NCPs as sacrificial bonds inbone [(A.) and (C.) from Fantner et al. 2005, (B.) from Fantner et al. 2006)].

In the case of small leucine-rich repeat proteoglycans (SLRPs), this category is the most abundant type of proteoglycan in bone and are typically ~40 kDa with GAG residues on both the 5' and 3' ends of the protein core. Some examples of SLRPs include decorin and biglycan, both proteoglycans found associated to the extracellular matrix and participate in the organization and the development of the organic matrix in bone tissue. Specifically, decorin is found to functionalize nascent collagen fibrils to mediate

formation of fibril bundles. Similarly, in the case of biglycan where it is found to be localized to the ECM and is believed to aid in mineralization of the collagen fibrils. The absence of both decorin and biglycan have been implicated in decreased bone mass, variations in collagen fibril diameters, and importantly, reduced osteoblast cellular activity and proliferation.

2.2.2 Glycoproteins

Glycoproteins are another class of non-collagenous proteins also found in the bone matrix like proteoglycans. In comparison to the aforementioned short chain proteoglycans, these proteins are typically higher in molecular weight and have many functional groups. The functional complexity of these proteins are indicated by the additional level of regulation by kinases and phosphatases in adjusting the protein's phosphorylation state—either adding/removing a phosphate (PO_4^-), the function of these proteins are turned on/off [25]. Two major anionic glycoproteins, bone sialoprotein and osteopontin, have been found to bind to hydroxyapatite with high affinities as well as interact with osteo- blasts and clasts. In the following paragraphs, structure and function of bone sialoproteins and osteopontin will be discussed in further detail.

Bone sialoprotein

Bone sialoprotein (BSP) is a ~300 base-pair protein which has three distinctive domains- two adjacent glumatic acid domains and an RGD domain at the C-terminal end. The two glutamic acid domains themselves are very specific in function and thought to be processed differently via posttranslational modifications. One of these glutamic acid domains is directly implicated in binding to hydroxyapatite mineral, whereas the other glumatic acid domain is required to aid in recruitment of cells to recognize the RGD sequence [26]. Additionally, BSP has been found to have a high affinity to Type 1 collagen [27].

Osteopontin

The complexity of this group of proteins is inferred by the variety of functionalities attributed to these non-collagenous proteins. In addition to initial findings that bone phospho- and sailo- proteins are involved in the nucleation of mineral in bone due their specific high degree of affinities to mineral ions like Ca^{2+} and Mg^{2+} [28-30], these proteins have been found to aid in the mechanical properties of the tissue [31-33].

Osteopontin has been implicated in inter-fibrillar interactions, specifically at the interfaces between mineralized collagen fibrils [31-33], where it is believed that it is able to interact with water and small ions to mediate the shearing processes between fibrils. Furthermore, many have proposed that osteopontin, due to its the abundance as well as its ability to electrostatically interact with other molecules in the ECM, participate in a network of proteoglycan-proteoglycan interactions termed sacrificial bonding [34]. Sacrifical bonds are themselves composed of weak, interacting molecular interactions, characteristic of osteopontin interactions, are believed to modulate the mechanical compliance in bone at the molecular length-scales (**Figure 2.3**).

2.3 Mineral in bone

The mineral in bone is a hydroxylated calcium carbonated apatite found to be in nano-sized platelet form [12]. The mineral component in bone reinforces the structural organization of the collagen component. Its structural importance is observed in the presence of defect, whether it is abundance, platelet morphology, orientation, or organization, which results in mechanical dysfunction of the whole tissue [35]. The mineral platelets themselves are approximately in dimensions of ~2 nm thick x 50 nm long x 25 nm wide intercalated into the collagen fiber bundles as well found in the inter-
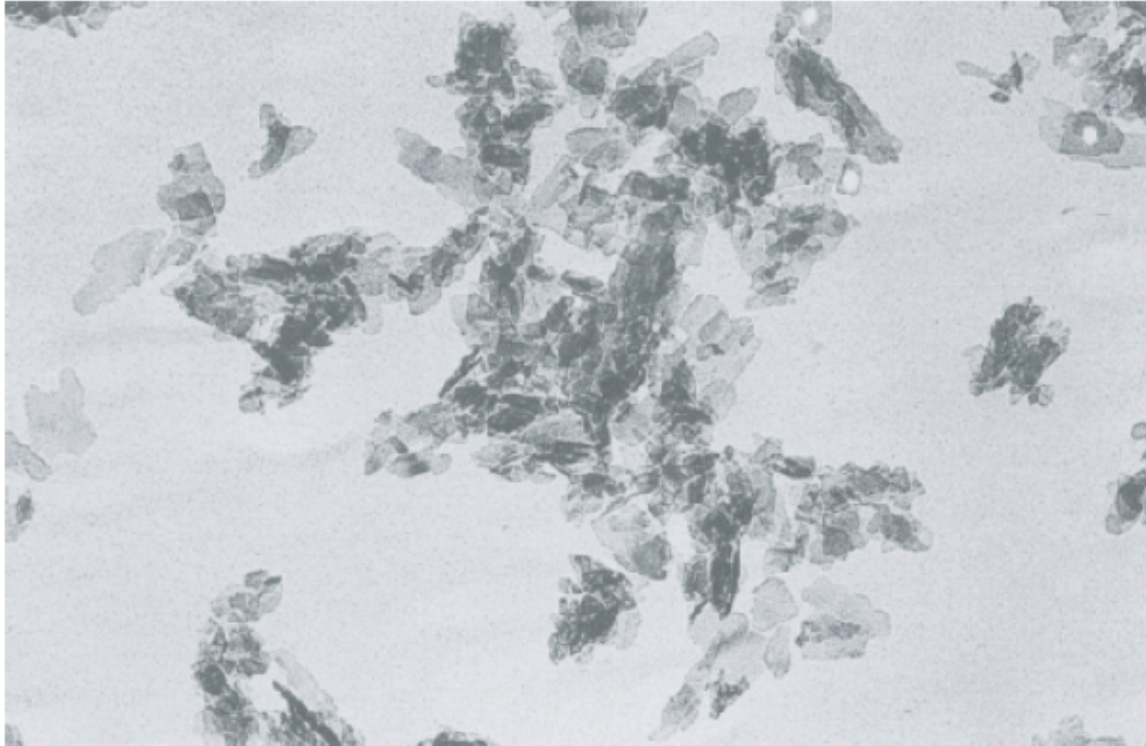
Figure 2.4 Transmission electron micrograph of the mineral component in cortical bone. By removing the mineral via an ultrasonic sonicator, the apatite mineral associated within the organic component of bone can be fractioned and is shown to have plate-like morphologies [Adapted from Weiner and Price Calc Tiss Int 1986].

fibrillar space [36-39] (**Figures 2.4, 2.5(A.)**). The organization of the mineral platelets confers much of the mechanical anisotropy found in the tissue. Additionally, the orientation of the mineral platelet is such that the length dimension is always along the longitudinal plane of the tissue or in the loading direction (**Figure 2.5(B.), (C.)**).

The structure of the mineral constituents in bone is itself a puzzle for since hydroxyapatite is natively found to form stable hexagonal crystal structures although the mineral in bone are found to be in platelet form. Many have proposed that an intermediate phase is involved in formation of the platelet morphology. Specifically, this phase is the octacalcium phosphate transition phase [40] [41-43]. The exact mechanism of mineralization is still unknown, but it is widely believed that osteoblasts secrete an amorphous mineral phase via secretory vesicles into the extracellular space and mineralization occurs by way of the octacalcium phosphate phase in the organic matrix.

A.

Mineralized collagen fibril

C axis

B.

Collagen fiber bundle

C.

Collagenous fascicle

Longitudinal axis
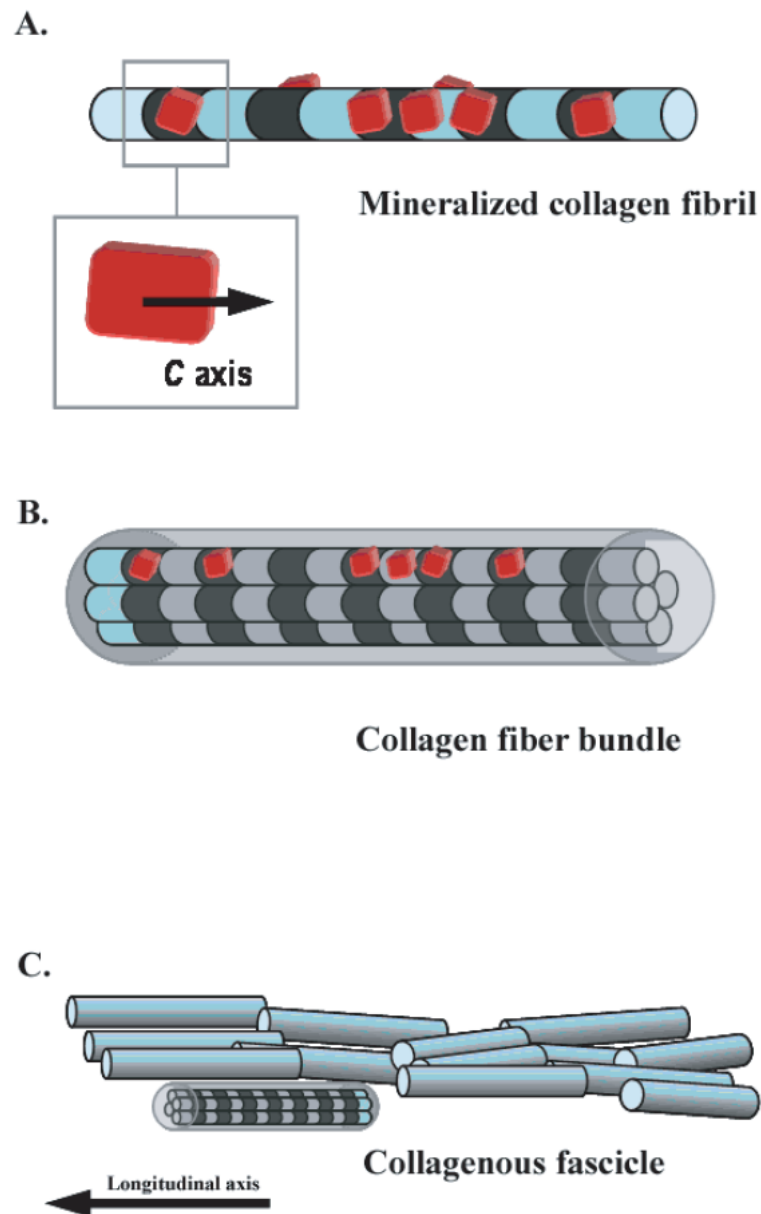
Figure 2.5 Superstructural organization of the mineral and collagen components in bone. (**A.**) Mineral nucleation and alignment occur along the collagen fibril and exist as both intra- and extra-fibrillar forms (**B.**) Mineral collagen fibrils are organized into a fiber bundle as a result of the parallel packing of the collagen fibrils (**C.**) Collagen fibers are further organized into fascicles which are oriented along a predominant axis (in bone, this is direction is the longitudinal bone axis) [Adapted from Nassif et al. Chem Mater 2010 *accepted*].

19

For mineral to enter into the intra-fibrillar spaces is itself complicated whereby passive diffusion does not adequately explain the regular and abundant mineralization that occurs throughout the organic matrix. Possibly, with the aid of proteoglycans as well as small mineral chaperones, mineral is actively transported into the intra-fibrillar space and mineralizes into the supposed octacalcium phosphate phase. Once initial mineralization does occur within the intra-fibrillar space, the nucleated platelets are inhibited from further growth due to the spatial constraints of the collagen fibrils. The seamless integration of the mineral platelets into the organic matrix forms the basis of mineralized collagen fibers. These mineralized fibers are themselves organized into various structural motifs and are further structured to produce diverse tissue types relevant for specific tasks. Some examples of these unique structures include structures like lamellar and osteonal bone, where the mineralized collagen is organized in various arrangements to form the tissue. In the next section, the various structural arrangements of mineralized collagen will be examined in more detail.

2.4 Structural motifs of mineralized collagen

At the micro-scale, diverse of structures within bone are observed (**Figure 2.6**). The versatility of mineralized collagen fibers, the structural unit cell at the micro-scale, is confirmed by the diverse uses observed in bone. This includes the formation of stent-like structures in trabecular bone as well as the plywood arrangement in osteonal bone. In this section, the organization of mineralized collagen will be discussed as well as the different bone types that arise from these structural motifs in cortical bone.
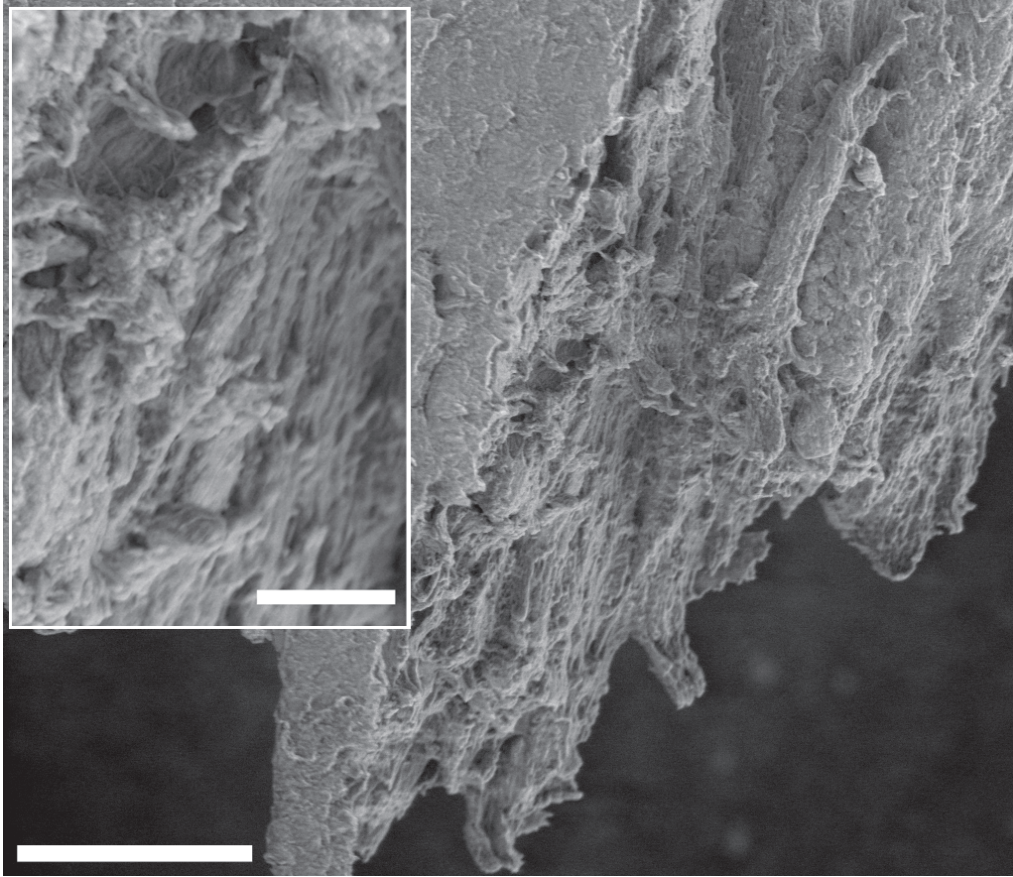
Figure 2.6 A typical bone fracture revealing the contribution from its two major constituents. Furthermore, at higher magnifications, the microstructure readily reveals the parallel fibered array of collagen and mineral. The inset shows the oriented mineralized collagen fibers. (scale bar: 5 microns (inset), 25 microns).

Specifically, the diversity of bone structures utilized demonstrates several strategies in responding to specific types of mechanical load.

2.4.1 Random stacking

At one extreme is an organization scheme incorporating the random stacking of the mineralized collagen fibers (**Figure 2.7(A.)**). The random packing of mineralized collagen fibers may initially be perceived to be mechanically inferior and often associated to pathological disease states, but random packing does increase the surface areas of mineralized collagen fibers-making more areas available for interacting with small
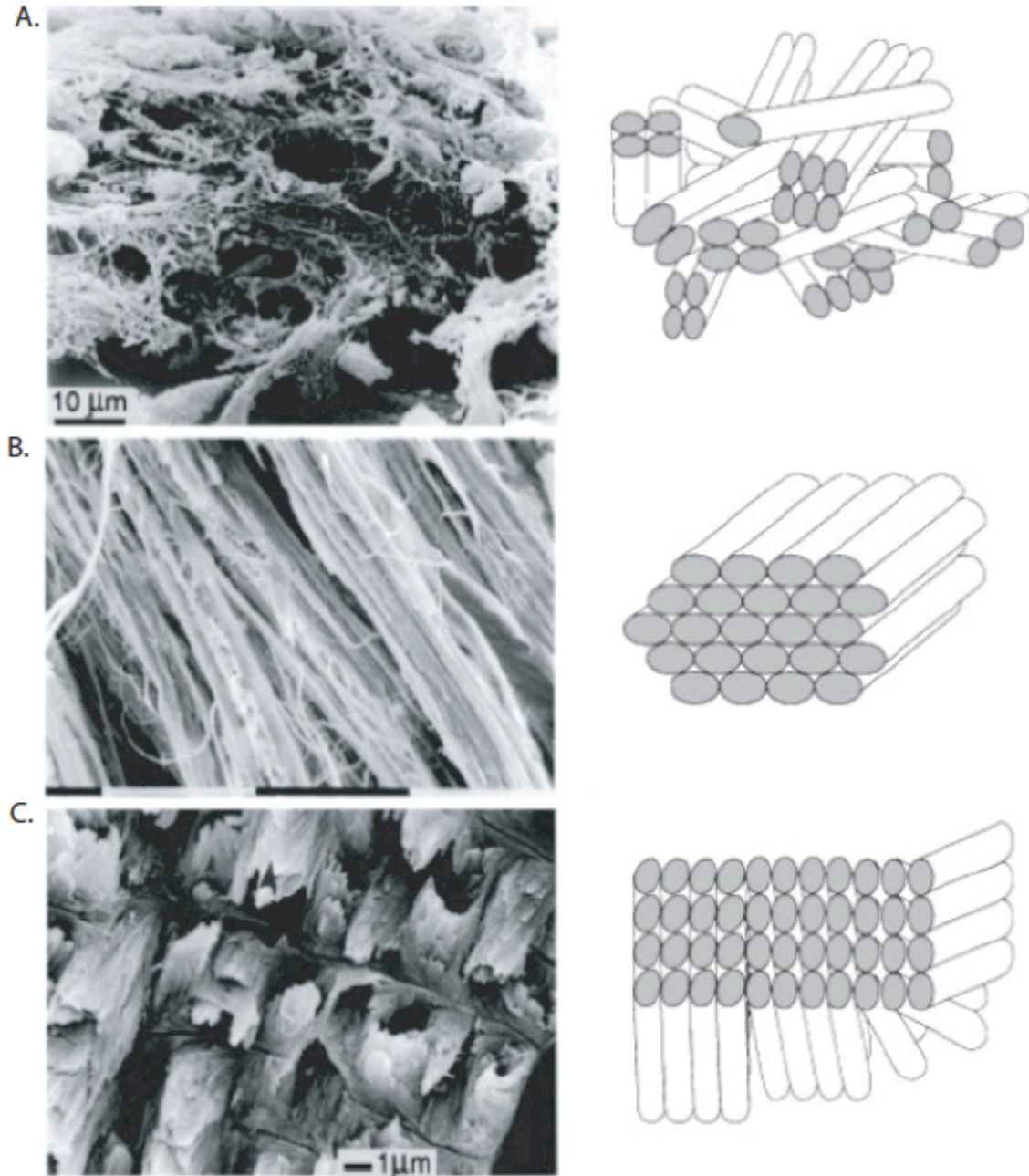
Figure 2.7 Organization schemes of mineralized collagen fibrils in bone. (**A.**) The collagen in woven bone is characterized by a "disordered" pattern and is highly mineralized (**B.**) Parallel-fibered collagen is found in bovine cortical bone and is advantageous due to its high degree of anisotropy in uniaxial loading (**C.**) Twisted plywood structures are most common in lamellar bone and allows for mechanical competence during multiaxial loading [From Weiner and Wagner Annu Rev Mat Sci 1998].

molecules and charged ions. Nor is it seldom in bone since it is the organization scheme found in typical bone types like bone callus. The mineralized collagen fibers are distributed randomly, in all various orientations, creating a tissue that is essentially isotropic. SAXS measurements have been made to confirm the lack of orientation the mineral particles, an indication of the lack of orientation of the fibers, in comparison to parallel-fibered bone [3]. Another characteristic of this bone type is the high amount of mineral content that is found in the tissue compared to other bone tissue types. It is very likely that the randomness of the mineralized collagen fibers is not coincidental and is a strategy used to relieve the spatial constraints in accommodating more inter- fiber and fibrillar mineral between mineralized collagen fibers. Not only is woven bone isotropic, it is mechanically stiffer and is not very compliant due to the extra amount of mineral. This type of bone is found predominately in amphibians and reptiles [12] and in these organisms, this bone type is thought of as a storage mechanism of mineral instead from a mechanical perspective since most of these organisms are sessile during the winter months.

2.4.2 Parallel fibered

In the simplest case, mineralized collagen fibers are stacked upon each other, all in the same orientation, to form a highly anisotropic bone type called parallel-fibered bone (**Figure 2.7(B.)**). The degree of mechanical anisotropy, a quantity that is indicative of the mechanical which varies with the length-scaled examined, is typically found to be approximately 0.3 for whole bone [44, 45]. The ability to vary the degree of anisotropy in tissue allows for optimization of materials properties. This strategy is especially useful in long bones where much of parallel-fibered bone type is found. By having such a tissue that is isotropic would make mobility energetically expensive as well as mechanically inefficient. The property of anisotropy in bone is predominately a result of the highly orientated parallel-fibered bone which compose the tissue. The orientation of these parallel-fibered "stacks" of mineralized collagen in bone is typically in the direction of the main loading axis. This enables bone to be mechanically optimized to a specific loading direction by having strength of the material primarily directed towards the load.

2.4.3 Plywood-like structures

In the bones of most terrestrial organisms, the mineralized collagen fibers are arranged in fiber arrays such that all are aligned to one orientation in a transverse plane. By progressing along the longitudinal axis, the orientation found in each neighboring transverse plane is found to be slightly off by a few degrees in relation to each other (**Figure 2.7(C.)**). Groups have reported that the degree of off-axis to be ~30° between two neighboring transverse planes [11, 12]. This organization is appropriately named the twisted-plywood organization due to the "twist" that is observed through the transverse planes along the longitudinal axis in the tissue. Lamellar bone is composed of these twisted plywood structures possibly due to the ability of the tissue to handle more diverse mechanical loading such as multi-axial loading, but still utilize the innate anisotropy provided by the mineralized collagen fiber. The assembly process of these twisted plywood structures are based on the innate physio-chemical properties of collagen [46]. At high enough concentrations of collagen, the molecules assemble into cholesteric structures typically found in liquid crystals. Giraud-Guille and coworkers have delineated the liquid crystalline arrangements of collagen in bone with electron microscopy [46] (**Figure 2.8**).

Many of these structural arrangements depend not only on the physio-chemical properties of the collagen fibers and fibrils, mineral, and NCP components, but also on the type of mechanical stimuli applied. By way of cellular networks that form a mechanosensory system, mechanical cues can stimulate cells to undergo certain processes such as growth and proliferation. In the case of bone, cells aid in forming the structural motifs required for mechanical homeostatis as well as reinforcing structural motifs utilized by existing tissue in the material bone [9]. These motifs are themselves the basis of bone tissue types that are widely different mechanically and structurally.
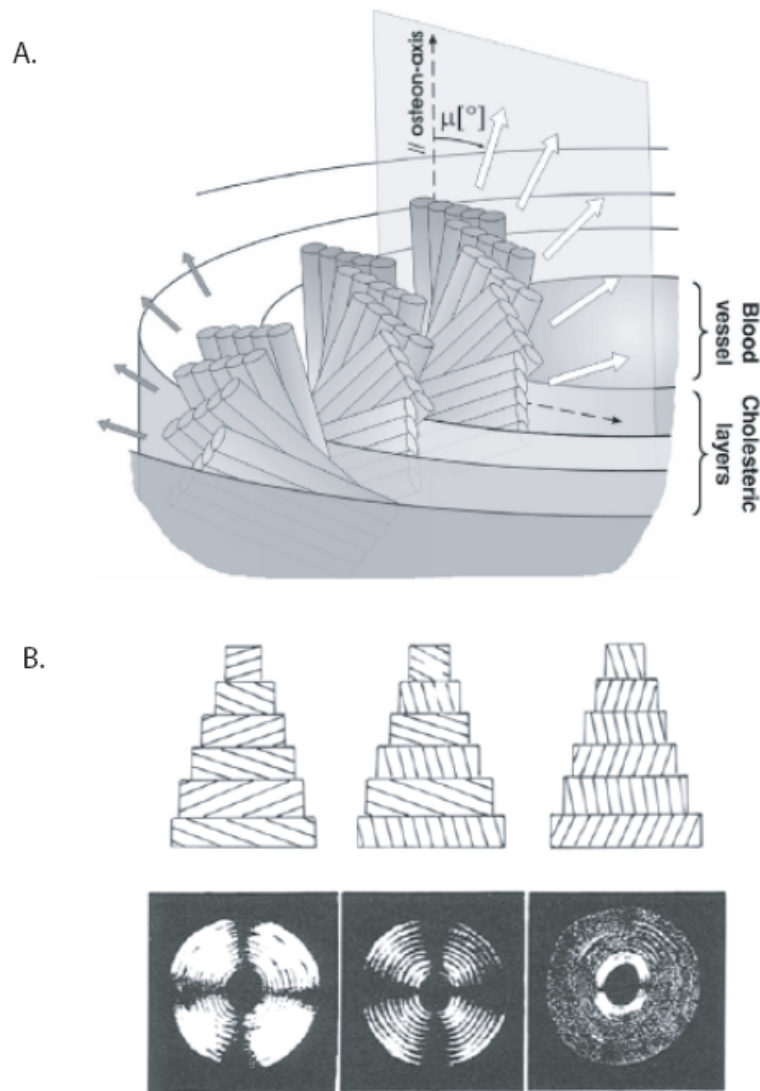
Figure 2.8 Fibrillar texture in the osteon. (**A.**) A schematic of the twisted plywood structure with respect to the main osteon axis (**B.**) Drawings of Ascenzi's model of the types of osteons observed under polarizing microscopy [(A.) from Wagermaier et al. Biointerphases 2008 (B.) Giraud-Guille Calc Tiss Int 1988].
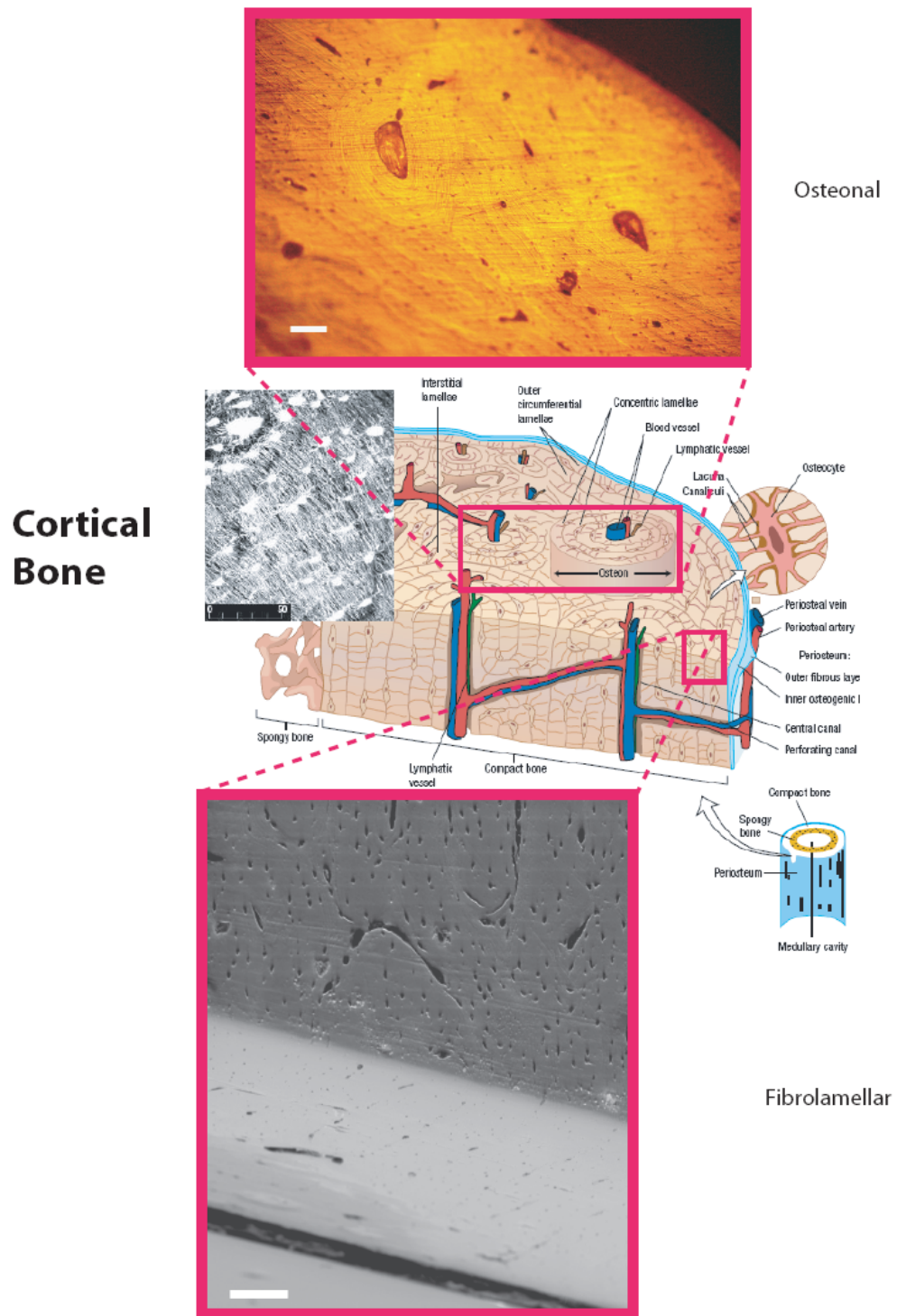
Figure 2.9 Organization of osteonal and fibrolamellar components in cortical bone. The microstructure of cortical bone reveals two types of load bearing elements, osteonal and fibrolamellar tissue. Fibrolamellar tissue is highly oriented and fast growth, allowing high loads relatively soon after birth. However, osteon tissue is made up of alternating twisted plywood structures and comes about from bone remodeling processes [Adapted from Taylor Nat Mat 2007].

2.5 Osteons

In the previous section, lamellar bone is mentioned often and referred to as a multi-axial, mechanically competent material. In a similar manner, remodeling processes in bone introduces a new structure, the osteon (**Figure 2.8(B.), 2.9**). This structure of concentric cylindrical substructure typically surrounds a sensitive channel and is oriented along the longitudinal axis of bone. Each layer is composed of a twisted plywood structure just like lamellar bone. Essentially, each onion-like layer of the osteon is a plane of lamellar bone folded into a cylinder (**Figure 2.8**) [47, 48].

2.5.1 Osteonal structure

The osteon creates a material that is competent in several axis, but most notably in the direction of the main loading axis (**Figure 2.8, 2.9**). The problem of having stacked planes of radially arranged mineralized fibers is due to the inability to adjust to the growing and developing bone tissues. In the case of an increase or decrease of an artery, many radial arrangements along different planes in the longitudinal axis would have to be displaced and reconstructed. For an osteon to accommodate such changes, an osteonal layer is either added or removed. As observed in **Figure 2.9**, "new" osteons are observed by their relatively small diameters, whereas "older" osteons have larger diameters. The occasional appearance of two osteons merging occurs due to spatial constraints, where one osteon increases in a diameter at the expense of another (**Figure 2.9**). In experiments where "new" mineral is labeled, the accretion of the osteonal layers are studied with time [49] [50].

2.5.2 Parallel fibered vs. osteonal structures

When comparing osteonal bone to parallel fibered lamellar bone, beyond the structural differences between the two bone types, questions regarding whether one or the other is more mechanically competent in handling typical stresses and strains arise. Liu and

Weiner [11] have used three point bending, a technique that simulates the tensile and compressive forces on the material, to measure the elastic modulus and work to fracture of both lamellar and osteonal bone along the main loading axis as well as orthogonal to the loading axis [12]. Results from these experiments have concluded that parallel fibered lamellar bone is mechanically stronger and tougher than osteonal bone. Similar experiments on osteonal bone using nanoindentation methods have shown that the elastic modulus derived from the hardness validates the observation of a more mechanically competent lamellar bone type compared to an osteonal bone type (**Table 2.1**). Simple reasons can explain the mechanical properties of lamellar bone such as a higher degree of mineralization as well as the methods used in the aforementioned cases, only measure small constituents of the bone types. In the case of osteonal bone, this is especially true since the entire osteon structure is one that must be examined and not only a component of it. The sectioning of the osteonal bone in the aforementioned experiments only sample a small range of the twisted plywood structure that is available. Thus, using microindentation techniques as well as mechanical measurements of homogenous, whole tissue sections, osteonal bone would more mechanical competent.

2.6 Plexiform bone

In contrast to lamellar and osteonal bone, plexiform bone tissue precedes these secondary growth tissues. The tissue is rapidly grown and typically developed in large animals like cow and sheep to support their large masses. Unlike woven bone, the tissue is organized in an oriented manner with its collagen fibrils and mineral platelets highly aligned along the main loading axis, as observed in its "brick-like" microstructure. When investigating the tissue at higher magnifications at the level of a single "brick," plexiform or fibrolamellar bone [3] is found to consist of a "sandwich" layering of lamellar bone with woven bone layered in between. This scheme in having the lamellar component at the edges of a single brick while retaining an inner woven region enables the small "bricks" to maintain a required stiffness to undergo the necessary mechanical loading without buckling. The "bricks," single fibrolamellar units, are themselves delineated from each other by haversion channels that are found throughout the tissue and possibly, serves

as a source of nutrients to osteocytes within a unit. An amazing aspect is the ability of controlling haversian channels to be spaced at regular intervals from each other, resulting in fibrolamellar units to be consistently ~150 μm in width and ~3 mm in length throughout the tissue. This fibrolamellar bone tissue is typically found in the cortex of young bovine cortical bone, most likely as a mechanisms to prevent buckling that may occur with other types of tissues under the same loading conditions. Unlike in other animals where large mechanical loads are not problematic, such as in mice bone, the cortex of mice cortical bone is not occupied by the "brick-like" structures of fibrolamellar bone, but is mainly woven bone. The stiffness and strength of fibrolamellar bone is not necessary to accommodate the loads mice bones experience, encouraging a more "economic" route of continued usage of woven bone throughout its lifespan. The mechanical behavior afforded by the high degree of orientation of its mineral and organic components makes fibrolamellar bone a material that will be a topic of further discussion in subsequent chapters.

2.7   Skeletal Disease in Mice Models

Typical skeletal disease models in mice are produced by the deletion of a key regulator of signaling pathways which control cellular activity. In these disease models, to determine if any of these gene deletions have any effect, skeletal tissues are investigated for specific phenotype that may be connected to this deficiency. Usual phenotypes observed come in the form of a significant difference in mineralization, whether it is a decrease or an increase in mineral from the wildtype case. Of particular interest are the TGF-β [51] and Ras [52] signaling pathways on skeletal development. These experiments attempt to simulate the disease in mice to emulate the disrupted biochemical pathways that may help in understanding the diseased state [53] [35].

In an effort to understand the various organic components which are important in regulating the materials properties of the material bone, knockout mice models are utilized. Specifically, mice models are used to investigate the deletion of proteins believed to maintain a role in mineralization as well as recruitment of osteoblasts and osteoclasts to observe the effects on the materials properties of bone. In the following

sections, the materials properties of samples from the Schnurri-3 (Shn3), Neurofibromatosis-1 (NF1), and α-Heremans-Schmid glycoprotein (Ahsg), also known as fetuin-A, mice models will be examined and the mechanisms by which these deficiencies affect the material bone further delineated.

2.7.1 Schnurri-3 (Shn3)

In the case of the Schnurri-3 (Shn3) mice model, a specific signaling factor necessary for regulation in the TGF-β signaling pathway, specifically the signaling molecule Runx2, is inhibited and shown to affect osteoblastic activity [52]. An increase in osteoblastic cell activity is believed to correlate to an increase in the amount of mineral produced in bone tissue. In addition, no effect on osteoclastic activity is observed. Histological examinations, X-ray radiography, as well as μCT imaging of skeletal tissues have qualitatively confirmed an increase of mineral in Schnurri-3 knockout mice in comparison to the normal wild type case. This increase in mineral is age-related, whereby no differences in mineral are observed between the knockout (KO) and wildtype (WT) after birth, while at 7 months, the Shn3 (-/-) animals have marrow cavities in their long bones entirely enveloped by mineral [52].

From pulse chase and affinity binding experiments, Shn3 binds competitively to Runx2, preventing the binding of Runx2 to cellular targets that are implicated in the production of bone sialoprotein and osteocalcin [52]. These non-collagenous proteins have been implicated in processes of nucleating extracellular matrix mineralization. Thus, Runx2 in Shn3 (-/-) animals is not regulated and the production of non-collagenous proteins is unchecked, leading to uncontrolled mineralization. Interestingly, this increased mineralization is significant only at older ages. Comparing the fetus and newborn, differences in mineralization of Shn3 (-/-) and Shn3 (+/+) mice are not noticeable. Differences in bone mineralization and structure only become apparent beginning at 1-2 weeks after birth. This age dependence indicates that there exist two stages in mice skeletal development, such that prenatal skeletal development is regulated by separate pathways and postnatal development of skeletal tissues is sensitive to Schnurri-3

regulation. The example of Shn3 deletion effects in the skeletal system highlights the importance of regulation in the TGF-β pathway in normal postnatal development of mice bone.

2.7.2 *Neurofibromatosis-1 (NF1)*

In a similar manner, NF1 mice models are used to examine the p21-Ras signal transduction pathway and specifically, the extent of the dysfunction from the molecular to the tissue levels [54] [55] [56]. NF1 (-/-) mutations disrupt the Ras signaling pathway by interrupting neurofibromin-1 from serving as a negative regulator of ras, in effect causing ras to erroneously activate pathways that take part in cellular growth and proliferation. Specifically, cells such as chondrocytes and osteoblasts are affected by the NF1 (-/-) mutation, leading to defects at the tissue-level such as premature skeletal joint development, dysplasia, as well as reduced mobility [54] [55]. At the tissue level, NF1 (-/-) animals are observed to have severely disfigured long bones with a tremendous decrease in materials properties.

2.7.3 *α-Heremans-Schmid Glycoprotein (Ahsg)/Fetuin-A*

In another mice model, knockout mice model of α2-HS-glycoprotein, also known as fetuin, is examined for effects on skeletal development and growth. In these mice models, the lack of fetuin in the animals causes non-specific ectopic mineralization. In particular, vascularized soft tissues are vulnerable to the aggregation of mineralized "clumps". The source of the mineralization is the instability of the Ca^{2+} in blood resulting in unwanted precipitation in vascularized tissues. Fetuin has been itself found to be an abundant serum protein that acts as a chaperone of the Ca^{2+} mineral, having high affinity to mineral [57, 58] [59] [60]. Taking such an important protein away from an organism has been shown to incite renal, cardio-pulmonary, as well as hepatic dysfunction [61] [62]. However, the effect of removing fetuin in skeletal tissues, a system that is already mineralized, has not been thoroughly investigated, but will be the focus in this work.

As in the aforementioned cases of Shn3 (-/-), NF1 (-/-), and Ahsg (-/-), the comparative differences in materials properties of WT and KO tissues aid in delineating the mineralization processes as well as the regulatory measures utilized by the organism. The materials properties of these mice models will be investigated and discussed further in **Chapter 4**. Due to the similarities in the mouse and human genomes, by studying skeletal disorders in mice models, it is hoped the same disorders in humans can also be understood. Specifically, these underlying mechanisms which cause dysfunction in mice models may help in understanding the diseased state in humans.

2.8 Mechanical behavior of bone

The mechanical behavior of bone is implicitly a result of the composite nature and composition. In the material bone, the brittle nature of the mineral does not overshadow the elastic character of the organic components nor vice-versa. Simply, bone utilizes the properties of both its major components (**Figure 2.1**) (**Table 2.1**). The process in which the two major constituent components, the mineral and organic components, are assembled is not trivial. In a simple arrangement, when the two materials are organized in a serial fashion (Reuss model), one realizes the materials properties are not similar in tensile mode. When the two materials are organized in a parallel manner (Voigt model), the materials behavior in the lateral direction also is lacking in tensile mode. However, in an organization scheme based on a hybrid Voigt-Reuss model, the materials properties are close to bone [63]. In a typical tensile measurement, the result is a stress-strain relationship which is summarized by a linear elastic regime that typically extends from ~0-1% strain followed immediately by a yield point and then a plastic, irreversible deformation regime which extends until ~1-1.5% strain before the ultimate tensile strength is reached and eventually, the material fails.

Table 2-1 Mechanical Properties of Osteons and Interstitial Components in Cortical Bone Elastic moduli and corresponding hardness values (only in nanoindentation) obtained from different modes of mechanical testing between osteonal and interstitial samples [Cowin Bone Mechanics Handbook 2001].

| Bone Tissue Type	Elastic Modulus (GPa)	Hardness (GPa)
Osteon (L)		
Tension	11.7 ± 5.8	--
Compression	6.3 ± 1.8	--
Shear	3.3 ± 0.5	--
Osteon (A)		
Tension	5.5 ± 2.6	--
Compression	7.4 ± 1.6	--
Shear	4.1 ± 0.4	--
Osteon (T)		
Compression	9.3 ± 1.6	--
Shear	4.1 ± 0.3	--
Osteon	--	0.285
Interstitial	--	0.349
Osteon	22.5	0.614
Interstitial	25.8	0.736
Osteon	18.6	0.52
Interstitial	20.3	0.59

2.8.1 Deformation behaviors

As mentioned in **Chapter 1.2**, initial stage of deformation in bone during tensile loading is characterized by a linear elastic region. The linear elastic regime represents reversible extensibility in the material—that is, no permanent damage occurs in the material within this range of <1 % strain and there is complete recovery after mechanical deformation. Another prominent property of bone is its viscoelastic properties, the time dependent behaviors that include creep and stress relaxation. The origin of this elastic behavior comes about from the main organic component of bone, the oriented collagen fiber phase.

With increasing strain, the yield point is reached signifying a transition from the linear elastic regime to post-yield behavior. Beyond this point, deformation is not reversible, but rather inelastic. At the molecular level in the material, the yield point signifies van der Waals as well as hydrogen bonds being broken in the material. As

proposed by Jaeger and Fratzl [64], a staggered arrangement of the mineral platelets and collagen fibrils within mineralized collagen fibers allow for a tension-shear chain model of loading mechanism between the mineral platelets and the surrounding soft organic matrix [65] [66]. Load transfer from one mineral particle to another occurs via a shearing mechanism such that mineral platelets carry much of the mechanical load. A defect of the load transfer mechanism by way of excess load lends itself to the formation and accumulation of defects in the micro-structure, seen at the macro-scale as voids and cracks. A defect of the load transfer mechanism by way of excess load lends itself to the formation and accumulation of defects in the micro-structure, seen at the macro-scale as voids and cracks. The presence of crack formation and cracks themselves do not mean end-of-life for materials. On the contrary, cracks which are properly distributed and oriented within a material, is used to absorb and deflect larger cracks that are catastrophic to the material [67]. In the same scheme, crack bridging can absorb the energy of propagating cracks in the material and slow the process of crack propagation. In fact, in materials like ceramics, microcracks are often part of mechanisms used to prevent crack propagation in the material. To quantify whether crack formation and propagation or crack inhibition occurs, a relationship of the amount of elastic strain energy and crack formation energies is summarized as follows by

$$\Delta U = -\frac{\bar{\sigma}^2 \pi a^2 B}{E} + 2aBG_c \qquad \textbf{(Eq. 2.2)}$$

where U is the internal energy in the material, $2aBG_c$ is the work to crack formation, and $\frac{\bar{\sigma}^2 \pi a^2 B}{E}$ is the total strain energy in the material [63, 68]. When material failure occurs, the total energy of the system decreases and crack propagation occurs catastrophically. These similar strategies in preventing crack propagation are also observed in cortical bone [69-71]. Osteocytes and the respective osteocytic lacunae are essentially void structures in the bone material, defects in the material which aid in crack deflection and bridging [72, 73]. In addition, the composite fiber nature of cortical bone inhibits cracks from propagating transversely due to the energy dissipative strategies such as shearing processes between organic components at the micro-scales as observed in experiments detailing the transition from brittle to ductile fracture by Peterlik and co-workers [67].
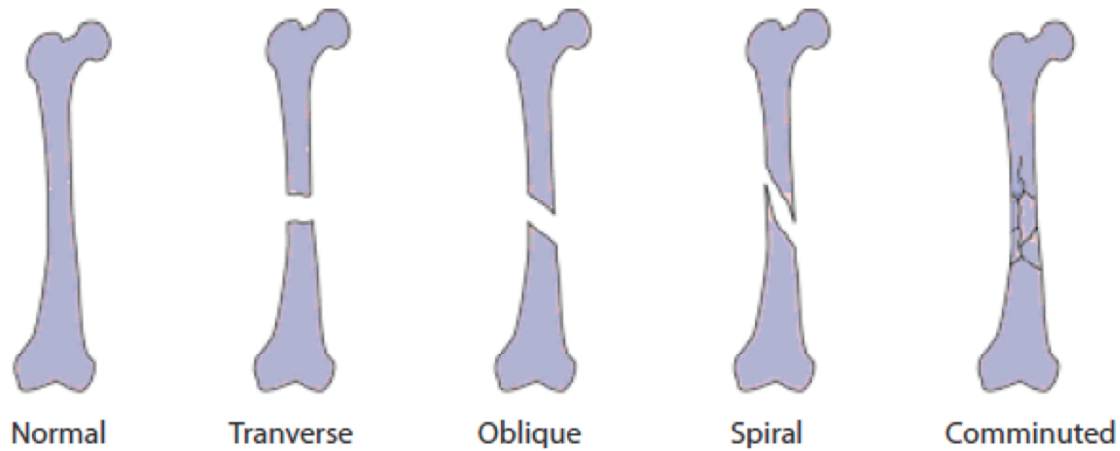
Figure 2.10 Common fracture types in bone tissue Due to the various ways in which bone tissue is loaded, the failure modes in bone can occur via different mechanisms as witnessed by the numerous types of fracture [Adapted from Cowin and Doty Tissue Mechanics 2006].

2.8.2 Failure in bone

Failure in the material bone occurs via different mechanisms. As observed, these mechanisms lead to differences in fracture damage at the tissue level (**Figure 2.10**). In understanding these failure mechanisms, the micro- and nano- scales must be examined since damage leading to material failure in bone has origins at these shorter length-scales [74]. Whether it is failure via fracture from the mineral or organic matrix components, or failure at the mineral-organic matrix interface, the micro- and nano- structures dictate the mechanisms of deformation, from damage initiation to fracture (**Figure 2.11**). Typically, damage at these short length-scales as witnessed with micro-cracking, can accumulate appreciably into damage noticeable at longer length-scales [69] [51] [75] [76]. Defects in the material at the nano-scale, such as mineral platelet defects, can also initiate cracks and develop into crack propagation at the tissue level. Damage itself at the micro- and nano-scales is an indicator of localized structural failure that increases the stress concentrations on neighboring constituent elements at these length-scales. Many of these stress concentrations are found to be at boundaries where mineral and organic components of the material interface. Osteocyte lacunae, haversion channels, canaliculae, as well as cellular processes are examples of sites where stress concentration is presumably higher
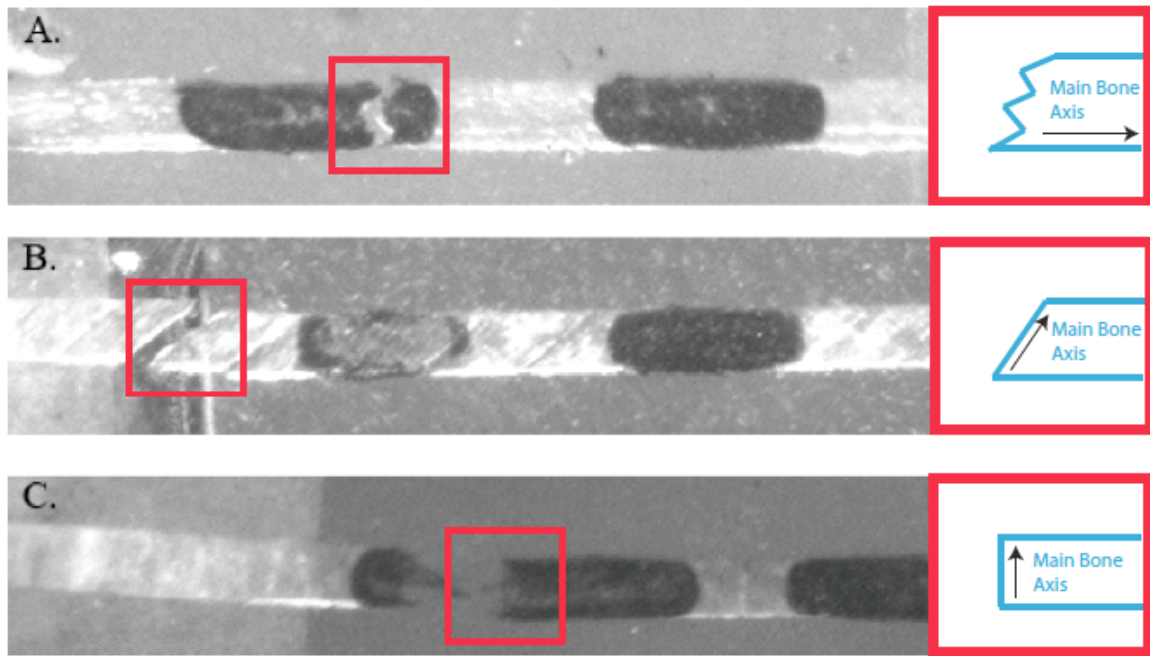
Figure 2.11 Typical fracture surfaces in fibrolamellar bone measured under tension
(A.) Brittle fracture surface of a fibrolamellar bone sample prepared along the main axis
of bone (B.) Fracture surface from shearing occurring in a fibrolamellar bone sample at
45 from the main bone axis (C.) Fracture surface from transverse loading of a
fibrolamellar sample at 90 orientaiton from the main bone axis.

and are prone to damage compared to regions lacking these features in the material bone
[77] [78] [73, 79]. In summary, failure of the material bone has its origins at lower
length-scales, specifically at the level of the micro- and nano- structures.

At the nano-scale, Nature addresses the damage prone characteristics of these
structures at this level by increasing material heterogeneity to promote energy dissipation
in bone [49]. Specifically, these heterogeneities can come in a variety of forms.
Phosphoproteins such as osteopontin integrated into the inter-fibrillar mineralized
collagen space adds heterogeneity to the material and as shown by Fantner and
coworkers, these proteins can also take part in sacrificial bonding at the nano-scale [34].
The ability to dissipate crack- forming and propagating energies aids in toughening the
material to prevent damage from evolving into material failure. Other strategies
employed by the material bone at these shorter length-scales include using weak
interfaces, voids as well as cellular structures in bone, components built into the
biological design principles to stop crack propagation and averting catastrophic material

36

failure [70] [80]. By directing where damage can accumulate, Nature utilizes architecture in allowing cracks to form in regions that are more tolerant to damage, whereas damage intolerant regions are shielded away from the slightest damage. As will be shown in later chapters, these architectural design principles are vital in contributing to the material bone's mechanical behavior.

In this chapter, an overview has been provided to understand the various aspects that have an effect on this relationship. Firstly, the composition of bone into an organic and mineral phase has helped elucidate the biphasic behavior in the mechanical behavior of bone. In an effort to make one seamless material from two major constituents, the organization of the constituents in bone are so intertwined that growth and development of the entire tissue is defective when one or the other is altered. This forms the basis of the composite-like structuring that is widely seen in bone from the tissue- to the nano-length-scales [81] [82]. Recently, the relationships between these sub-structures have provided insights into how hierarchy participates in the mechanical behavior of whole tissues. The ability to combine these various stiffening and strengthening strategies in a biological environment, composed of elements which tend to be soft and amorphous, into one integrated tissue further complicates the inquiry into bone. Presently, many groups find just how elaborate bone is in their efforts to mimic the tissue in artificial systems [83] [84, 85] [86, 87]. How does a living tissue maintain its structural integrity and mechanical competence as well as accommodate the biological processes that dictate development, growth, and regeneration? The answer is in bone [88].

3 Experiments and Methods

Hierarchical structuring in bone requires a multitude of techniques to elaborate relationships of its materials properties at every length-scale - from the ordered hydroxyapatite nano-platelets to the micron-sized trabeculae found forming a network of internal scaffolding in the femoral head [1, 3, 12, 76]. In this chapter, mechanical methods are used to understand these relationships between bone's function and structure. Specifically, the focus of this work is on bones from bovine and murine model systems and results from these experiments are a basis for understanding the complexity in bone of humans and other organisms.

Bone's complexity can simply be summarized with observations of its shape and function by eye. The diversity of mineralized skeletons in organisms - the ways shape and function can vary tremendously in Nature - hint's at precision in controlling bones to service the many different functional requirements of the material (**Figure 3.1**). To that extent, to understand the degree of diversity within these differences are and where might these differences in the material originate - or conversely, just how similar different mineralized tissues are, methods focused at probing the material at length-scales of the micro- and nano- are utilized.

3.1 Sample preparation

Heterogeneity in biological materials can complicate the characterization process in evaluating materials properties. Unlike metals and ceramics, homogeneity of the material is often found typically at the micro-scale and up, enable simple sample handling and subsequent characterization of materials properties. Specifically, a cylinder of a ceramic material in the dimension of a typical long bone (i.e. femur) is tested in compression mode until failure and its microstructure modeled with ease, describing the processes from initial compression, bending, and ultimately, failure. Taking a similar
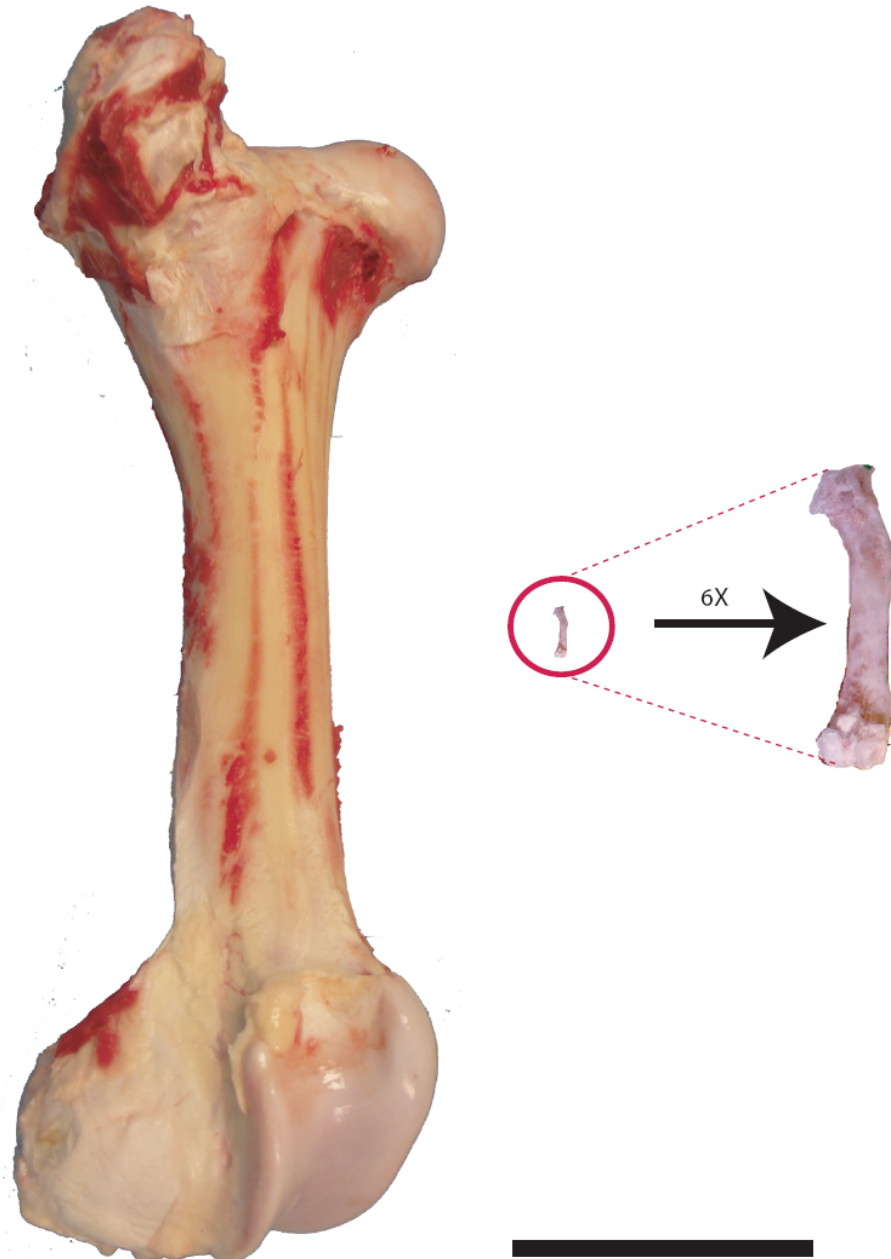
Figure 3.1 Scaled comparison of femurs from bovine and murine bones. A significant difference between bovine and murine bone is the size difference which affects tremendously the role of the microstructures in the respective materials properties of these bones (scale bar: 10 cm).

cylinder constructed from bone and submitting it to the same measurements as the ceramic cylinder, depending on which structure and length-scale is examined, the

materials properties of the bone cylinder would differ over a large range due to the various structures in bone just at one length-scale. Thus, bone cannot be treated as just an ordinary material and placed directly in a tensile or compression tester in hopes of obtaining a result that is characteristic of the material.

Sample preparation of bone material is necessary to properly evaluate its materials properties - to understand what is exactly being measured. In the case of bovine and murine bone, the strategy to build a tissue to resist fracture from hierarchical structures innately adds heterogeneity to the material [1, 12, 51, 70, 89]. In **Figures 3.2** and **3.4**, microstructural heterogeneity is removed by identifying and isolating
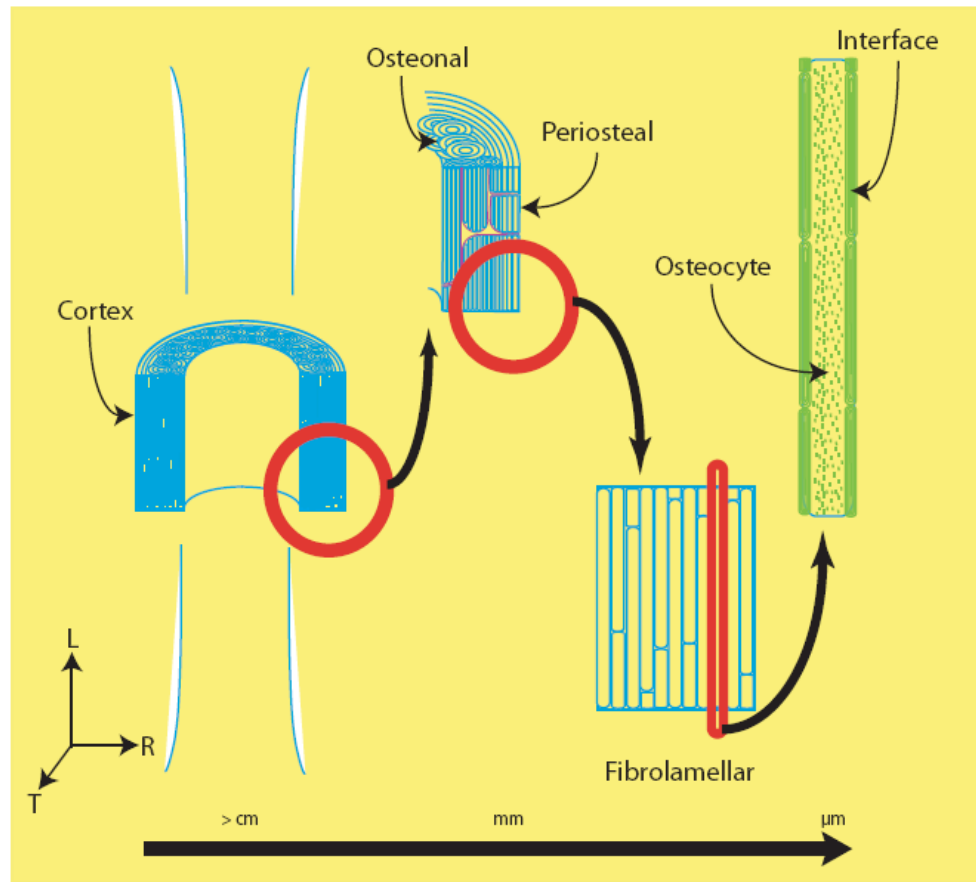
Figure 3.2 Schematic diagram of bovine cortical bone. The innate structural hierarchy in bovine cortical bone is observed spanning several length-scales—from the tissue to the μm. Each diverse substructure accommodates a certain set of requirements at the respective length-scale (i.e. blood vessels, cells, etc…) and contributes to the overall materials behavior of the tissue. Of interest is the contribution of each substructure to the materials properties of the whole tissue.
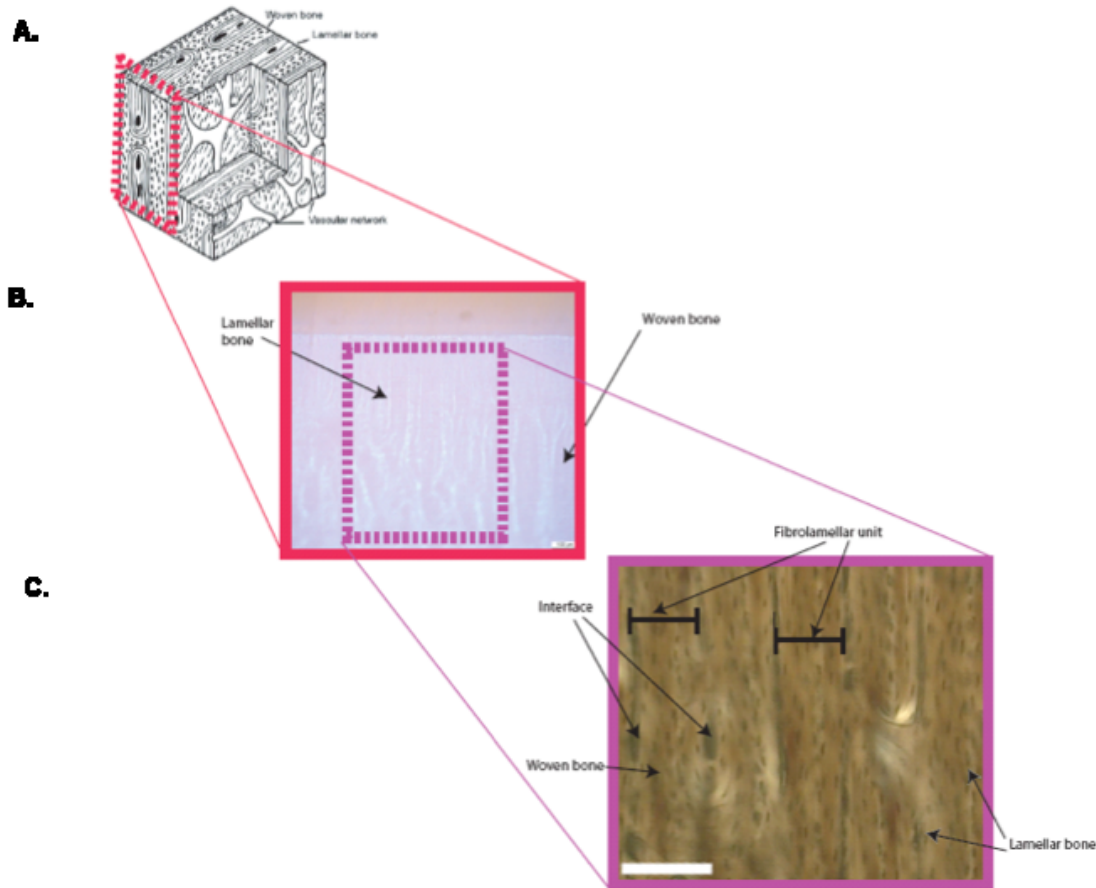
Figure 3.3 Decomposition of fibrolamellar bone--where and what Fibrolamellar bone is found in periosteal cortical bone and is characterized by a "brick-layer" organization (**A.**) Fibrollamelar bone is typically found in the radial-longitudinal plane of cortical bone with its characteristic "bricks" laid parallel to the bone's long-axis (**B.**) At higher magnification, within each fibrolamellar unit structurally distinct regions are observed (**C.**) Under polarized light microscopy, these constituent regions are found in a lamellar-woven-lamellar arrangement (scale bar: 150 μm) [(A.) adapted from Currey Bones 2002].

homogenous material at one specific length-scale in the material. Through the use of standard materials sectioning saws (Leica SP1600, Leica Mikrosystem Vertrieb GmbH, Bensheim, Germany) specifically adapted to sectioning biological samples, sectioning artifacts are reduced. In both these cases, homogenous microstructures within the material are identified at the micro-scale. Fibrolamellar units in bovine periosteal cortical bone is found and is organized regularly in preferred orientations to form tissue capable
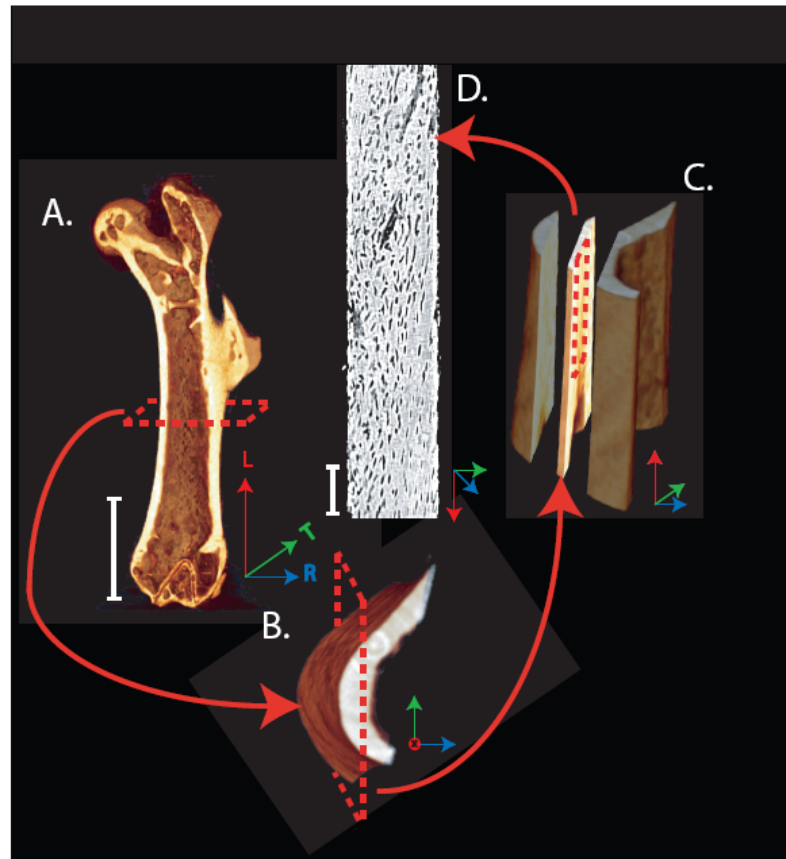
Figure 3.4 Schematic diagram of femoral murine bone. (**A.**) A whole femur is shown with the longitudinal plane exposed (as seen by micro-CT) (scale bar: 3mm) (**B.-C.**) Cortical bone from the mid-diaphysis is of mechanical interest due to the defined forces this region of the femur is loaded (**D.**) Of specific interest is the role of the microstructure in the overall materials behavior of the tissue (as seen by phase enhanced X-ray radiography) (scale bar: 75 μm).

of being loaded in a predominant direction (**Figure 3.3**). This situation differs to the material in murine bone where the length of the equivalent bone is approximately 400% smaller than bovine, murine bone does not require the strengthening mechanisms present in bovine bone and retains bone without fibrolamellar units (**Figure 3.5**). Although much smaller in dimension, murine bone is prepared in a very similar way to bovine bone for characterization of its materials properties by mechanical measurements (**Figure 3.6**).

3.1.1 UV laser micro-dissection

In both bovine and murine bone sample preparations, gross material heterogeneity is removed by typical materials sample preparations such as slow speed sectioning (IsoMet
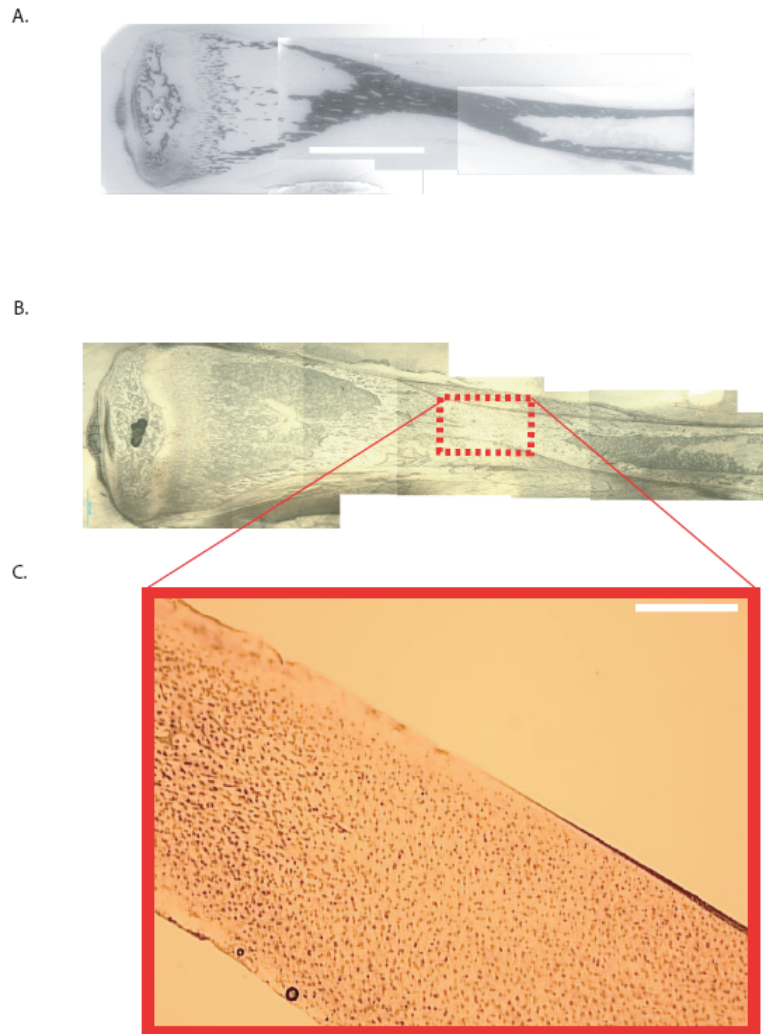
Figure 3.5 Femoral murine bone as seen in electron and light microscopy (**A.**) An inverse scanning electron micrograph obtained from a backscatter detector demonstrating the amount of electron dense mineral (black) throughout the tissue, especially at the mid-diaphysis region scale bar: 2 mm (**B.**) Light microscopy of the same sample as in (A.) displaying the microstructure scale bar: 500 μm (**C.**) High magnification light microscopy image of the osteocyte lacunae at the microstructure (scale bar: 300 μm).

Low Speed Saw, Beuhler Ltd., Lake Bluff, IL, USA) and soft polishing (AP-D, Struers A/S, Ballerup, Denmark) and grinding (Logitech PM5, Logitech Ltd., Glasglow, UK). Schemes in preparing bovine and the smaller murine bone to obtain homogenous material for materials characterization are observed in **Figures 3.2** and **3.4**. It is important to note that during the entire preparation process, the samples are kept hydrated throughout as dehydration affects dramatically the materials properties [18, 90-92]. Additionally, specific regions of the sample are sectioned with a ~1 μm precision in any desired size, orientation, and morphology with the use of a ultra-violet (UV) laser micro-dissection system (PALM MicroBeam C, P.A.L.M. Microlaser Technologies GmbH, Bernried, Germany) with a computer-controllable sample stage (**Figure 3.7**).

In the same way, laser technologies used in modern day surgery to make incisions as well as remove biological tissue [93, 94] [95], UV laser micro-dissection enables precise ablation of chemical bonds in specific areas of the tissue without damage to neighboring regions. The ability to precisely ablate small regions allows for limiting sample artifacts during preparation. With the use of accompanying optical objectives (5-100X) from an inverted microscope to converge the beam to a more precise spot, the UV laser achieves small, defined cutting regions in the range of 1 μm. The solid state neodymium-doped yttrium aluminum garnet (Nd:YAG) is the UV laser source which provides a coherent beam with a wavelength of 337 nm and an energy of 95 μJ when focused onto a spot size of ~1 μm in a specific focal plane. Furthermore, the laser operates at a pico-second pulse rate, specifically at a rate that is conditioned for the energy level and wavelength, ensuring the ablated sample does not suffer from effects of burning, the result of an intense beam focused on a spot too long. If the pulse rate is too slow, burning occurs, whereas if the rate is too fast, ablation does not occur. The pulse rate is especially noteworthy since many samples that are sectioned with this micro-dissection system are several tens of microns thick, requiring a focal plane-by-focal plane rastering to section through the sample. Thus, the ability to move to the sample before the laser beam irradiates the sample for too long is essential. This brings us to the next vital component of the micro-dissection system, the controllable stage. The stage is controlled
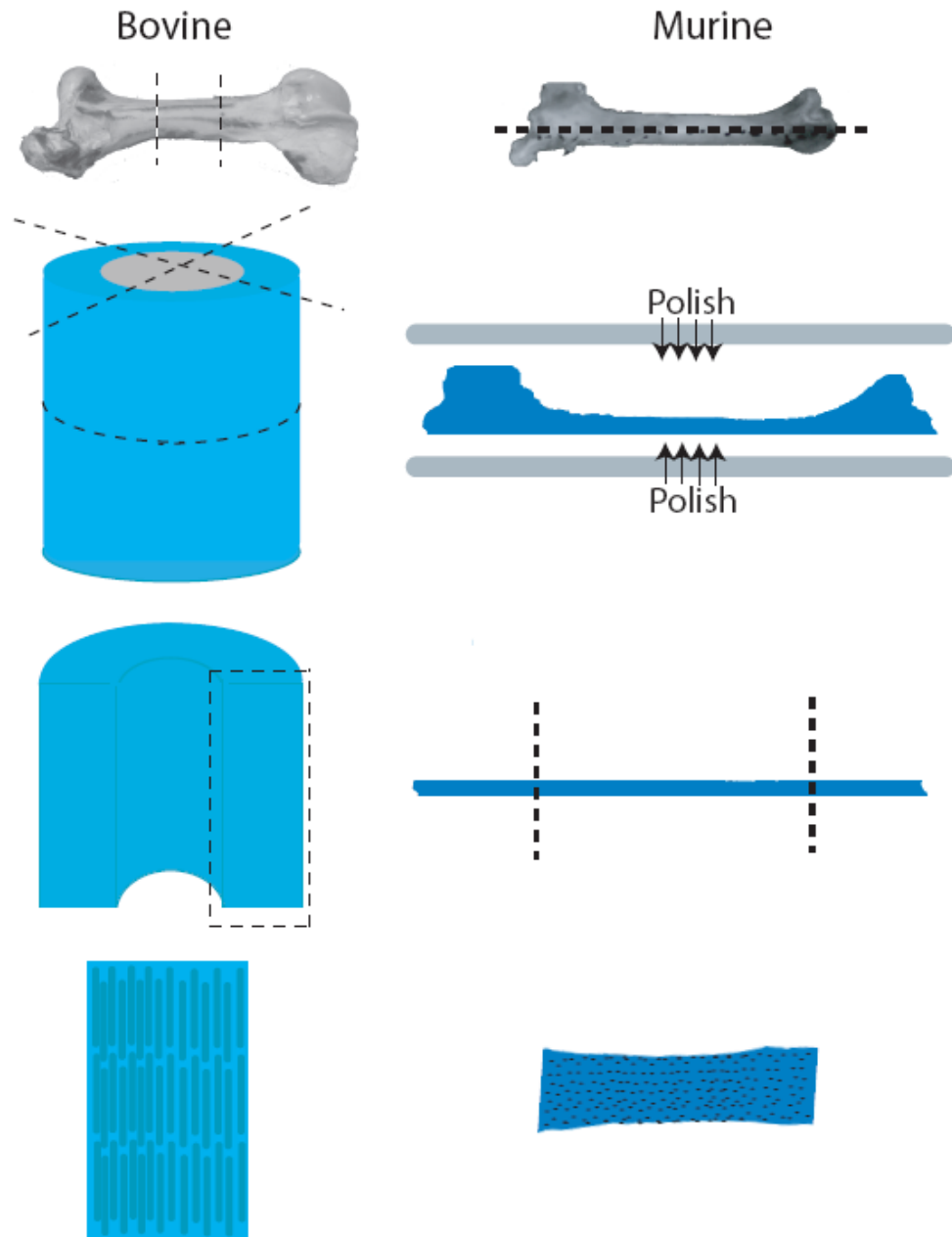
Figure 3.6 Gross sectioning of bovine and murine cortical bone To obtain a homogenous material for characterization of materials properties, a systematic procedure to remove inhomogeneities and in the correct orientation is shown in the above schematic diagram. An important note is that the entire procedure involves retaining the sample wet during sectioning to minimize sectioning artifacts.
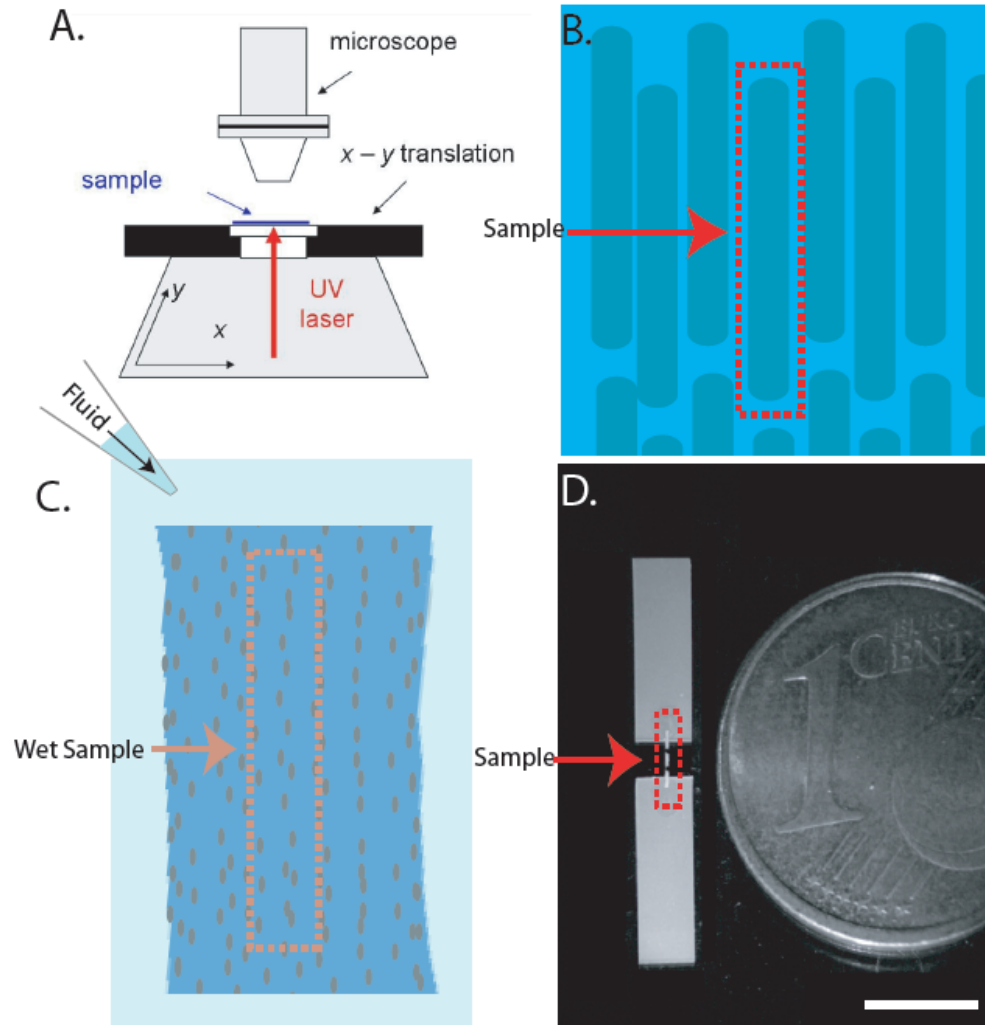
Figure 3.7 UV laser micro-dissection of mineralized tissues. (**A.**) With a computer assisted X-Y translation stage, samples with specific orientation and morphology are sectioned with ~1 μm precision (**B.**) Single fibrolamellar bone units are homogenously sectioned from bovine cortical bone (**C.**) Homogenous samples of murine cortical bone are sectioned in a wet environment, retaining its physiological environment throughout the sample preparation procedure (**D.**) Samples are glued with cyanoacrylate to stiff teflon sheets that are clamped into a mechanical tensile system (scale bar: 6 mm).

by a computer that has specific settings for each optical objective. At higher objectives, the stage moves the sample slower than at lower objectives to expose the sample to

enough flux for ablation. When rastering is necessary with the laser on a sample section, the sample stage can return to the same ablated areas with sub-micron precision to allow continued ablating of the same sections. It is important that for different types of materials, the speed of the stage, energy level, and material roughness are parameters to be adjusted for appropriate sample ablation.

Artifacts can occur when preparations of the sample do not occur in their native environments. To that extent, UV laser dissection of mineralized tissues takes place in a physiologically wet condition. The advantage of the system is its ability to automate the sectioning process in order to consistently provide samples in the same dimensions from the same homogenous regions. With the aid of the computer, the sample sections scale accordingly to the objective, thus, always having the correct dimensions even when ablating at 40 or 100X objectives. This enables for a consistent source of samples that are used for characterization techniques, such as mechanical and structural measurements.

3.2 Characterization of Mechanical Behavior

3.2.1 Micro-tensile measurements

Micro-tensile measurements provide quantitative results on the material including stiffness and UTS [96, 97]. Bone is a material that naturally is mechanically loaded in its native environs. Although our own bones are not entirely loaded in tension, much of the time in compression [98, 99], tensile forces are significant at the microstructure when our bones are subjected to torsion and bending. In coupling sample preparation with the UV laser micro-dissector to section homogenous regions of bone devoid of artifacts at the micro-scale (i.e. blood vessels and other microstructure defects), micro-tensile measurements can effectively probe the materials properties at the microstructure.

Figure 3.8 Schematic diagram of the Micro-mechanical Tensile Apparatus (MiTA) with sample. Uni-axial mechanical measurements (tensile) are performed on micrometer-sized homogenous mineralized tissues to assess the mechanical properties at the micro-scale of the respective tissue. The ability to keep the sample wet enables measurement close to/near physiological conditions. In addition, the compactness of the device allows insertion into measurement chambers for in situ measurements like in situ X-ray synchrotron measurements.

The micro-tensile tester is itself composed of a screw-driven motor (M-126.DG, Physik Instrumente, Karlsruhe, Germany), load-cell (ALD-MINI-UTC-250, A.L. Design Inc., Buffalo, NY, USA), sample holders for micro-scaled samples, and a controller (C-663 Mercury, Physik Instrumente, Karlsruhe, Germany) –together able to perform at tensile loads < 2.5 N and slow strain rates ~0.2 μm/s (**Figure 3.8**). The sample itself is a section with dimensions 150 μm width x 50 μm thickness x 3 mm length, with its ends adhered with cyanoacrylate to stiff Teflon foils which are attached to sample holders of a mechanical testing system. Initial sample holders keeping the sample attached to the micro-tensile tester via screw clamps, but have been replaced by a peg-and-hook method due to the torque applied to the samples during sample mounting. The peg-and-hook

method enables the sample to have an additional degree of freedom to adjust its sample orientation (in the case, it is not already oriented) to the axis of the main tensile force. This ensures that samples do not inadvertently fail from forces other than tension. While the sample is tensed, marks on the sample made by a marker are tracked by way of an external video camera for strain measurements and frames of the sample are recorded for analysis. The velocity of the tensing is controlled by custom programmed software on a computer and a motor controller to keep the sample under a quasi-static loadng state such that inertial effects during loading are negligible. Typically, tensile loading occurs at a strain rate of 0.2 μm/s until the sample fails. The stress is measured by a load cell and recorded simultaneously to correspond to a strain value [100]. After such a measurement, a stress-strain behavior characteristic of the material is produced and analysis of typical parameters such as elastic modulus and ultimate tensile strength occurs from the recorded measurements.

3.2.2 Strain evaluation

Strain analysis comes about from tracking marks on the sample during tensile measurements with a video camera (Basler A101f, Basler Vision Technologies, Ahrensburg, Germany) and video extensometry software. The technique, unlike traditional strain detection methods in utilizing strain gauges [10], is non-contact. In any method of strain analysis, an initial length ($l_\circ$) and an end length (l_f), corresponding to length before and after stress, are supplied to describe the strain in the material: $\varepsilon = \dfrac{l_f - l_\circ}{l_\circ}$. The actual measurement of strain entails keeping track of the marks and assuming the marks themselves do not evolve via custom video applications (Labview 7.0, National Instruments, Munich, Germany) (**Figure 3.9**). Two implementations of this method have been used. The first is a simple tracking of marks based on contrast difference between the marks (black) and sample (white) and in essence, tracking the edges of the marks and using these edges as landmarks for strain. The downside of this method is the requirement for high levels of contrast, making illumination and optical recording of
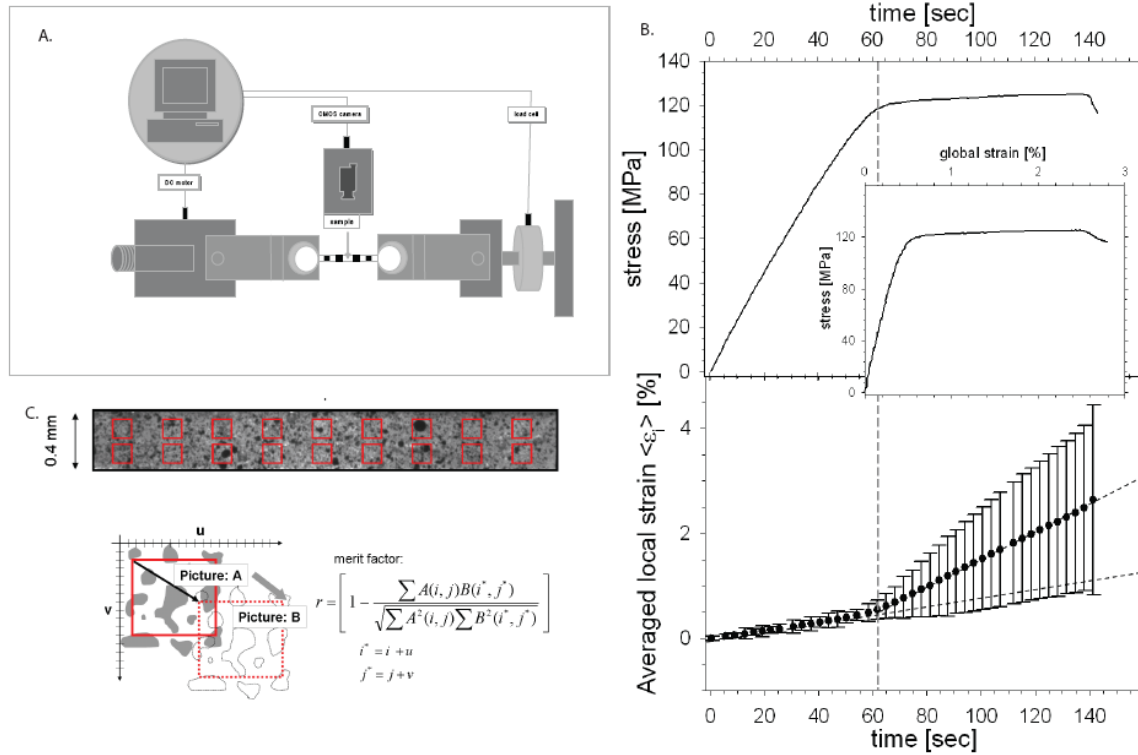
Figure 3.9 Strain detection from video extensometry. (**A.**) Schematic of the strain detection system used to track strains and correlate to forces applied to the material during mechanical tensile measurements (**B.**) Stress-strain curve of a typical cortical bone sample with the strain measured by video extensometry and the associated average strain evolution in the sample with time (**C.**) With digital image correlation, landmarks in the sample microstructure are tracked and sample strain measured with time [Adapted from Benecke et al. JMR 2009].

the measurement important. In fact during any material deformation, the texture of the material dramatically changes also affecting the illumination and subsequently, the contrast differences between the sample and the marks are diminished. This problem often occurs and is most severe just moments before material failure. To address this situation, another tracking method is used to follow the evolution of the marks on the sample during deformation [100]. The sample is overlaid with an electronic grid pattern that covers the entire gauge length of the tensed sample. Each grid tracks a local region of the sample and strain is determined from the displacement to the next square (**Figure**

3.9). Depending on the placement of the grid pattern, strain values are determined along the x- and y- axis. The mechanism by which this method is able to efficiently track marks on the sample is by having each grid in the pattern act independently from each other— each grid moves randomly in all directions ~8 pixels to predict where the local region might move in the next recorded frame. Thus, this method enables tracking strain of a sample that undergoes large amounts of displacement, heterogeneously throughout the sample.
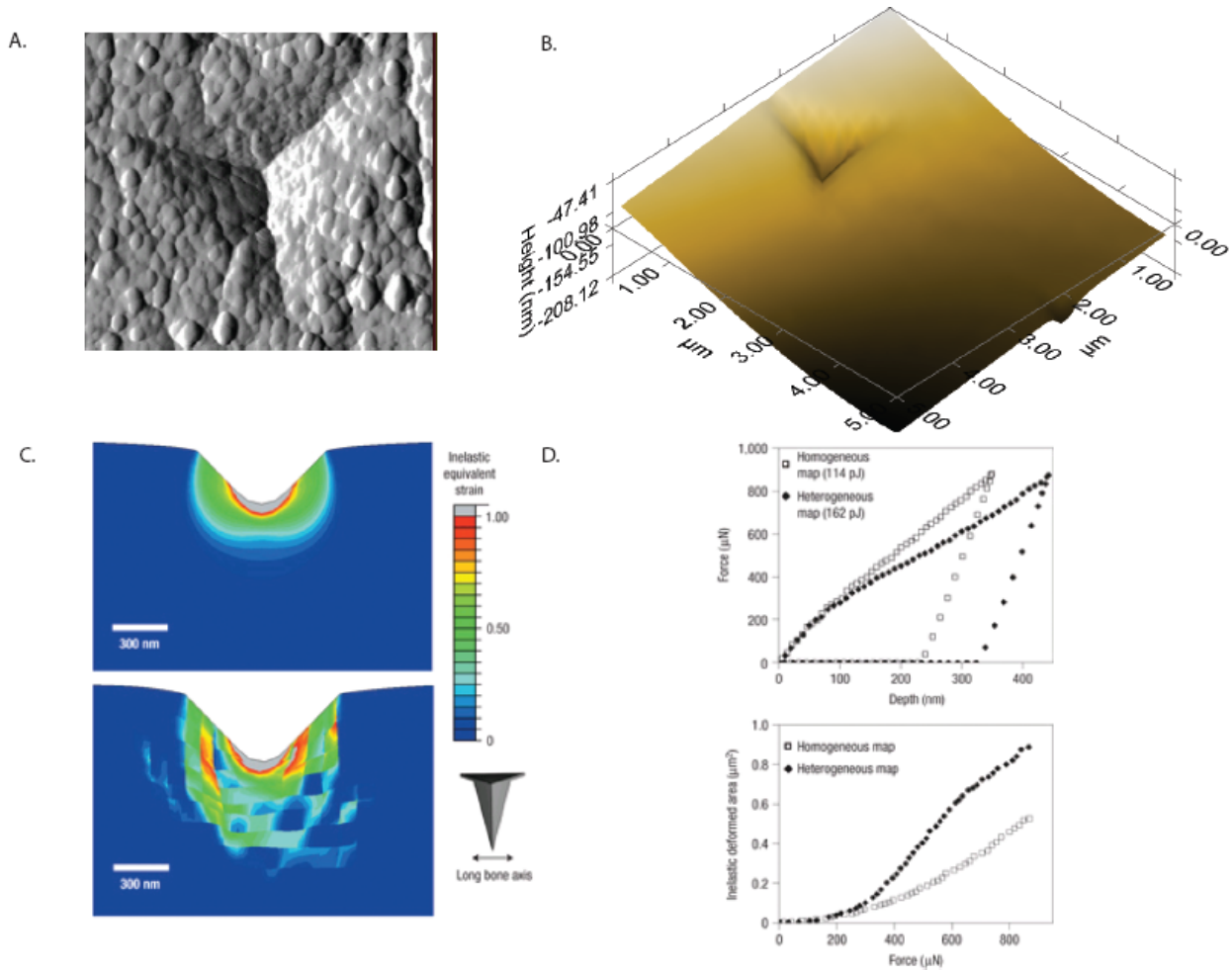
3.2.3 Nanoindentation

Nanoindentation (NI) is a mechanical characterization technique that requires a planar surface with roughness < 1 μm. An indenter in the form of a Berkovich tip (**Figure 3.10**) approaches the surface of the material at a constant force and deforms an area for a given amount of time. During this process, the Berkovich tip is mounted onto a piezoelectric sensor, a force feedback loop is established and the NI system (Ubi 1, Hysitron Inc., Minneapolis, MN, USA) detects the amount of force exerted by the material. This measure is the source of the hardness value obtained from the indentation. Afterwards, the tip retracts and leaves a pattern, typically in the form of the tip. By measuring the dimensions of the indent in the material, a value of hardness is derived as well. Although NI may not provide bulk information of the material since the volume of indentation is small (~100 μm^3). Typical quantities obtained from NI are hardness and a hardness derived elastic modulus values. The following are hardness H and a reduced modulus E_r derived from H:

$$H = \frac{P_{max}}{A}$$
(**Eq. 3.1**)

such that,

$$E_r = \frac{1}{\beta} \frac{\sqrt{\pi}}{2} \frac{S}{\sqrt{A(h_c)}}$$
(**Eq. 3.2**)

Figure 3.10 Nanoindentation of cortical bone. (A.) A typical indentation tip is the Berkovich tip, a three-sided pyramidal tip **(B.)** A typical contour map of the nanoindentation on the surface **(C.)** An finite element model simulating the effects of the NI tip on the material **(D.)** Force-displacement and area-force curves are used to evaluate materials properties like elastic modulus and hardness of the indented material. [Adapted from Tai et al. Nat Mat 2006].

where P_{max} is the maximum load, A is the contact area, E_r is the effective modulus, S is the stiffness of the contact, h_c is the depth of the residual indentation, β is a correction factor for the Berkovich indenter type. E_r is related to the elastic modulus of the material by the following equation [101] [102]:

$$\frac{1}{E_r} = \frac{1-v^2}{E} + \frac{1-v_i^2}{E_i}$$
(Eq. 3.3)

Where v_i and E_i are the Poission's ratio and elastic modulus of the indenter and v is the Poisson's ratio of the measured material [101]. Since the materials properties of the indenter is typically known, the evaluation of the elastic modulus of the sample material can be obtained under several assumptions about the sample material. The main assumption presumes the sample material is isotropic and perfectly linear elastic with no significant inelastic regime, which is not the case in bone.

Typical values of the indentation modulus obtained for bone are in the 15-30 GPa range, depending on the state of the material - whether the sample is from an older person, whether it is measured in humid conditions, and the orientation of the main collagen fiber axis with respect to the measurement. However, the interpretation of the actual measurement results as well as the mechanism in which the indentation occurs is not fully understood. Specifically, the behavior of the material as the indenter makes contact with the sample is not clear. Examples of these complexities are typified by nanoindentation measurements of a material where material "pile up" occurs at the indentation site. This occurs when forces applied by the indenter is in the form of a gradient from the surface towards the bulk. Many groups have utilized computer simulation such as finite element modeling in attempts to understand fully these scenarios during nanoindentation (**Figure 3.10(C.)**), but such techniques do not definitively resolve the questions related to the response of a material due to interactions with the NI.

3.3 Characterization of the Microstructure

3.3.1 Optical microscopy

To visualize structures in a material, such as damage induced by a mechanical measurement or the inherent structure which may explain specific materials properties, polarized optical light microscopy (DM RXA2, Leica Microsystems GmbH, Wetzler, Germany) is used as a cursory analysis tool to examine the microstructure (**Figure 3.11**). By polarizing the incident light such that all the emitted light is in the same oriented
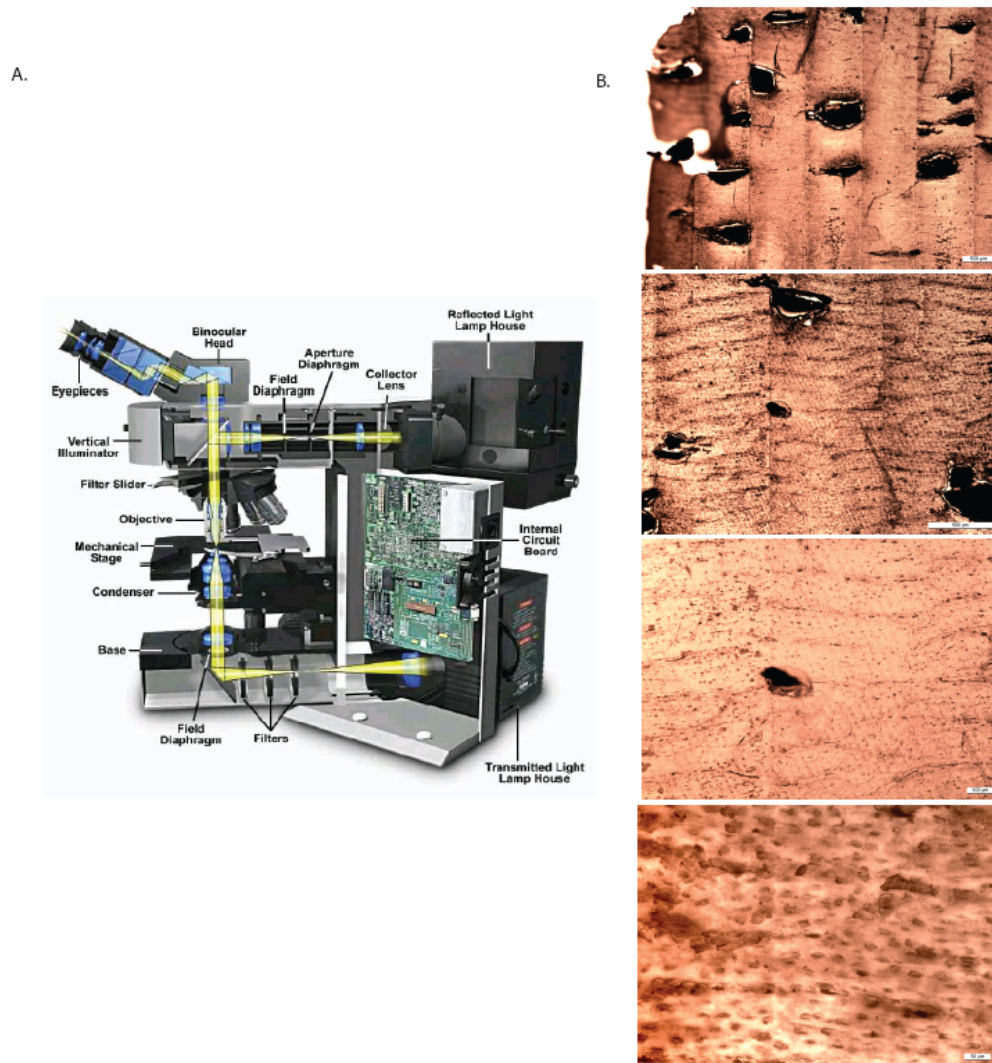
Figure 3.11 Evaluating material micro-structural changes with optical light microscopy. (A.) A typical schematic of a light microscopy with several lens objectives and optical filters (**B.**) Observation of damage in fibrolamellar bone from intense laser heating at several objectives, from the level of the tissue showing large swaths of calcined regions to the individual fibrolamellar unit showing burn damage at the fibrolamellar unit interface.

phase, structures in materials that are assembled in preferential directions, crystalline materials like bone, are optically anisotropic and are observed with polarized light. Specifically, in most organized crystalline structures, the effect of birefringence is encountered due to their optical anisotropies. Birefringence occurs when the linearly

polarized light interacts with the sample material such that two parallel light waves, an ordinary wave and an extraordinary wave, are produced to create a double refraction effect. Furthermore, the preferential arrangements in materials can also be observed by the preferred angle of polarized light. The angle of the entering polarized light can also be adjusted to allow only specific angles of polarized light to the sample, modulating the intensity of such an effect like birefringence. The ability is especially useful when the sample itself is embedded in a medium that reflects light with a different reflective index, i.e. water or plastic embedding medium, angular polarized light is adjusted to extinguish this background light and enhance the visualization of the sample.

Many of the materials examined have an organic component that does not have many optical properties. With the use of fluorescent probes such as rhodamine, synthetic dyes with adhesion to specific chemical groups are used to label organic components of interest in materials. Endowing the organic component with an optical label allows not only for visualization but, as well as localization within the materials bulk structure. These probes have unique properties - requiring specific excitation energies (**Figure 3.11**) and conformational structures to make these compounds fluoresce. Together with polarized light microscopy, florescent probes delineate the roles of the organic component in the organization of the material - understanding the interactions between the organic and inorganic in developing structure.

Optical microscopy takes on many variants and will be mentioned again in subsequent sections. These variants include the different modes of optical microscopy which are utilized to further enhance particular details in the material. The main modes are reflective and transmission mode optical light microscopy. These two modes provide different, but complementary information on a material. In the case of reflective mode microscopy, the main light source is exposed to a surface of the material and the reflecting light is what is collected and observed. This mode of microscopy enables for detailed examination of the material surface and details that may be hard to observe in transmission mode, such as surface cracks or roughness (**Figure 3.11(B.)**). In contrast, transmission mode light microscopy typically directs light through the material and the the transmitted light passing through the material is captured and used for analysis. This latter mode enables for examination of the bulk material.

3.3.2 Scanning electron microscopy

At higher resolving power, the scanning electron microscope provides an instrument that can bridge imaging the micro- and nano- structures in a material, like visualizing single nano-scale mineral platelets in bone. With the ability to create an image with an electron beam, the scanning electron microscope (Gemini 1550, LEO Electron Microscopy Group, Oberkochen, Germany) creates an image from rastering of an electron beam onto a sample (**Figure 3.12**). The deflected beam is then detected by a sensor capable of differentiating the velocities of each electron deflected. A computer takes this and creates an image that corresponds to the sample. The ability to scan a sample with an electron beam was limited due to the sample being too nonconductive or too intolerant to the electron beam. With the advances in modern sample preparation and electron microscopy technology, environmental scanning electron microscopes can now be used to accommodate electron beam sensitive materials. Instead of a high vacuum, the electron beam inside an ESEM encounters a chamber filled with water vapor. This enables the sample to be hydrated, unlike in a traditional SEM where the samples are dehydrated and coated with a layer of metal, as well as uncoated. In addition, the usual ESEM chamber is large enough to account all sizes of samples as well as supplemental device to perform in-situ measurements. As seen in **Figure 3.11(B.)**, the damage to the material as observed at higher magnification in the ESEM (Quanta FE-ESEM 600, FEI Company, OR, USA) in **Figure 3.12(B.)**, showing cracks induced by a burning of the organic component in bone. In this specific case, due to the inherent shorter wavelengths of the electron beam, imaging with the ESEM can accommodate at least 100X higher magnifications compared to the optical microscope. Additionally, with a backscatter detector in an ESEM, a quantitative measure of the material's density is also accomplished. For example, a sample that has regions containing differing amounts of mineral is detected with the BSEEM. Other detectors such as X-ray detectors can also be installed into the ESEM for elemental analysis like EDAX or EELS measurements.
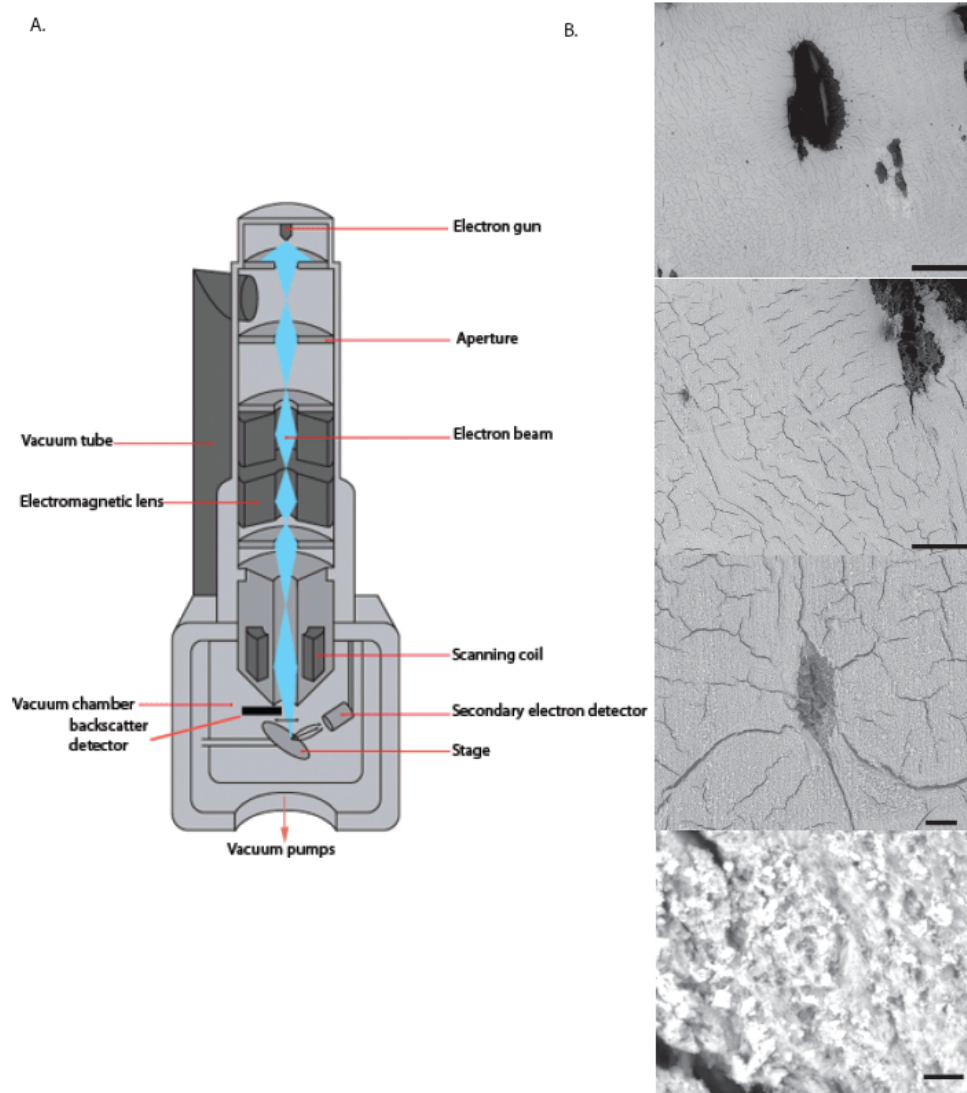
Figure 3.12 Use of scanning electron microscopy for high resolution imaging of surface microstructure in bone. (A.) A schematic diagram of a typical scanning electron microscope with various detectors **(B.)** Burn damage in bone caused by high energy laser beam observed at several magnifications under backscatter electron microscopy showing cracks in the material at several length-scales (scale bar: from top to bottom 400 μm, 100 μm, 20 μm, 2 μm, respectively).

3.3.3 Confocal laser scanning microscopy

Laser confocal microscopy (CLSM Aristoplan, Leica Lasertechnik GmbH, Heidelberg, Germany) is an optical technique which obtains high resolution images, but in combination with a tunable laser and the ability to adjust the focal plane,
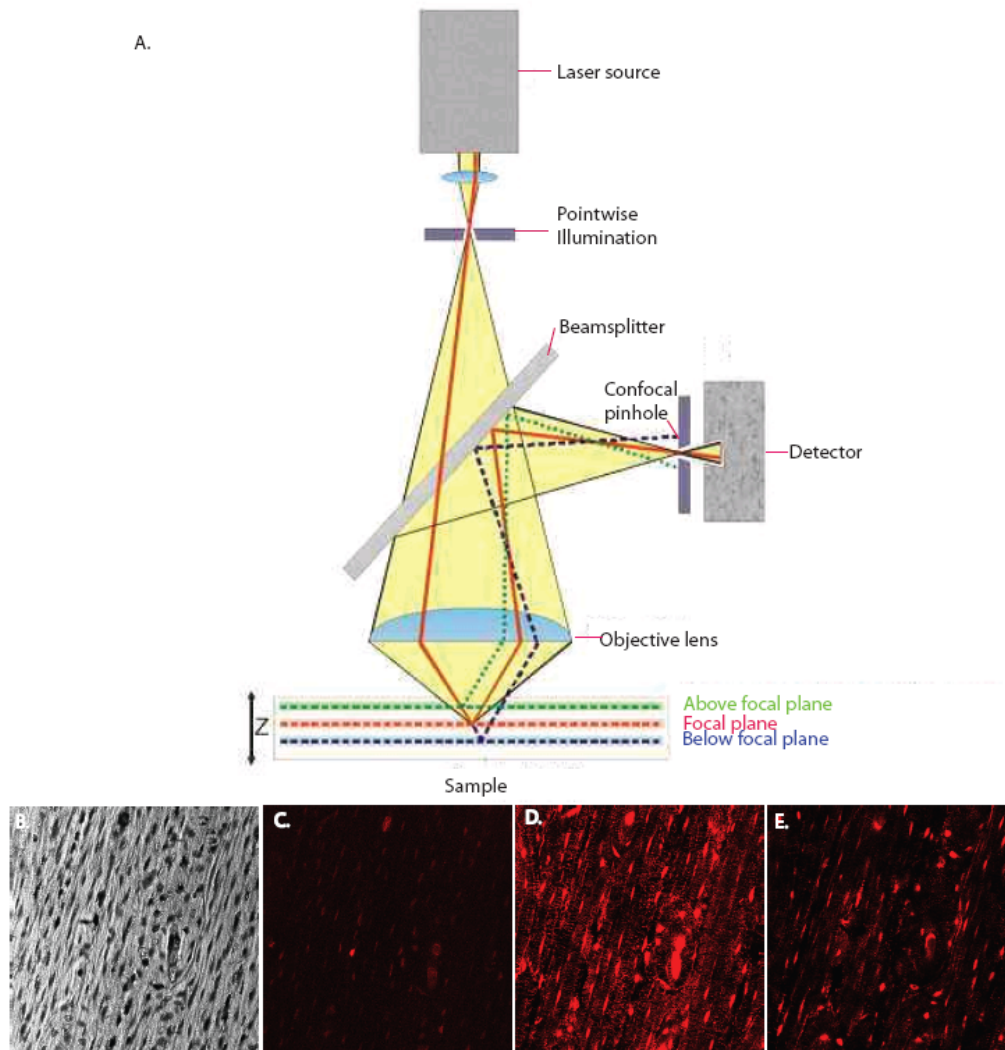
Figure 3.13 Laser scanning confocal microscopy to observe microstructure. (A.) A schematic diagram of the imaging process in confocal microscopy (**B.**) An optical image of cortical bone showing the microstructure predominately populated by osteocytes and blood vessels (**C.**) Using rhodamine-B as a contrast stain, the sample in (B.) imaged above the focal plane (**D.**) imaged in the focal plane (**E.**) sample shown below the focal plane.

images obtained by confocal microscopy can have depth selectivity (**Figure 3.13**). This requires a transmission mode scheme to be able to accomplish this depth selectivity. Using a fluorescent probe that is excitable by a specific laser wavelength, selected regions with a Z-axis perspective is analyzed. Typically, the total depth that is penetrated is approximately 10 μm. Thus, a measurement would involve collecting several frames through the depth of a material. An example of a typical bone section labeled with rhodamine is shown with the different planes of focus (**Figure 3.13(B)).** With reconstruction software, the images are assembled into a 3D volume showing the amount of fluorescence through the material.
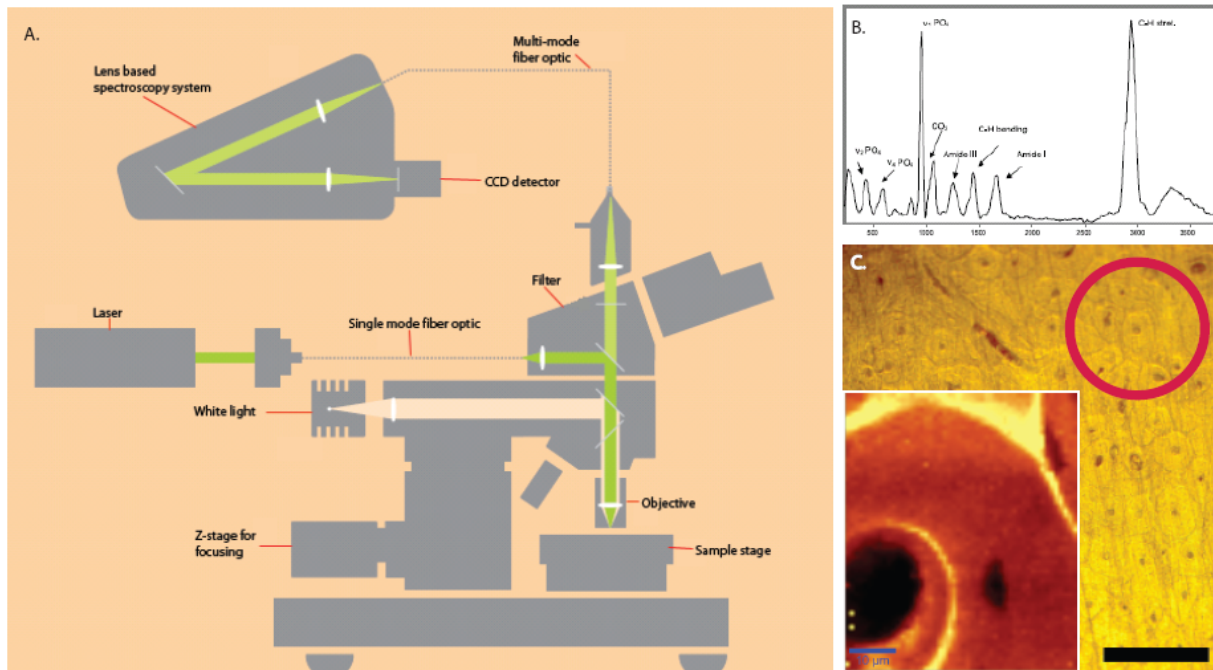
3.3.4 Raman microspectroscopy

Similar to the function of laser confocal microscopy, Raman microspectroscopy (CRM200, WITec GmbH, Ulm, Germany) uses an intense, monochromatic laser beam to inquire about the vibrational and/or rotational modes of molecules in the material in a volume of ~1 μm^3 (**Figure 3.14(A.)**). Specifically, photons from the emitted light source are either absorbed, reflected, or scattered. Only from the scattered light is a Raman shift detected. The source of this Raman shift is the inelastic scattering from a photon interacting with a molecule in the sample in such a way that the molecule is polarized. This polarization state can be summarized in the following equations [103]:

$$\mu_{in} = \alpha E \qquad \textbf{(Eq. 3.4)}$$

where μ_{in} is the induced dipole moment, α is the polarizibility from an electric field E
This relationship describes the polarization state of a molecule as a photon interacts with it. The first cosine term, ν_{in}, relates to the elastic Raleigh scattering that is equal to the frequency of the incoming light. The second cosine term, $\nu_{in}+\nu$, relates to the scattered photon that increases frequency by an amount, ν, which is the frequency of them of the molecular vibration. The third cosine term, $\nu_{in}-\nu$, relates to the photon that decreases frequency by an amount, ν. The increase and decrease in frequency shifts are characteristic of specific molecular vibrations. The essence of Raman scattering of a molecule comes about from quantifying and analyzing these shifts (**Figure 3.14(B.)**).

Figure 3.14 Raman microspectroscopy used an imaging technique of bone microstructure (**A.**) Schematic of the Raman spectroscopy setup (**B.**) Raman results provide in addition chemical information of the sample (**C.**) Typical osteonal samples from cortical bone are imaged in Raman spectroscopy showing the chemical composition of the microstructure (inset: an osteon showing the lamellar layering of organics and mineral) (scale bar: 600 μm) [(A) from WiTEC user manual].

In extending single point Raman spectroscopy measurements, a distribution map of Raman scattering in an area from a sample is also feasible (**Figure 3.14(C.)**). In its imaging mode, the same principles of Raman spectroscopy are utilized, but are applied to an area. Instead of performing single point measurements, a specific sample area is rastered by a focused 1 μm laser beam for a chemical composition map of the material. Like confocal microscopy, the Raman micro-spectroscopy setup can also probe in- and out- of specific focal planes due to an effective depth penetration of 5 μm by the laser light source.

3.3.5 X-ray scattering and diffraction

Diffraction

Using a different measurement medium to characterize mineralized tissues, X-rays are used to probe the nanostructure of a material. A monochromatic electron beam is focused onto a small point region and used to raster a region of interest (Nanostar, Bruker

AXS Inc., WI, USA) (**Figure 3.15(A.)**). Like BSEEM, it can provide hints at the density of the material due to the measured absorption of X-rays from the primary X-ray beam. Most importantly, the scattering behavior of the X-ray beam transmitted through the material is able to provide information about the material nanostructure. When X-rays are transmitted through a material, the X-rays undergo a process of diffraction whereby the X-rays interact with the material. In the simplest case, when a material is a crystalline, ordered material such as a crystal, the behavior of the X-rays transmitted through this crystal is described by Bragg's law:

$$\lambda = 2d \sin \theta \qquad\qquad \textbf{(Eq. 3.5)}$$

where λ is the wavelength of the X-ray, d is the distance between crystal planes, and θ is the angle of the diffracted X-ray. This quantitative description of the X-ray interaction within the material allows for not only characteristics about the arrangement of the scattering centers in the material, but also information on the organization. In reciprocal space, Bragg's law is defined by the conservation of momentum transfer between the initial and final wave vectors, k_0 and k_f, such that that the scattering length $q=k_0-k_f$, with $k_0=k_f$ in elastic scattering. Since the scattering vector q in reciprocal space is described as the vector normal to the lattice plane with a length $q=2\pi/d$, Bragg's law in reciprocal space becomes:

$$q = \frac{4\pi \sin \theta}{\lambda} \qquad\qquad \textbf{(Eq. 3.6)}$$

Small-angle scattering

A typical measurement provides a scattering profile in q-space (reciprocal space) representing the measured sample region of interest. Specifically, the scattering intensity as a function of q-range in a two phase material is shown as

$$I(\vec{q}) = I_0 * (\rho_\alpha - \rho_\beta)^2 \left| \int_V \sigma(\vec{r})e^{i\vec{q}\vec{r}} d\vec{r} \right|^2 \qquad\qquad \textbf{(Eq. 3.7)}$$

where I_0 is the initial intensity of the X-ray beam before exposure to the sample, ρ_α is the electron density of the α phase, ρ_β is the electron density of the β phase, σ is a step function such that if $\vec{r}$ is in α phase it is 1, else it is 0.
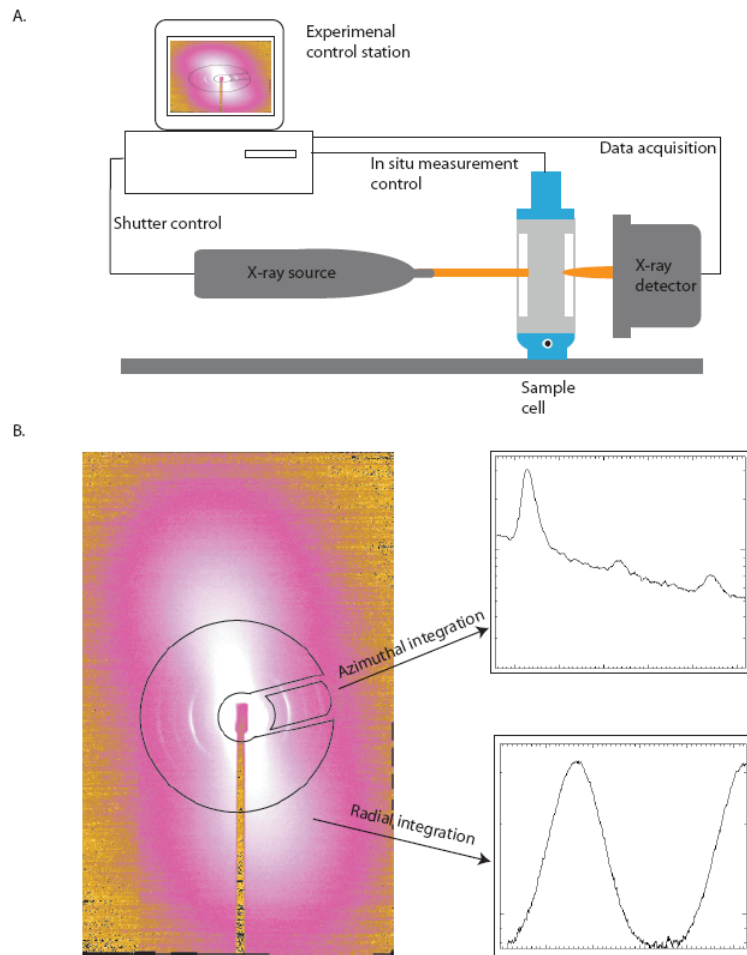
Figure 3.15 Small-angle X-ray scattering (SAXS) as a method to probe the materials properties in bone (A.) A schematic SAXS setup shown in a typical experiment (B.) Analysis of the SAXS data can provide information about the dimensions (via radial integration- T-parameter) as well as the orientation (via azimuthal integration-Rho parameter of the constituent materials.

At certain detection regimes called the small-angle X-ray scattering (SAXS) regime, information about the constituent size and orientation are measured. Outside this regime, wide-angle X-ray diffraction (WAXD) is predominant and provides information about the crystalline lattice structures involved in the material. Typically, structures which are in the range of 1-100 nm are in the SAXS regime, whereas those in the 0.1-1 nm are in the WAXD regime (**Figure 3.16**).

3.3.5.1 T-Parameter

The analysis of the small-angle X-ray scattering profiles can provide two parameters which describe the orientation and thickness dimension of the constituent materials in the sample. In the case of bone, the scattering profile will consist of reflections from the mineralized collagen peaks and an elliptical mineral peak. To obtain a quantitative value that describes the thickness dimension of the constituents with respect to the measurement frame, the scattering profile is azimuthally averaged along the mineralized collagen to obtain an intensity to q-range (inverse nm) plot (**Figure 3.15(B)**). This plot clearly shows the varying intensities of the different orders of diffraction from the mineral in the mineralized collagen i.e. 1st, 2nd, and 3rd. To evaluate this data to obtain a value that has a physical meaning, the following expression establishes a relationship of the smallest dimension of the mineral platelet, T parameter, in the material to the scattering behavior [37] [104, 105] [38]:

$$T = \frac{4}{\pi * PC} \int_0^\infty q^2 S_{PBcorr}(q)dq \qquad \textbf{(Eq. 3.8)}$$

the Porod constant PC, the Porod background PB, the radially averaged and background corrected intensity S_{PBcorr}, and as well as a meaningful q-range are determined to solve the integral such that

$$T = \frac{4}{\pi * PC}\left[\frac{q_{min}^3 I(q_{min})}{2} + \sum_{q_{min}}^{q_{porod1}} q^2 S_{PBcorr}(q)\Delta q + \frac{PC}{q_{porod1}}\right] \qquad \textbf{(Eq. 3.9)}$$

From the Porod evaluation [106], the function is filled in with the appropriate extrapolated values.

Furthermore, a shape function G(x) is used to validate the results of the T-parameter function. S_{PBcorr} is rescaled into a function G(x) that is independent of the T-parameter and takes into account the average shape, size, and spatial arrangement of the

Figure 3.16 Wide-angle X-ray diffraction of bone. (**A.**) In addition to the SAXS regime, depending on the measured q range, the WAXD signal is obtained to determine the chemical composition as well as the lattice structures in the materials (**B.**) A typical WAXD pattern of bone shows predominant signals in the (002) and (310) lattice planes and produces data that are analyzed to determine orientation of the mineral.

mineral as parameters. Thus,

$$S_{PBcorr} \Rightarrow G(x) = Kq^2 S_{PBcorr}(q) \qquad \textbf{(Eq. 3.10)}$$

such that x=qT and K is evaluated such that $\int_0^\infty G(x)dx = 1$. G(x) curves are used to

compare relative differences for hints at differences in any of the aforementioned parameters, including differences in size [107].

In another formulation of the above equations, in bone it can be assumed to be a biphasic material consisting of organic and mineral components, such that **Eq. 3.7** can be simplified to

$$T = \frac{4\phi(1-\phi)}{\sigma}$$ **(Eq. 3.11)**

whereby ϕ is the volume fraction of the mineral platelet and σ is the surface area per unit volume. Typical values of the T parameter in bone range from ~1.8-2.5 nm [105] [38] [108] [39].

3.3.5.2 ρ-Parameter

Another vital piece of information which is gathered from the radial integration of the scattering intensity profile, such that $I(q,\chi)$ is integrated with respect to q or 2θ, a resulting function $S(\chi)$ describes the periodic scattering intensity as a function of χ. The quantity which describes the degree of alignment, ρ parameter, is evaluated by determining the area under curve of the $S_{corr}(\chi)$, normalized and background substrated (Figure 3.15b). Assuming a Gaussian distribution, the function $S_{corr}(\chi)$ is fitted by a four parameter Gaussian distribution term to obtain parameters that describe the contribution of background A_0 to the $S(\chi)$ and as well as the corrected peak area A_1. The ρ parameter can then be evaluated as:

$$\rho = \frac{A_1}{A_0 + A_1}$$ **(Eq. 3.12)**

which quantifies the degree of constituent orientation in the material, with 0 indicating that all the constituents are entirely disordered and 1 indicating that all the constituents are perfectly ordered [38, 39].

The aforementioned X-ray techniques enable for a wide-range of applications as well as a wealth of information that is obtained from a material. Most importantly, with the advent and development of soft X-rays at synchrotron sources (ESRF ID2, BESSY Microfocus), materials that are normally prone to damage from exposure to too much radiation can now be characterized with these X-ray techniques at low flux. Biological materials can now be hydrated, via a cryostream or a monolayer of water, and their

structures probed with scattering techniques. Furthermore, these X-ray methods are extremely flexible techniques allowing for coupling of other experiments such that mechanical measurements are performed in-situ. As a result, the use of X-rays is a powerful tool that complements the microstructural information of a material with details at the nano-scale.

From the ability to evaluate mechanical behavior to the structure at the nano-scale, the tools that are available to characterize Nature's materials are readily available. Utilizing all the aforementioned techniques in this chapter, the structure and function of bone is probed from the nano- to the macro- tissue scales. With these techniques, the assemblage and organization of the hierarchical structure in bone with respect to its characteristic mechanical deformation behaviors, in its complete framework from the nano- to the tissue- length-scales, can be fully understood.

4 Results and Discussion

In this work, novel mechanical methods in conjunction with structural characterization techniques are used to probe the micro- and nano- scale properties of the material bone. These approaches enable for structural and functional features at the smallest length-scales to be delineated in order to establish structure-function relationships at several levels of the bone structural hierarchy. From the tissue- to the nano- length-scales, bone's hierarchical structure incorporates a diversity of strengthening schemes to utilize the mechanical properties of distinct constituent elements at each length-scale. At the tissue level, soft epithelial tissues as well as cellular sheaths enhance the amount of mechanical compliance in the tissue by inadvertently adding heterogeneity to the bone tissue. Continuing into the micro-scale, the existence of weak interfaces is found to prevent catastrophic material failure via inhibiting crack propagation. At the nano-scale, the mineralized platelets and collagen fibers are highly organized and oriented to provide characteristic mechanical anisotropy and strength (**Chapter 2**) along the mechanical loading direction. These structure-function relationships in the material bone are explored to understand the assemblage and organization of its constituent elements over several length-scales, but most importantly, to comprehend the utilization of the hierarchical structure in the mechanical deformation mechanisms of the material bone. In this chapter, the structure and function of bovine and murine cortical bone models are investigated to understand the various structural origins of properties such as strength and toughness in the material bone.

4.1 Mechanical properties of bovine cortical bone

By using a diverse array of mechanical techniques, from nanoindentation to uni-axial micro-tensile measurements, empirical materials properties at several length-scales in the hierarchical bone structure are obtained. In this section, the materials properties as well as the mechanical behavior of the "bricks" in the brick layer structure of bovine
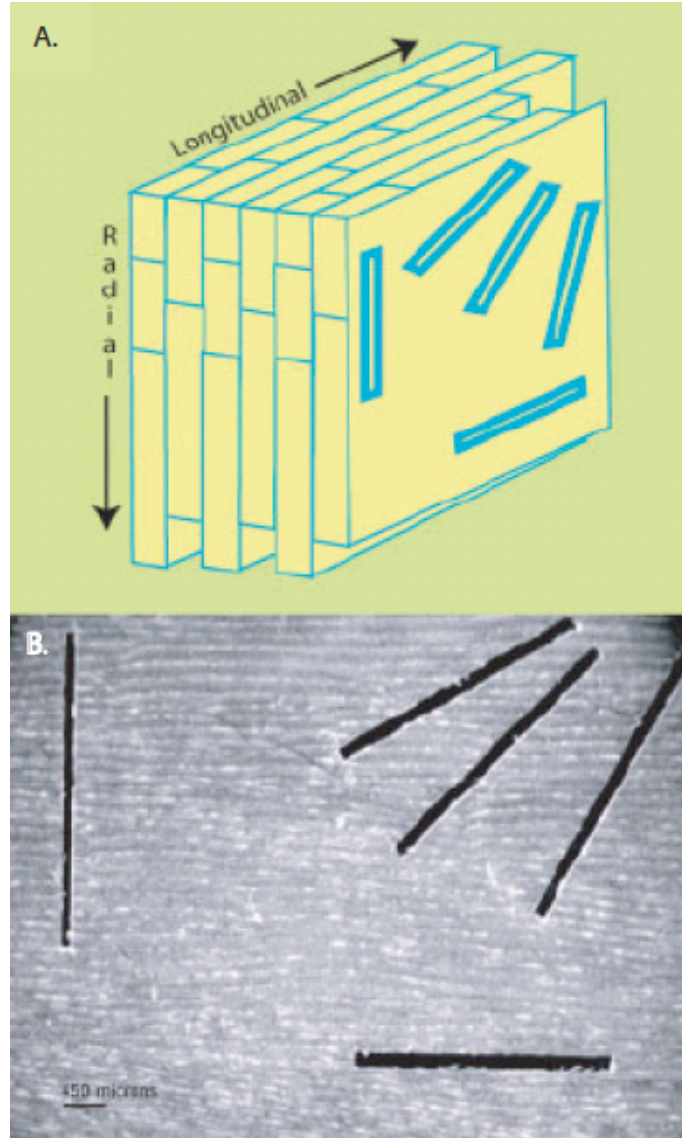
Figure 4.1 Orientation effects of fibrolamellar bone. (**A.**) A schematic diagram of fibrolamellar bone units with respect to the orientation of the tissue, such that 0° is along the main bone axis (**B.**) Optical microscope image of sample orientations sectioned by UV laser micro-dissection used for micro-tensile measurements.

fibrolamellar bone, units termed fibrolamellar bone units are described (**Figure 4.1**). In measuring typical materials properties such as elastic modulus, yield point, hardness, and ultimate tensile strength at the micro- and nano- length-scales, the contributions of structures at these length-scales to the overall mechanical behavior of bone can be determined.   Furthermore, these materials properties are also examined under various states of orientation and hydration since normal physiological loading conditions of bone

tissue occurs in both a hydrated environment and with mechanical loads not always being on-axis. In addition, the effects of scaling on these properties are also examined. The following sections describe results of experiments that establish the critical role of the structural hierarchy in the deformation mechanisms of fibrolamellar bone at the micro- and nano- length-scales.

4.1.1 Nanoindentation

In this section, experiments using nanoidentation to probe the elastic and hardness properties (**Chapter 3.2.3**) of fibrolamellar bone in different orientations in the radial-longitudinal plane are described. NI sample planes are oriented at angles in degrees of 0°, 30°, 45°, 60°, and 90° with respect to the main bone axis (**Chapter 3.1**). All these measurements are performed in the dry state.

Utilizing NI, cursory measurements of bone's materials properties typically from a surface volume surrounding the indent area of ~10 μm^2 is made (**Figure 3.10**). From a typical NI measurement, an indentation modulus and a hardness value are calculated. These values are related to an elastic modulus as well as the yield stress of the material. Specifically, measurements along the transverse plane of the longitudinal bone axis reveals a hardness and elastic modulus of 0.678 GPa ± 0.0741 (mean ± S.E.M, from this point, all errors will be expressed in S.E.M.) and 23.1 GPa ± 1.32. By slightly varying the orientation of the samples (**Chapter 3.2.1**), NI measurements are found to decrease accordingly. The range of values in these off-axis measurements of hardness and elastic moduli are from 0.7-0.5 GPa and 10-23 GPa, respectively (**Figure 4.2(A.),(C.)**).

In systematically varying the orientation of the sample, NI is used to investigate orientation effects in bulk fibrolamellar bone by observing changes in both indentation modulus and hardness as a function of the loading direction. When taking NI measurements at incremental angles away from the main bone axis (also the main collagen axis), a decrease in indentation modulus is observed. Specifically, at angles from 0° (parallel to direction of the bone axis) to 30°, a 6% decrease from 23.11 GPa (0°) to 21.66 GPa (30°) is observed in the elastic modulus. By increasing the angle away from

the main bone axis to 45°, the difference between elastic moduli at 30° and 45° is a decrease that is ~26% with 21.66 GPa (30°) to 16.11 GPa (45°). A further increase in the orientation angle away from the bone axis to 60° shows an exception to the decreasing trend in elastic modulus with increasing orientation angle. At 60°, the elastic modulus is found to be 18.39 GPa, an ~14% increase from the measured value of 16.11 GPa at the 45° orientation. This result is explained by the innate structuring of the elastic organic matrix and the stiff mineral whereby at 45°, such that shear stresses in the material are at its maximum. When increasing the angle towards the 60° orientation, the shear stresses decline and the material stiffness appears to increase. This false impression of an increase at the 60° orientation is only a result of the dramatic decrease in stiffness at the 45° orientation. By increasing to the 90° orientation, an elastic modulus of 15.44 GPa is found, indicating ~16% decrease from the 60° orientation. In general, the elastic moduli values decrease when measuring at angles increasing away from the main bone axis.

Hardness also follows the same decreasing trend observed in the elastic moduli. However, when progressing from 0°-30°, rather than a decrease, an increase of ~7% from 0.678 GPa (0°) to 0.724 GPa (30°) occurs although hardness and indentation modulus values are inherently inter-dependent (**Chapter 3.2.3**). This observed increase is statistically insignificant (P=0.940). Thus, as a result of sampling error, the unusual divergence between 0° and 30° in hardness is ignored and a decrease in measurement values of their true hardness values is expected. When examining the hardness values at 30° and 45°, values of 0.724 GPa ± 0.4569 and 0.567 GPa ± 0.0288 are obtained, respectively, showing ~13% decrease. At 60°, as similarly observed in the elastic modulus of the same angle, the measured hardness value is partially recovered at 60° when compared to the 45° orientation. The difference between 0.567 GPa (45°) and 0.662 GPa (60°) is ~17%. Dramatically, the hardness values at 60° and 90° orientations decreases approximately 24%. As expected, the trends observed in the hardness values at increasing angles away from the main bone axis decrease in a similar manner as observed in the elastic moduli.
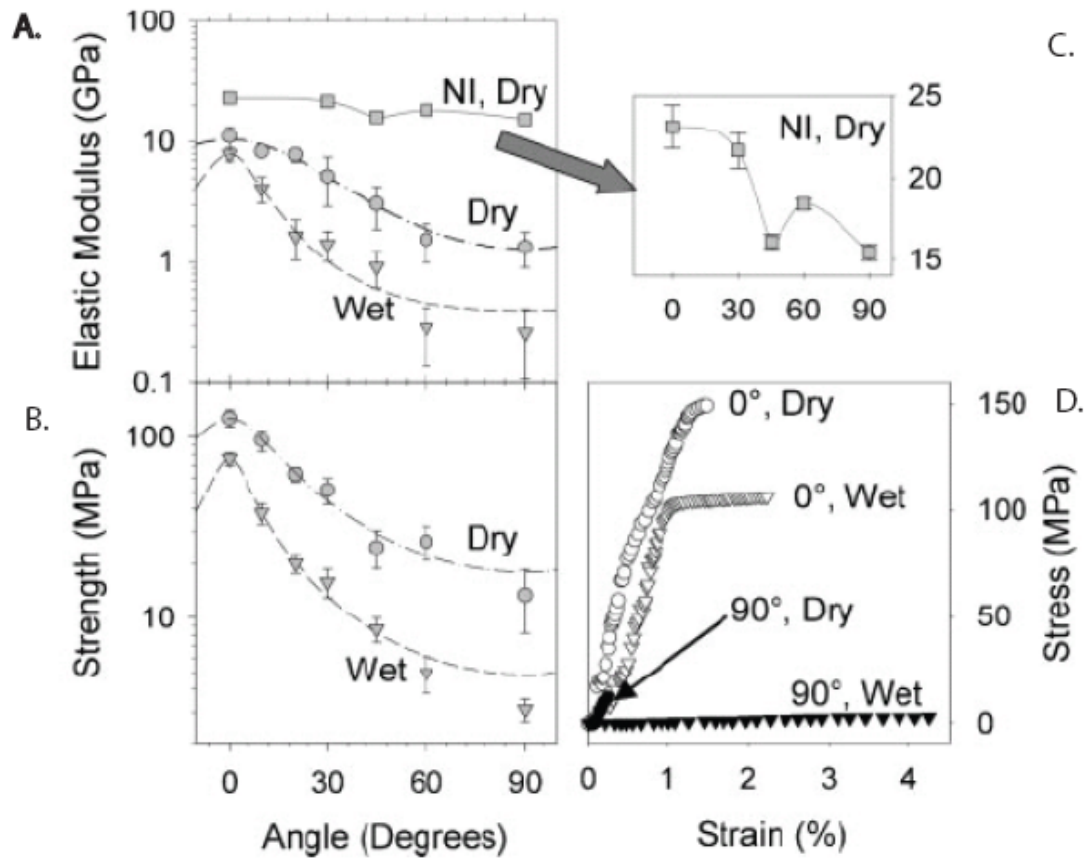
Figure 4.2 Mechanical measurements of samples in fibrolamellar bone. (A.) A compilation of elastic moduli from samples measured by NI as well as micro-tensile measurements in dry and wet conditions as a function of collagen fiber orientation **(B.)** A comparison of the micro-tensile strengths as measured in dry and wet conditions **(C.)** Zooming in on the NI data, one can observe a local minimum that occurs between orientations at 45° **(D.)** A stress-strain plot of typical samples at 0° and 90°, in dry and wet conditions.

The NI measurements indicate decreases in both the elastic modulus and hardness values when increasing the angle away from the main bone axis. The differences between the maximum and minimum values of both elastic moduli and hardness are summarized by ratios at 0° and 90° orientations, which are found to be $\frac{E_{0°}}{E_{90°}} \approx 1.50$ and $\frac{H_{0°}}{H_{90°}} \approx 1.35$.

These ratios quantitatively describe the degree of mechanical anisotropy measured from the elastic modulus and hardness by NI. It must be also noted that these NI measurements are made onto bulk pieces of cortical bone tissue, such that the NI measurements actually

represent properties of near surface volumes and are also partially averaged over several fibril orientations. As a result, the microscopic NI results are influenced by structural features from the tissue level due to the inherent features in the sample. In the next section, homogenous constituent elements in fibrolamellar bone are mechanically characterized by micro-tensile measurements to accurately assess the materials properties at the micro-scale.

4.1.2 Micro-tensile measurements

In this section, uni-axial tensile measurements performed on single fibrolamellar bone units are also examined. Single fibrolamellar units sectioned from bone tissue at angles of 0°, 10°, 20°, 30°, 45°, 60°, and 90° away from the main bone axis are investigated by micro-tensile measurements. In contrast to NI measurements, the effects of hydration on these materials properties are also be examined. In each case, whether it is in the dry or wet states, all the aforementioned orientation angles are measured by micro-tensile measurements as mentioned in **Chapter 3.1**.

Orientation effects of fibrolamellar bone in the dry state

In an effort to elaborate on the NI measurements, micro-tensile measurements are performed on single fibrolamellar units (**Figure 4.2(A.),(B.),(D.)**). Individual fibrolamellar bone components are isolated from the tissue and their materials properties characterized [96, 97] via uni-axial micro-tensile measurements at constant strain rate and tensed until failure (**Chapter 3.1.1, 3.1.2**). Typical micro-tensile measurements of fibrolamellar bone units are described in stress-strain plots (**Figure 4.3**) depicting deformation regimes in the mechanical behavior of the sample (**Chapter 2.8**). Specifically, from the stress-strain behavior, a characteristic elastic modulus and an
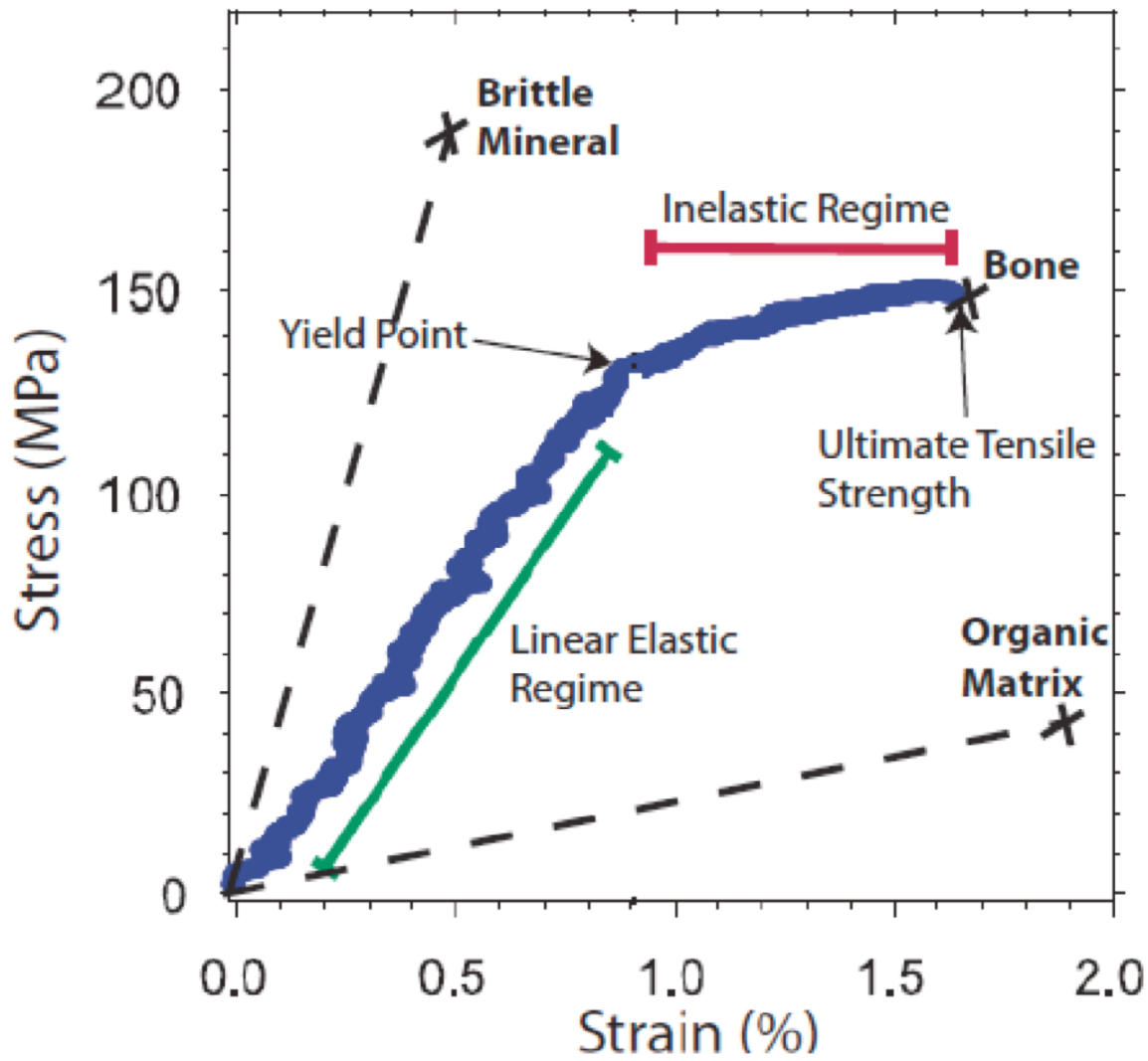
Figure 4.3 Typical stress-strain behavior of a fibrolamellar unit under micro-tensile loading As observed, the different elastic and plastic regimes depict the different deformation behaviors in the material, showing a yield point as the onset of plastic deformation and ultimately, failure of the material. Additionally, the idealized properties of the organic and mineral are superimposed with [Adapted from Gupta et al. PNAS 2006].

ultimate tensile strength (UTS) is obtained for each measured sample. In the following sections, orientation effects on single fibrolamellar units are performed by micro-tensile measurements at 0°, 10°, 20°, 30°, 45°, 60°, and 90° orientations from the main bone axis (**Figure 4.1(B.)**).

Micro-tensile measurements of fibrolamellar units oriented parallel to the main bone axis (0°) are found to have elastic moduli with a mean value of 11.1 GPa ± 2.22 (mean ± S.E.M.). When increasing the orientation angle gradually away from the main bone axis, the elastic moduli decrease accordingly, as observed from the NI measurements. At both the 10° and 20° orientations, the mean elastic moduli continue to gradually decrease. However, the mean elastic modulus at 30° is found to be 5.16 GPa ± 2.28, resulting in a decrease which amounts to ~34% between the 20° and 30° orientations. This decrease becomes larger at the 45° orientation, where fibrolamellar units are found to have a mean elastic modulus of 3.04 GPa ± 1.17, such that the difference between the 30° and the 45° orientation is a ~41% decrease. The most dramatic decline in elastic modulus occurs between the 45° and 60° orientation angles (**Figure 4.2(C.)**), where it is found that the mean modulus at 60° is 1.55 GPa ± 0.546, resulting in ~50% decrease from the elastic moduli at the 45° orientation. In incrementing to the 90° orientation, the elastic modulus levels out and a decrease of 14% occurs from the 60° to the 90° orientation. A measure of the decrease in magnitude from the maximum (0°) to the minimum (90°) elastic moduli value is represented by a ratio of the elastic moduli at 0° and 90°, which is found to be $\dfrac{E_{0°}}{E_{90°}} \approx 8.32$. The elastic moduli measured by micro-tensile measurements not only confirm a decrease of elastic moduli with increasing orientation angles away from the main bone axis, these measurements indicate that the orientation effects on elastic moduli in micro-tensile measurements are more dramatic in comparison to the moduli obtained from NI measurements.

A similar trend is also observed in the UTS at incrementing orientation angles from 0°, 10°, 20°, 30°, 45°, 60°, to 90° orientations measured away from the main bone axis via micro-tensile measurements (**Table 4.1**). The UTS at 0° is found to be 128 MPa ± 13.9 (mean ± S.E.M.) decreases with increasing orientation angles. However, at the 45° orientation, the UTS is found to be 24.5 MPa ± 5.88, resulting in a 52% decrease from the 30° orientation and an approximately 80% decrease from the 0° orientation. In contrast, at the 60° orientation, the UTS is found to be 26.4 MPa ± 5.66, an exception to the trend occurs such that an *increase* of 8% takes place between 45° and 60°. Similar to

the NI measurements at the same orientation angles, the divergence from the trend is very likely a result of sampling error. However, the UTS at the 90° orientation is found to be 13.3 MPa ± 5.10, resulting in a 50% decrease from the UTS at the 60° orientation. The magnitude of difference found in the UTS between the 0° and 90° orientations is $\frac{UTS_{0°}}{UTS_{90°}} \approx 9.59$. As in the case of the elastic modulus, the effects of orientation on UTS are found to be substantially significant.

Orientation effects of fibrolamellar bone in the wet state

To simulate more closely the mechanical loading in physiological conditions experienced by the material bone, micro-tensile measurements on fibrolamellar bone units are conducted in a hydrated environment. Under the same micro-tensile loading conditions, the effects of orientation are also investigated as a function of hydration. In the following sections, the orientation effects on the elastic modulus and UTS are examined in a hydrated state.

In the wet state, the elastic modulus at 0° is found to be 7.85 GPa ± 0.982 (**Table 4.1**). Like in the decreasing trends observed in the dry state, the elastic moduli decreases with increasing orientation angle and often, the decrease is greater than observed in the dry state. At increments of 10°, 20°, 30°, 45° relative decreases are approximately 48%, 60%, 14%, and 36% respectively, in the wet state. However, the largest decline in elastic moduli occurs between the 45° and 60° orientation states, with the elastic modulus at 60° being 0.281 GPa ± 0.141, such that the modulus at 60° is found to be 69% reduced from the modulus at 45°. Furthermore, incrementing the orientation from 60° to 90° reveals a 9% decrease in elastic modulus, with the elastic modulus at the 90° orientation being 0.257 GPa ± 0.150. The magnitude difference between the 0° and 90° orientations is represented by the ratio of elastic moduli at these respective orientations and found to be $\frac{E_{wet,0°}}{E_{wet,90°}} \approx 30.5$. This indicates that in a hydrated state, the orientation effects of the elastic moduli are far greater than in the non-hydrated state.
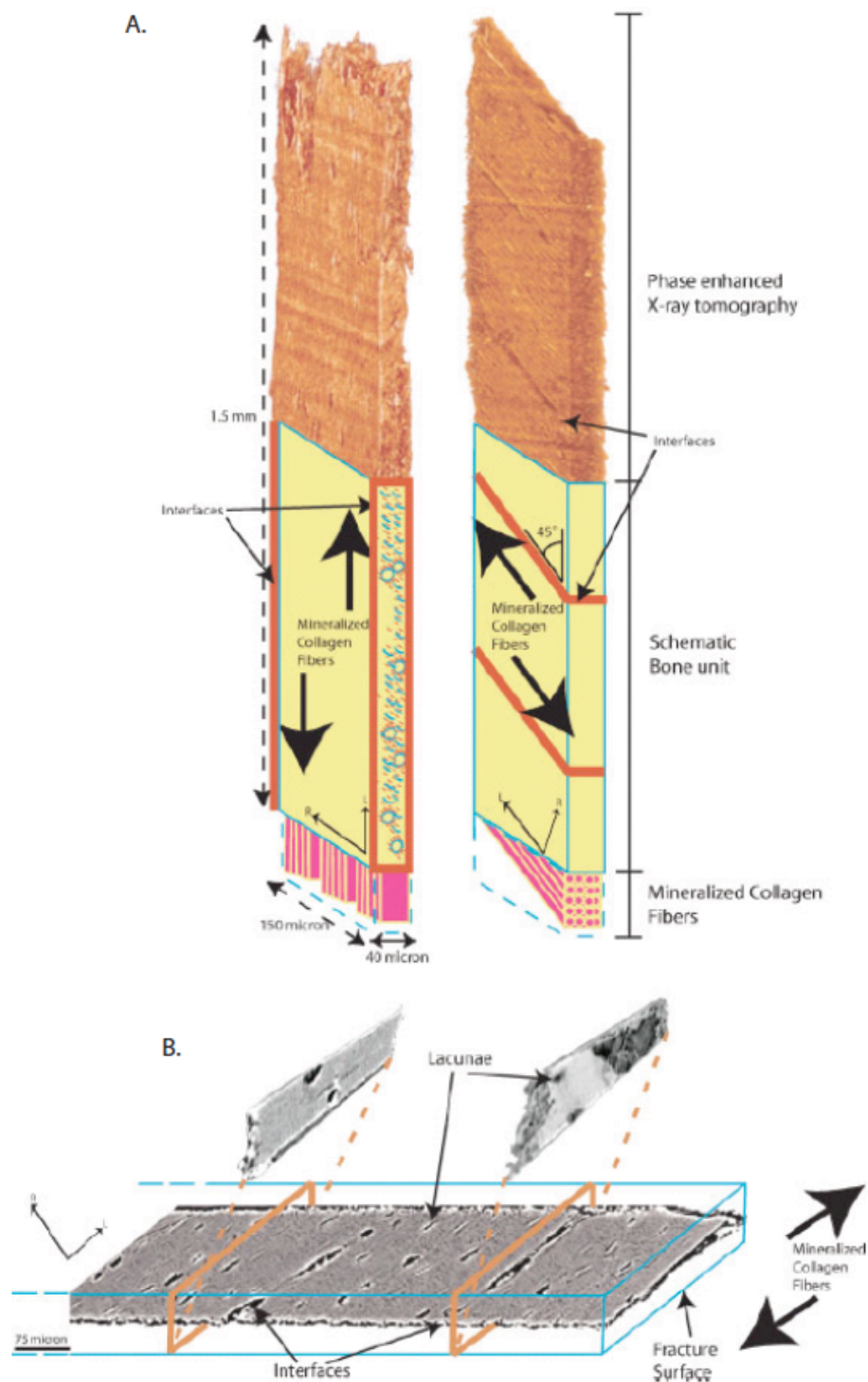
Figure 4.4 Schematic of a bovine fibrolamellar unit (**A.**) Schematic drawing of 0° and 45° oriented fibrolamellar bone units with respect to their interfaces and the main collagen fiber axis (**B.**) A X-ray tomography of a single fibrolamellar unit at 45° orientation show transverse sections through an area with and without an interface.

The UTS at 0° in the hydrated case is found to be 75.9 MPa ± 5.96 (**Table 4.1**). With increasing orientation angles away from the main bone axis, it is found that at 10° the UTS is 37.8 MPa ± 4.79. The relative difference from 0° is a decrease of 50%. This large decrease most likely represents a severe weakening of the material by way of an introduction of a material defect or exacerbating an existing defect. At subsequent orientations such as at 20°, the UTS is found to be 19.9 MPa ± 2.33 where the difference from the 10° orientation is approximately 47%. The degree of decrease becomes smaller with increasing angle such that at 30° and 45°, the relative decreases are found to be approximately 21% and 45%. Additional decreases in the range of 43% occur when increasing from the 45° to the 60° orientations, where the UTS at the 60° orientation is found to be 4.95 MPa ± 1.12. In addition, continuing to the 90° orientation, the UTS is found to be 3.11 MPa ± 0.438 such that the relative decline in UTS between 60° and 90° orientations is 37%. The ratio of the UTS at 0° and 90° is found to be $\dfrac{UTS_{wet,0°}}{UTS_{wet,90°}} \approx 24.4$.

This confirms the significance of orientation effects under hydration in affecting the strength of the material bone.

By increasing the angle of orientation of the fibrolamellar bone unit away from the main bone axis, the elastic moduli and UTS are observed to undergo a dramatic decrease whereby the ratios $\dfrac{E_{dry,0°}}{E_{dry,90°}}$ and $\dfrac{UTS_{dry,0°}}{UTS_{dry,90°}}$ are found to be approximately 8.32 and 9.59, respectively. Under a hydrated state, these ratios $\dfrac{E_{wet,0°}}{E_{wet,90°}}$ and $\dfrac{UTS_{wet,0°}}{UTS_{wet,90°}}$ are found to be approximately three-fold greater than the values in the non-hydrated state, resulting in values of 30.5 and 24.4, respectively. These values indicate a high degree of orientation and hydration sensitivity in fibrolamellar bone material. Specifically, when incrementing the orientation of fibrolamallar units away from the main bone axis, two notable structural features of the fibrolamellar bone unit change. These being: (1.) the orientation of the main collagen fiber axis and (2.) the inclusion of periodic weak interfaces. Since the orientation of the main collagen fiber axis is strongly associated to the main bone axis, such that the orientation of the main collagen fiber axis is always the

orientation of the main bone axis, micro-tensile measurements of fibrolamellar units further oriented away from the main bone axis are understandably weaker due to the misalignment of the loading direction and the stiff mineralized collagen fibers. Furthermore, the introduction of weak interfaces that span the entire width of a fibrolamellar unit assists in weakening the sample more. At larger orientation angles, more load is directly applied to these weak interfaces such that the weak interfaces of fibrolamellar units at 90° orientations experience the entire axial mechanical load.

As expected, these micro-tensile measurements also demonstrate an apparent hydration effect, since the samples themselves are approximately half composed of an organic component. To estimate the effect of hydration on the elastic moduli and UTS at different orientations, dry to wet ratios of moduli and UTS are produced at 0° and 90°

orientations. These ratios $\dfrac{E_{dry,0°}}{E_{wet,0°}}, \dfrac{UTS_{dry,0°}}{UTS_{wet,0^*}}$ and $\dfrac{E_{dry,90°}}{E_{wet,90°}}, \dfrac{UTS_{dry,90°}}{UTS_{wet,90^*}}$ represent the relative

Table 4.1. Summary of micro-tensile and nanoindentation measurements on the hydration and orientation effects of fibrolamellar bone units The elastic modulus and strengths of fibrolamellar bone units are measured at different orientations as well as in dry and wet states. In NI, an indentation modulus and the respective hardness are measured at different orientations to the major bone axis.

	Elastic modulus, E [GPa] (mean ± S.E.M.)		Ultimate Tensile Strength, UTS [MPa] (mean ± S.E.M.)		Nanoindentation, NI (mean ± S.E.M.)	
Orientation	Dry	Wet	Dry	Wet	Indentation Modulus, E_{NI} [GPa]	Hardness, H [GPa]
0°	11.1 ± 2.22	7.85 ± 0.981	128 ± 13.9	75.9 ± 5.96	23.1 ± 1.32	0.678 ± 0.0741
10°	8.29 ± 0.703	4.09 ± 0.996	95.9 ± 13.1	37.8 ± 4.79		
20°	7.77 ± 0.967	1.64 ± 0.598	62.2 ± 5.35	19.9 ± 2.33		
30°	5.16 ± 2.28	1.41 ± 0.393	50.8 ± 8.48	15.7 ± 2.84	21.7 ± 1.08	0.724 ± 0.0592
45°	3.04 ± 1.17	0.905 ± 0.294	24.5 ± 5.88	8.62 ± 1.34	16.1 ± 0.457	0.567 ± 0.0288
60°	1.55 ± 0.546	0.281 ± 0.141	26.4 ± 5.66	4.95 ± 1.12	18.4 ± 0.316	0.662 ± 0.0224
90°	1.33 ± 0.425	0.257 ± 0.150	13.3 ± 5.10	3.11 ± 0.438	15.4 ± 0.522	0.502 ± 0.0327

differences between the dry and wet states of elastic moduli and UTS, resulting in values of 1.41, 1.68 and 5.17, 4.28, respectively. The differences observed in the 90° orientations reveal the dramatic effects on the elastic modulus and UTS from hydration. These relative ratios implicate these weak interfaces to be regions where hydration affects the materials properties in fibrolamellar bone.

4.1.3 Modeling the strength and elastic modulus

Furthermore, the dry and wet data obtained from the micro-tensile measurements show trends that are explained by a fiber composite model. In an attempt to fit a model to the data, the Tsai-Wu fiber composite model [9, 63]

$$\left(\frac{\sigma^2 \cos^4 \theta}{X_1^2} + \frac{\sigma^2 \sin^4 \theta}{X_2^2} + \frac{\sigma^2 \sin^2 \theta \cos^2 \theta}{X_{12}^2} - \frac{\sigma^2 \sin^2 \theta \cos^2 \theta}{X_1 X_2} \right) = 1 \qquad \textbf{(Eq. 4.1)}$$

is used to fit the strength data such that where X_1 is the strength parallel to the main collagen fiber axis, X_2 is the strength orthogonal to the collagen fiber axis, and X_{12} is the shear strength. Whereas, the elastic moduli were fit with a relationship containing four material specific constants [9]

$$\text{E}(\theta) = \frac{1}{S_{11} \cos^4 \theta + (2S_{12} + S_{66}) \cos^2 \theta \sin^2 \theta + S_{22} \sin^4 \theta} \qquad \textbf{(Eq. 4.2)}$$

such that S_{11} is the elastic compliance value in the direction of the collagen fiber axis, S_{22} is the elastic compliance value orthogonal to the fiber axis, S_{12} is the in-plane compliance, and S_{66} is the shear compliance. Of interest is the quality of the strength and elastic moduli fits used, each possessing R-values of 0.996, 0.995 and 0.996, 0.996 for dry and wet measurements, respectively. The material constants obtained from the fit parameters provide additional proof that the interfaces themselves are critical in providing the specific materials properties in fibrolamellar units (**Table 4.2**). Specifically through these fit parameters, the interfaces are implicated in contributing to the increased degree of anisotropy that is observed compared to previous examples found in literature where the value of v_{xy} is approximately 0.3 [44, 45] while this data indicates a v_{xy} value

approximately 0.12. This extreme anisotropy is a result of isolating the individual fibrolamellar units with the innate microstructural features intact, whereas previous works have obtained a value for the bulk material typically through indentation techniques and uniaxial measurements on whole tissue [7, 8, 102, 109, 110].

In comparison to the NI data, the micro-tensile measurements show a steeper decline as the measurements move further away from the main bone axis. These differences, indicate two possible scenarios which explain these differences: (1.) individual fibrolamellar units, while intact in fibrolamellar bone tissue, interact with other fibrolamellar units to distribute the load and when an individual fibrolamellar unit is isolated, such a load distribution mechanism does not occur. In a quick comparison to the NI indentation modulus at 0°, the elastic modulus obtained by micro-tensile measurement is $\sim \frac{1}{2}$ of the modulus obtained by NI, validating an effect of the surrounding bone tissue on the NI measurements. (2.) The fibrolamellar interfaces are not activated in the bulk NI measures, probably due to the aforementioned reason in (1.), except in the case of 45° where shear forces are at their maximum. In both explanations, the source of the lower elastic modulus and strength in the micro-tensile measurement is due to a weak, organic interface. To validate that the precipitous drop in **Figure 4.2(C.)** in the tensile case is indeed related to the presence of these interfaces, micro-tensile measurements on the same fibrolamellar units in the same orientations are performed in a hydrated environment. When the mechanical behavior of the fibrolamellar units are in fact dictated by these interfaces, the same mechanical properties should be even lower when hydrated due to the sensitivity to hydration of the organic component [92] [111]. Indeed, as observed in **Figure 4.2** in the tensile measurements performed in a wet environment, a similar trend as observed in the dry case when progressing from 0° to 90° in both elastic modulus and strength are seen. The wet case is lower, in fact in elastic modulus the ratio of dry-to-wet is approximately ~30% larger and in strength the ratio is approximately three-fold larger. This supports the claim that the interfaces determine the mechanical behavior of fibrolamellar bone tissue. In essence, the role of these weak interfaces in a constantly loaded material like bone is to dissipate excess high loads away from load sensitive constituents.

Table 4.2. Fit parameters of measured elastic moduli and UTS values from dry and wet samples (The errors are determined from variations in the measured values) Utilizing Eqs. 4.1 and 4.2, the following fit parameters, corresponding to constants that describe the materials constants in a transverse orthotropic material, are fitted from measured values where X_1 is the strength parallel to the bone axis, X_2 is the strength orthogonal to the bone axis, X_{12} is the shear strength, S_{11} is the elastic complicance parallel to the direction of the bone axis, S_{22} is the elastic compliance orthogonal to the bone axis, S_{12} is the in-plane compliance, and S_{66} is the shear compliance

	Dry Samples	Wet Samples	Ratio (Dry to Wet)
Strength Parameters [MPa]			
X_1	127.0 ± 5.1	75.9 ± 1.7	1.67 ± 0.077
$\left(\dfrac{1}{X_{12}^{\,2}} - \dfrac{1}{X_1 X_2} \right)^{-\frac{1}{2}}$	25.8 ± 2.6	7.8 ± 0.5	3.3 ± 0.036
X_{12}	22.7 ± 1.8	7.23 ± 0.41	3.14 ± 0.11
X_2	17.9 ± 2.8	4.9 ± 0.8	3.7 ± 0.83
$\dfrac{X_1}{X_2}$	7.09 ± 1.15	15.5 ± 2.6	
Elastic Moduli Parameters [GPa]			
S_{11}^{-1}	10.4 ± 0.626	7.83 ± 0.286	1.33 ± 0.094
$(2\,S_{12} + S_{66})^{-1}$	2.01 ± 0.501	0.248 ± 0.030	8.10 ± 2.2
S_{22}^{-1}	1.30 ± 0.406	0.398 ± 0.209	3.27 ± 2.0
$\dfrac{S_{11}^{-1}}{S_{22}^{-1}}$	8.0 ± 2.5	19.67 ± 10.4	

As shown in the aforementioned data, there exists an unreported extreme degree of anisotropy at the micro-scale of fibrolamellar bone. With the introduction of heterogeneous, weak interfaces between stiff fibrolamellar bone units, the degree of mechanical anisotropy is controlled (**Figure 4.4**). As a result of these interfaces, hydration and orientation effects become significant in the mechanical behavior. With respect to whole bone mechanical behavior, these weak interfaces serve to inhibit as well as direct [67] crack propagation by increasing the toughness in bone tissue, a strategy shared in fiber composite materials [63]. The existence of heterogenous structures at the weak interfaces between fibrolamellar units at the meso-scale is crucial for the mechanical anisotropy of bone at the 10-100 μm length-scale (**Figure 4.4**).

4.1.4 Mechanical properties of lamellar and woven bone regions in fibrolamellar bone

The fibrolamellar bone unit is composed of woven and lamellar bone types at the 10-100 μm length-scale (see **Figure 4.5**) [3]. The contributions of each component to the overall mechanical properties of the fibrolamellar unit is not completely known. By introducing specific structural defects in the form of notches into one of these components and characterize the resulting sample, the mechanical function of each individual component is assessed. In this section, to understand further the mechanical differences of the lamellar and woven regions in fibrolamellar bone, notches into the lamellar regions are introduced and appropriately characterized by micro-tensile measurements.

The lamellar components of each unit are typically located at the units' edges and span ~15-25 μm towards the middle of the fibrolamellar unit. The woven component is "sandwiched" in between the two lamellar regions (**Figure 4.5(A.)**). In the case of fibrolamellar units without lamellar constituent components, notches extending to the edges of the woven bone are made via UV laser microdissection. Typical micro-tensile experiments found the elastic moduli and strength to be 7.34 ± 1.30 GPa, 13.3 ± 0.987 MPa, respectively. The differences in elastic modulus and strength are found to be in the form of approximately 9% and 82%, respectively, decreases from non-notched samples (**Table 4.3**). These differences between elastic modulus and strength are themselves of interest since it indicates that elastic modulus is less sensitive to micro-structural defects than strength. The decrease in strength is explained by the concentration of defects in the microstructure introduced by the notches, causing these notches to be the "weak link" in the material. This is in contrast to the elastic modulus which experiences a decrease, but not as dramatic as seen in strength. The behavior of the elastic modulus is partially explained by the relatively large woven component that is still intact and unaffected by the ~15-25 μm removal of sample material. More experimental evidence is required in
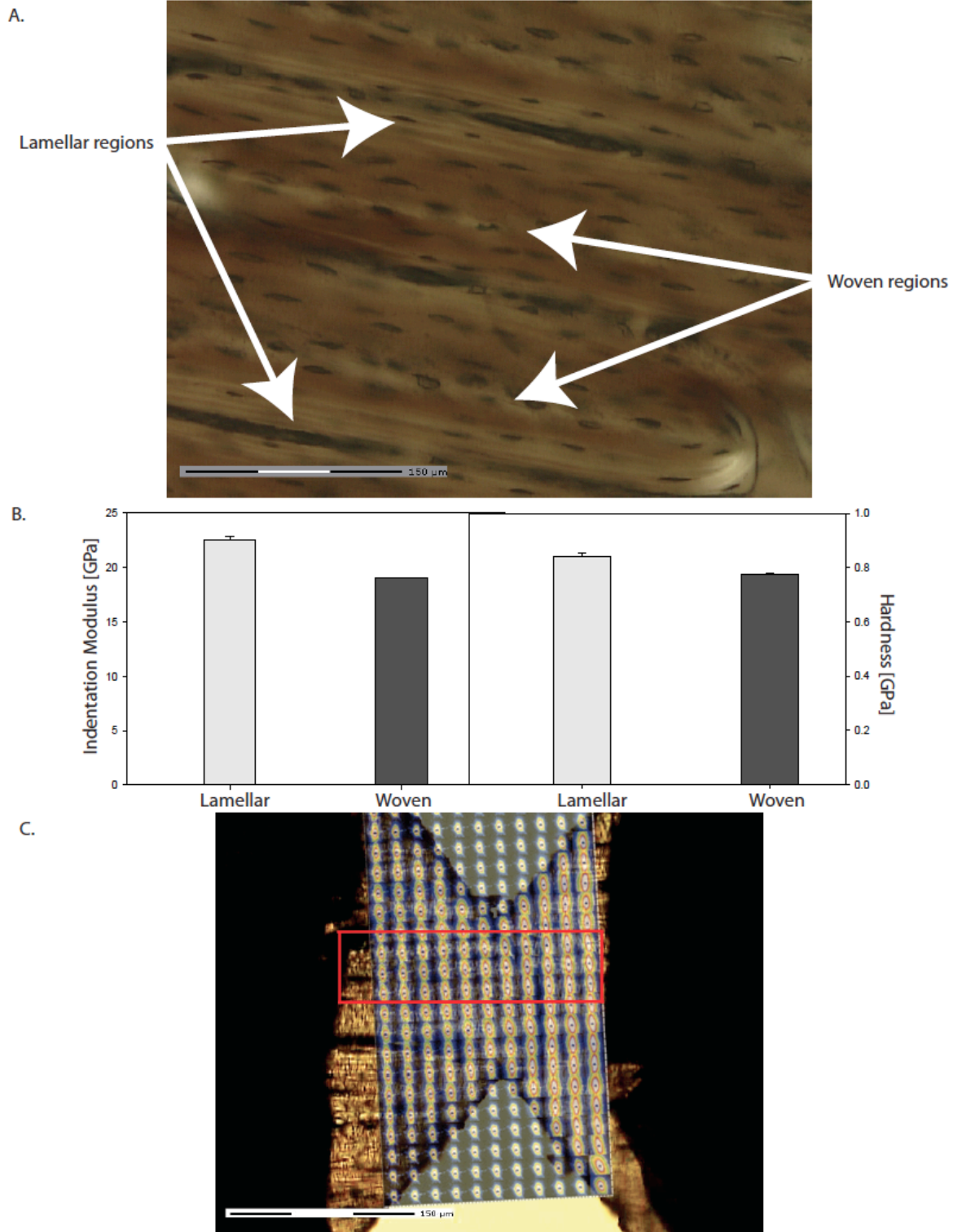
Figure 4.5 The constituent elements in fibrolamellar bone—the lamellar and woven components (**A.**) Polarized optical image of fibrolamellar bone demonstrating the presence of lamellar and woven regions (**B.**) NI of the woven and lamellar regions in fibrolamellar bone (**C.**) Scanning SAXS composite image of fibrolamellar bone with the red box highlighting the woven region in the sample.

the form of samples which have only their woven components sectioned away such that the lamellar components are characterized. Additionally, NI experiments found slight differences between the woven and lamellar bone types (**Figure 4.5(B.)**). The indentation modulus and hardness for lamellar regions are found to be 22.5 GPa ± 0.308, 0.842 GPa ± 0.0115, respectively. While the indentation modulus and hardness for woven regions are found to be 19.0 GPa ± 0.0784, 0.774 GPa ± 0.00654, respectively. These insignificant differences may indicate similarities in orientation of the mineral platelets in both woven and lamellar bone types. Although woven bone is considered to be more disorganized than lamellar bone type [9] [3], this may be the case only at short length-scales like the collagen fibril and mineral platelet scale. At the length-scale of the tissue, the organization of woven regions is similar to that found in lamellar regions. Furthermore, scanning SAXS with scan frames of 10 μm interval rasters in the woven and lamellar regions of fibrolamellar bone show no differences in orientation (**Figure 4.5(C.)**).

It is well known that the degree of mineralization in woven bone regions is noticeably greater in comparison to lamellar bone regions [3, 112]. Even with this greater amount of mineral, the hardness values obtained for woven and lamellar regions are not significantly different. Some speculative ideas on this discrepancy involve the need for mechanical homogeneity and compliance in fibrolamellar bone. In order for the fibrolamellar bone unit to attain its present mechanical properties, its lamellar and woven constituents may not be too mechanically different to reduce the possibility of large interfacial stresses that erupt from putting two mechanically incompatible materials together. By modulating the density of woven bone regions, the elastic modulus of the tissue is affected accordingly [113, 114], enabling woven bone regions to have both a higher degree of mineralization as well as being more compatible with lamellar bone regions. This would also explain the small effects when notches are introduced into the lamellar regions—the elastic modulus of lamellar and woven regions are identical.

4.1.5 Scaling effects in fibrolamellar bone

In this section, the materials properties of fibrolamellar bone samples of increasing size are measured and compared with the properties found in the single fibrolamellar bone unit to observe any scaling effects in materials properties. Specifically, using the fibrolamellar bone unit and its materials properties as a reference, samples that are two- and three- fold larger in size are characterized by micro-tensile measurements. Of particular interest is the effect of the weak interfaces on the materials properties of fibrolamellar bone with increasing size. At length-scales beyond 100 μm, the influence of multiple weak interfaces on samples of fibrolamellar bone is examined. Additionally, the following experiments address the effects of weak interfaces on the materials properties of the tissue at higher length-scales (**Figure 4.6**). In the same manner of preparing fibrolamellar units (**Chapter 3.2.1**), samples with two fibrolamellar units (one interface) as well three fibrolamellar units (two interfaces) are sectioned and characterized mechanically via micro-tensile measurements (**Figure 4.6**). It is found that elastic moduli increase with the increasing dimensions of the sample. Measurements of the elastic modulus from the single fibrolamellar unit to the double fibrolamellar unit and to the triple fibrolamellar unit samples show a progression of 7.83 to 11.99 to 22.86 GPa, respectively. The increases in elastic moduli represent, from single to double fibrolamellar units, an increase of elastic modulus by 1.5 fold, whereas from double to triple fibrolamellar units, an increase of elastic modulus by 1.9 fold is observed. The strengths of the single, double, and triple fibrolamellar units are found to be 75.9 MPa ± 1.70, 39.7 MPa ± 3.60, 58.5 MPa ± 5.21, with no clear effect observed (**Table 4.3 and Figure 4.6)**.

Using similar measurements of samples in the same dimensions, but sectioned in the orthogonal direction, a similar trend in elastic modulus is observed, whereas virtually no differences is shown in their respective UTS. The strength of the single, double, and triple fibrolamellar units are found to be 75.9 MPa ± 1.70, 39.7 MPa ± 3.60, 58.5 MPa ± 5.21. In the orthogonal orientation, elastic modulus of single, double, and triple fibrolamellar unit samples are found to be 0.398 GPa, 2.79 GPa, and 3.15 GPa,
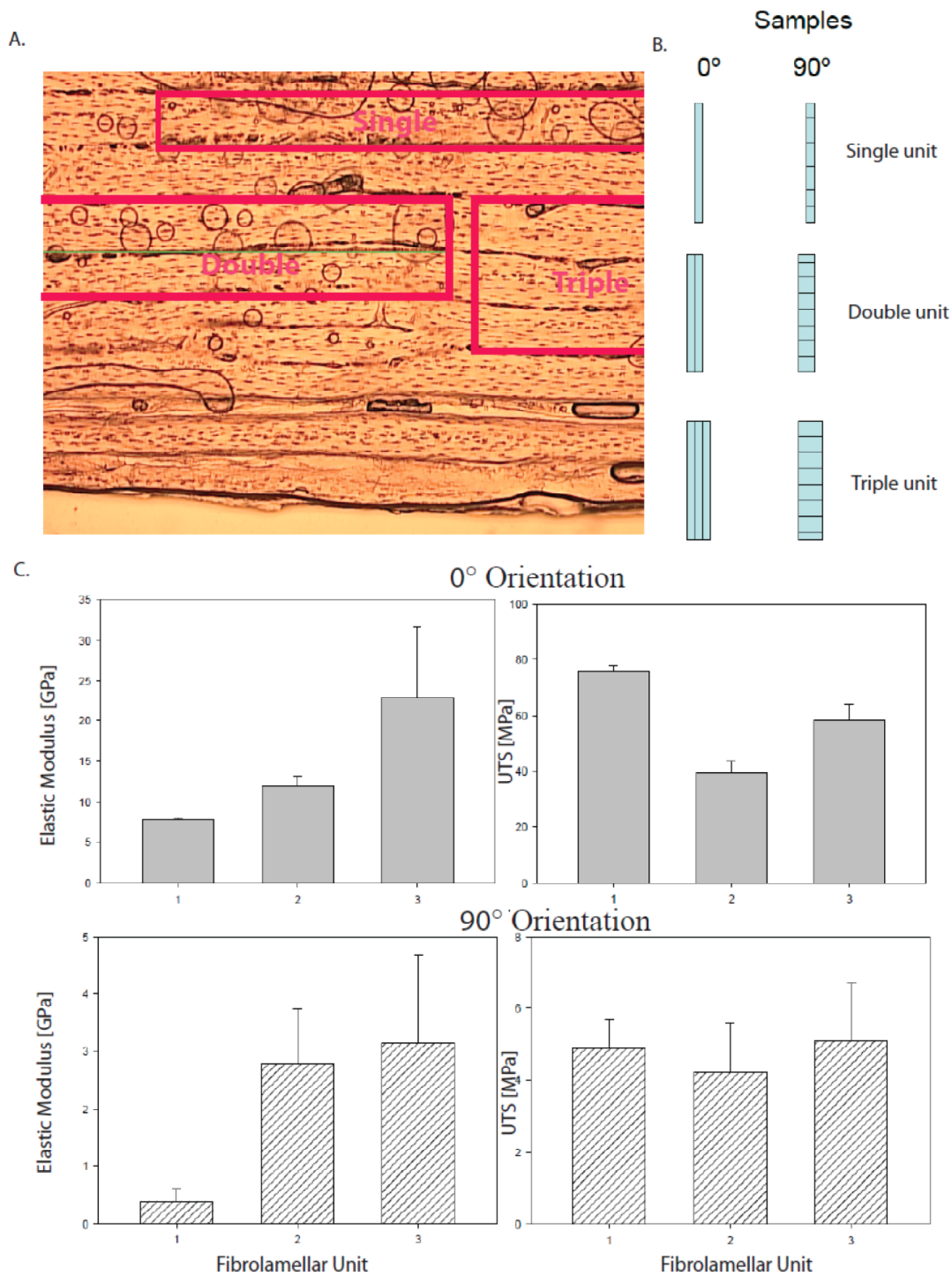
Figure 4.6 Scaling effects within fibrolamellar bone. (**A.**) An optical micrograph of fibrolamellar bone with schematic diagrams showing single, double, and triple fibrolamellar units (**B.**) A schematic diagram of the fibrolamellar units in longitudinal and orthogonal orientations (**C.**) Micro-tensile measurements of the single, double, and triple fibrolamellar units in longitudinal and orthogonal orientations.

Table 4.3. The effect of scaling sample dimension at different orientations in fibrolamellar bone By taking samples in the dimension of a single, double, and triple fibrolamellar bone unit, micro-tensile measurements the effect of dimension and orientation on the elastic modulus and strength. The errors are determined from variations in the measured values.

	E [GPa]		UTS [MPa]		Ratio (0° to 90°)		Poisson's ratio
Samples	0°	90°	0°	90°	E [GPa]	UTS [MPa]	ν_{xy}
Single Fibrolamellar Unit*	7.83 ± 0.982	0.257 ± 0.150	75.9 ± 5.96	4.90 ± 0.800	19.67	15.5	0.12
Double Fibrolamellar Unit	11.99 ± 1.25	2.79 ± 0.938	39.7 ± 3.61	4.21 ± 1.40	4.30	9.43	0.26
Triple Fibrolamellar Unit	22.86 ± 8.81	3.15 ± 1.54	58.5 ± 5.21	5.12 ± 1.58	7.26	11.43	0.53

respectively (**Figure 4.6(C.)**, **Table 4.2**). With respect to the 0° orientation, the relative increases as a result of orientation are represented by $\dfrac{E_{0°,\sin gle}}{E_{90°,\sin gle}} \approx 30.5$, $\dfrac{E_{0°,double}}{E_{90°,double}} \approx 4.30$, and $\dfrac{E_{0°,triple}}{E_{90°,triple}} \approx 7.26$. This suggests that with increasing fibrolamellar sample size, the anisotropy in the elastic moduli decreases. The Poisson's ratio, $\nu_{xy,}$, found for single, double, and triple fibrolamellar unit samples are found to be 0.12, 0.26, and 0.53, respectively. The increasing trend of the Poisson's ratio with increasing sample size indicates bone tissue is mechanically less sensitive to orientation effects at higher length-scales.

The mechanical implications of these results in fibrolamellar bone indicate that mechanical anisotropy is born from the structural anisotropy at the lower length-scales in bone—originating from the anisotropy of the aligned mineral platelets and collagen fibers at the nano-scale. At the micro-scale, weak, organic interfaces between fibrolamellar units further reinforce this mechanical anisotropy. The effect of these structures is evident at the 10-100 μm length-scale, but by increasing the sample size to higher length-

scales, a specific size threshold is reached whereby the influence of these structures is diminished. This is observed in the relative ratios of elastic moduli at 0° and 90°, $\frac{E_{0°}}{E_{90°}}$, as well as the Poisson's ratio of fibrolamellar samples with triple fibrolamellar units, with both quantities indicating a reduction in mechanical anisotropy. This is possibly mediated by compliant structures at these higher length-scales like epithelial tissues which are more relevant at these length-scales.

Furthermore, it is interesting that these size effects only affect the property of elastic modulus, with strength being virtually unchanged. This implies that the same structures defining strength at the single fibrolamellar unit also dictates strength at higher length-scales. This is especially true in the orthogonal case where the strength of the single, double, and triple fibrolamellar units are not significantly different (**Table 4.3**). The increase in sample size does not contribute to a significant change in strength in the orthogonal orientation, indicating that the effects of weak interfaces scale with the increasing sample size. In the parallel orientation, with the exception of the single fibrolamellar unit, an increase in strength is observed between the double and triple fibrolamellar unit samples. The nonconforming strength behavior of the single fibrolamellar unit is attributed to the lack of weak interfaces in the sample. No clear trend is observed in strength with increasing size.

This data suggests elastic modulus scales with increasing sample size, whereas the strength behavior with increasing sample size in the longitudinal or transverse orientations, is complicated and far from conclusive, requiring more research to understand these effects. It is clear that these weak interfaces observed at the 10-100 μm length-scale become less relevant in mechanical loading of the material bone at the tissue scale.

4.1.6 Deformation mechanisms in fibrolamellar bone

In this section, fibrolamellar bone unit samples are characterized mechanically by micro-tensile measurements and simultaneously, exposed to X-ray radiation to probe the behavior of structures at the nano-scale. By performing both micro-tensile measurements

and X-ray scattering and diffraction measurements, the mechanical load transfer is tracked from the macro- down to the nano- length-scale in the material bone.

To access the nano-scale constituents in fibrolamellar bone, X-ray diffraction techniques are utilized to probe the mineral and indirectly, the organic matrix. These techniques provide information about the material at the nano-scale such as the average size of mineral crystallites, orientation of crystallites in the material, the packing of the crystallites, and the relationship with the collagen fibers that constitute the organic matrix. With the additional ability to probe the micro-scale, the deformation of the material at both the micro- and nano- scales is quantitatively measured and described simultaneously (**Figure 4.7**). The amount of strain transferred from the tissue-level to the nano-scale constituents is determined by measuring the amount of displacement occurring in the mineral crystals as well as the collagen fibril when a fibrolamellar unit is tensed until failure [97]. Specifically, by simultaneously examining the peak shifts of the (002) lattice plane of the mineral component in WAXD patterns and the meridonal peak shifts from the SAXS patterns during tension, strains at the mineral platelet and collagen fiber length-scales can be measured [115].

By measuring the displacement at the levels of the mineral crystals, the collagen fibrils, and at the fibrolamellar unit, the amount of strain transfer from the tissue to the mineral platelet is calculated. When comparing the ratios obtained of mineral/fibril strain to fibril/tissue strain, the transfer of strain is approximately half of the value going from higher to lower length-scales. In essence, strain sensitive elements are buffered from excess strain to prevent catastrophic failure. The different interfaces between mineral-fibril and fibril-tissue levels reduce the amount of strain that is transferred to the different structures, specifically limiting certain hierarchical levels from high strains/stresses. Additionally, strain differences of measurements in dry and wet conditions of fibrolamellar units can also be examined in X-ray scattering and diffraction experiments. Interestingly, comparing the ratio of dry-to-wet in mineral/fibril strain measurements, a significant difference exists on the order of 1.55 ± 0.45 indicating that the mineral-collagen fibril interface is highly modulated by the hydration of organic components. In the dry state, the transfer of strain from higher levels of hierarchy is not buffered as much as in the physiologically wet environment, enabling transfer of more strain to the mineral
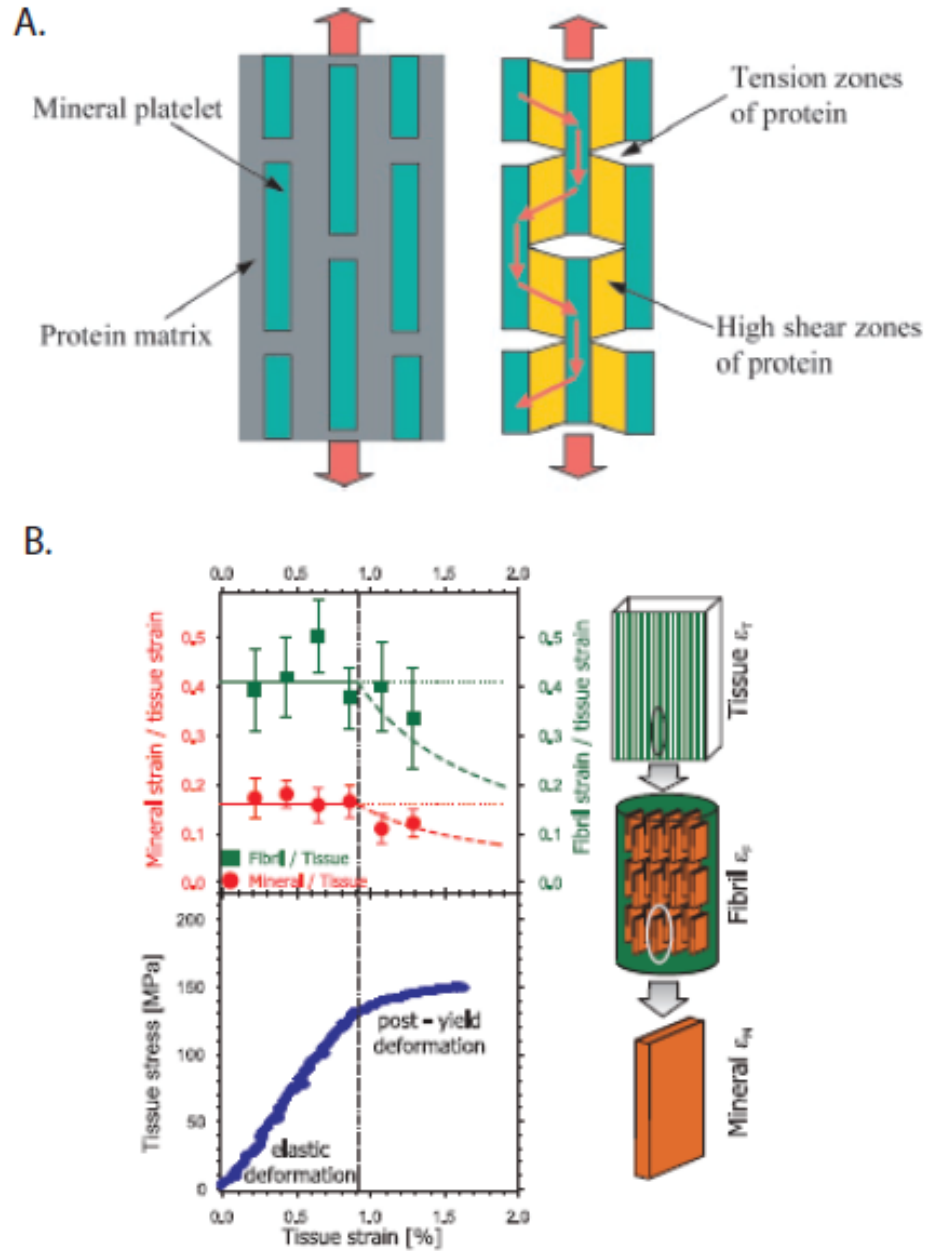
Figure 4.7 Strain transfer from the tissue to mineral platelets (**A.**) Schematic drawing of the possible mechanism of load transfer in the staggered model by way of shear in bone at the nano-scale   (**B.**) By simultaneously measuring strains at the mineral (WAXD), fibril (SAXS), and tissue (optical) during the entire measurement, strain distributions at all levels of structure is deduced [(**A.**) from Gao et al. PNAS 2000, (**B.**) from Gupta et al. PNAS 2006].

platelet. This differs to the case at the fibril-tissue levels, where the ratio of dry/wet in fibril/tissue strain is ~1. This may seem odd due to the previous arguments that interfaces

Table 4.4. **Strains in bone tissue** At the different length-scales in bone—from the tissue to mineral platelet the strains found in both wet and dry conditions reveal an increasing take up of strain at larger length-scales. Shown are εF/ εT, εM/ εT, and εM/ εF calculated from linear regressions of binned data for wet and dry samples.

Parameter	Wet samples	Dry samples
Fibril to tissue strain (εF/ εT)	0.41 ± 0.06	0.41 ± 0.02
Mineral to tissue strain (εM/ εT)	0.16 ± 0.01	0.24 ± 0.02
Mineral to fibril strain (εM/ εF)	0.34 ± 0.15	0.53 ± 0.00
Elastic modulus (ET)	11.5 ± 3.7	13.9 ± 3.4
Stress concentration (κ)	1.46 ± 0.15	1.58 ± 0.14

made of organic components contribute dramatically to the mechanical properties, specifically to the transfer of strain. A possible explanation to the 1:1 ratio in both wet and dry fibril strains is that the absolute increases in fibril and tissue strains when going from wet to dry conditions are proportional, such that the relative increases in the dry conditions do not lead to any changes in the ratio of fibril to tissue strain. Another aspect that can explain the differing effects of hydration at the different levels of bone hierarchy is the possibility that structuring of the elements from one hierarchical level to the next is different when comparing tissue to fibril and fibril to mineral platelet. In addition to composition and amount of these hydration sensitive elements at the interfaces between hierarchical levels, the organization of these elements in the material are equally critical.

The mechanisms utilized in transferring strain from the collagen fibril to the mineral show how structure and mechanical properties are coupled at critical length-scales in bone (**Figure 4.8**). In assuming a simple arrangement of constituents (i.e. fibrils and mineral) in bone, one realizes the inadequacy in simple organization schemes of constituents at different length-scales due to the large constituent mismatch in mechanical properties. Specifically, the elastic moduli of collagen fibrils are 1 GPa compared to the mineral platelets which are 100 GPa [9] [12]. Such a mismatch in materials properties not only make the overall material vulnerable to the weaknesses inherent of the individual material constituents, but also introduces additional material flaws that are derived from vulnerabilities created at the interface of the constituents. In the case of fibril to mineral strains, the measured result in a ratio of fibril to mineral strains is 5:2 supports the hypothesis that energy dissipation occurs to reduce interfacial effects between length-
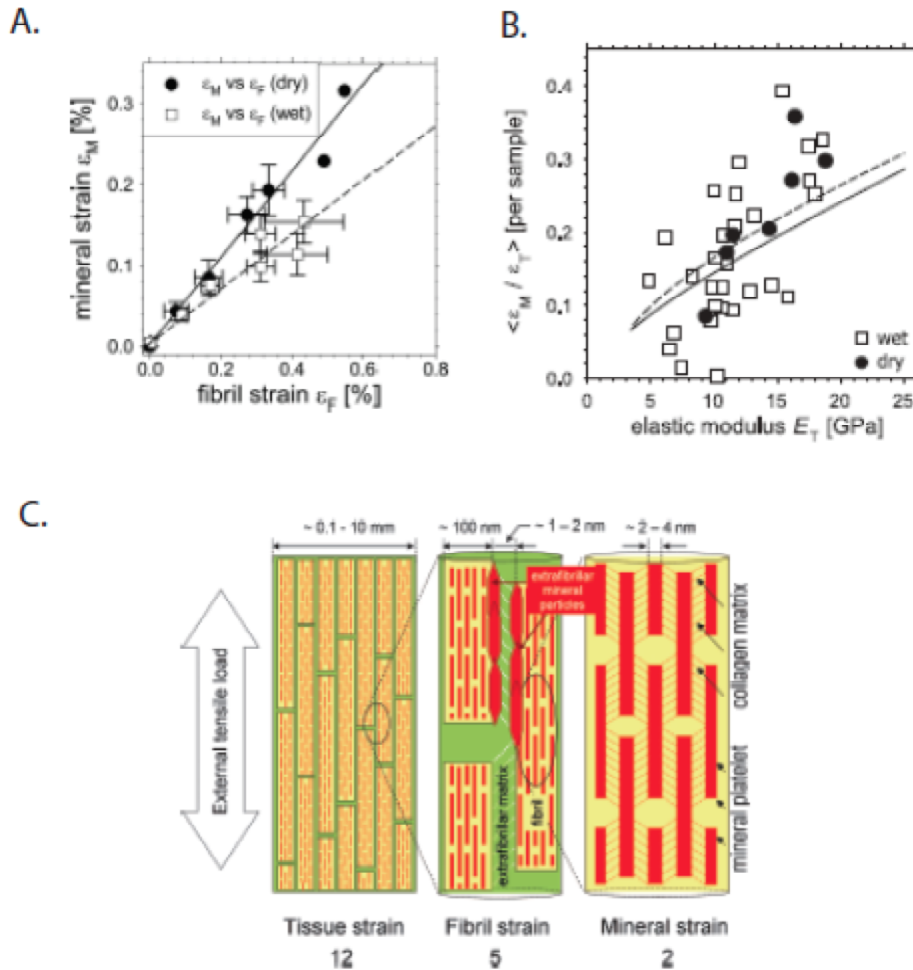
Figure 4.8 The relationship between tissue: fibril: and mineral in strain follows a ratio of 12: 5: 2 (A.) Plots of mineral versus fibril strains as well as the normalized mineral strains versus elastic modulus of the tissue show more strain and stress transfer when samples are dry compared to wet states **(B.)** A schematic drawing of the strain transfer mechanism in bone [(A.)-(C.) from Gupta et al. PNAS 2006].

scales. This energy dissipation mechanism of strain transfer is found to be similar to one based on a shear transfer and not in a parallel or Voigt model of equal strains in the collagen fibril or mineral component [48, 65]. It is found that from the tissue- to the nano – scale levels, a ratio of 12: 5: 2 is observed at the different levels of hierarchy as an individual fibrolamellar unit is tensed to failure **(Figure 4.7(B.))** [48]. In such a case where little or no reduction of strain occurs between the fibril and mineral constituents, a scheme whereby a 1:1 ratio of fibril to mineral strain occurs in bone would concentrate strain at the mineral component to the extent that catastrophic material failure takes place

at low strains. Realizing that bone does not fail at <1% strain, it is safely assumed that the 1:1 fibril to mineral strain ratio fails to explain the origin of bone's toughness. As seen in **Figure 4.8(B.)**, the mineralized fibril transfer strain to the stiff mineral platelets where there is an interconnected network of organic matrix that surrounds each platelet. During tension, the mineral platelets begin to deform by first distributing the stress between adjacent platelets through a shearing mechanism with the organic matrix.

Inelastic deformation in the material begins to occur in this case when the organic matrix no longer is able to take up excessive strain and in effect, disrupts the ability of the matrix to transfer excess strain to the adjoined mineral platelets [64]. These mineral platelets begin to accumulate defects such as cracks, and eventually, with further loading become the sites where the start of catastrophic cracking through the material begins.

Optimal organization and composition in bone are vital strategies in making a tissue that is efficiently and effectively able to repeatedly bear load and simultaneously utilize the processes of development, growth, and healing. Composition itself is important as the selection and merging together of several materials. When done randomly, disastrous materials with poor properties can appear, whereas good composite materials are formed when the material takes advantage of key features of each constituent element. This is simply described in the numerous examples of man-made composite materials [116, 117]. With the additional ability to organize the different compositions in a material, structuring at many different length-scales is possible. This enables the addition of length-scales to a material to increase surface area [32, 34] and subsequently, increase the number of interactions within or outside the material. In the context of bone, structuring in the various biological molecules takes on a more mechanical role as it allows for the ability to direct excess stress away from sensitive components [65, 66]. By structuring constituent elements in composite materials, as in the form of fiber composite materials, these same materials are tuned to have properties with increased strength and toughness ability in comparison to the non-structured analogues [116]. It is surprising that these structures in organisms have evolved and adapted to possess specific properties that aid in carrying out optimized functionality at every necessary length-scale. In the next section of this chapter, specific cases in Nature's control of bone composition and structure will be examined to the balance between composition and organization in bone.

4.2 Structure and Mechanical behavior in selected mice models

In **Chapter 4.1**, the mechanical and deformation behaviors of bovine cortical bone as well as some strategies to prevent catastrophic material failure are described. To further examine the various components and strategies that may lead to the strength and toughening processes of bone, the following pages will focus on genetic modification of key biological processes that control the development and regulation of mineralized tissues in mouse models [51, 53]. These specific details on the biological control may help in understanding how Nature is able to implement these strategies in making materials that are functionally optimized. Specifically, this work attempts to understand not only the relationship between structure and function, but also how this relationship is regulated by genes. With the vast database of disease models, transgenic mice provide an array of model systems that have specific deficiencies that is followed throughout the lifespan of the animal [118]. Many of these diseased models mimic the same diseases afflicting humans and often produce the same phenotype in humans [119]. In other instances, mice models due to the biological redundancy built-in into important processes do not show any phenotype. In the following pages, several skeletal disease models and their mechanical and structural phenotypes will be investigated to shed light on the biological control mechanisms behind bone mineralization.

Bone tissue from knockout mice models are examined by micro-tensile measurements as well as X-ray techniques. In an attempt to characterize the mechanical and structural phenotypes, comparative studies of wildtype and mutant analogs are utilized to assess the differences in materials properties between tissues. Specifically, mineralized tissue samples from Schnurri-3, Neurofibromatosis-1, and α-HS-glycoprotein mice models are examined.

4.2.1 Schnurri-3 model

The increased mineralization found in Shn3 (-/-) animals (**Chapter 2.7.1**) would adversely affect normal bone functionality. The uncontrolled mineralization, progressing with age in essence would induce an effect of osteopetrosis, making bones noticeably more stiff and dense as well as inhibiting vascularization, and possibly also affecting processes like wound healing. Although the origin of this skeletal tissue defect is biochemical, the quality of the mineral platelet formed by the abnormal osteoblastic activity is different as well. With the use of SAXS measurements, quantitative comparisons between the size of mineral particles in both the Shn3 (-/-) and Shn3 (+/+) are made. As observed from scattering patterns of Shn3 (-/-) and Shn3 (+/+) in **Figure 4.9(A.)**, analysis show very little difference in the T-parameter (Table 4.5) of the mineral platelets in the bones of the Shn3 (-/-) and Shn3 (+/+). This indicates that the dimensions of the typical mineral platelet formed by osteoblast in the Shn3 (-/-) animal is the same compared to the mineral produced in a normal animal. Furthermore, the G(X) term which is an independent quantity used for validation purposes also confirms the lack of significant differences (**Figure 4.9(B.)**). Additional measurements with FTIR and quantitative backscatter electron microscopy also indicate the amount of Ca^{2+} per mineralized area is the same, indicating that the degree of mineralization is the same and only the amount of mineral is uncontrolled in the tissue. Furthermore, the extra-mineralization poses a problem as to how the extra mineral in Shn3 (-/-) tissues is organized within the tissue. A simple scheme is to gain mineral by accretion, in a layer-by-layer scheme. This is in fact the case, but it is also found through FTIR that the

Table 4.5. T-parameter of the mineral platelet in Shn3 (-/-) and (+/+) Measurements performed under scanning SAXS describing the average thickness of the mineral platelets in Shn3 (-/-) and Shn3 (+/+) samples.

Sample	T-Parameter (mean ± S.E.M.)	η (mean ± S.E.M.)
Wildtype (6 wks)	1.87 ± 0.0578	0.0179 ± 9.31e-4
Shn3 (-/-) (6 wks)	1.80 ± 0.0888	0.0157 ± 6.44e-4
Wildtype (4 months)	1.96 ± 0.0111	0.0178 ± 6.43e-4

A.
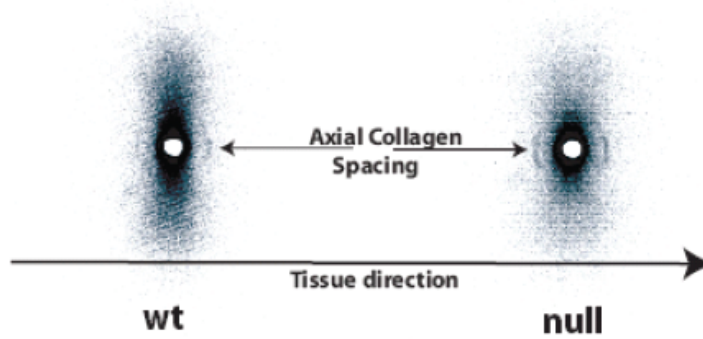
B.
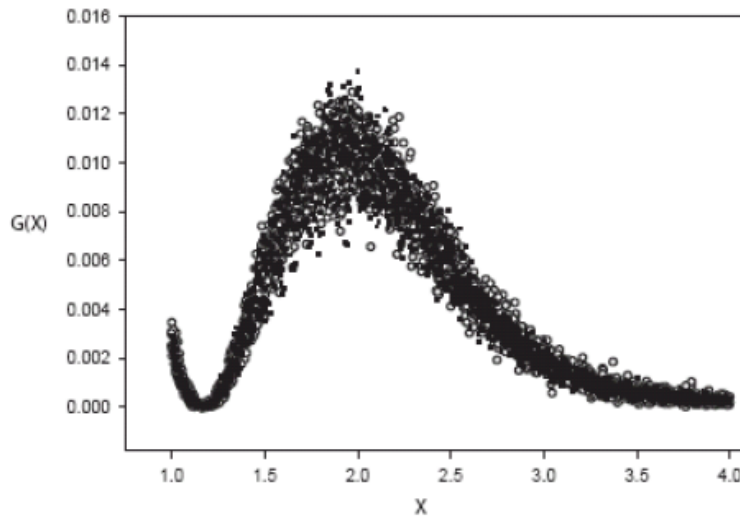
Figure 4.9 SAXS analysis of Schnurri-3 (-/-) femoral samples. (**A.**) SAXS patterns of wildtype and null Schnurri-3 mice samples (**B.**) The $G(\chi)$ function of both the wildtype and null Schnurri-3 samples showing no differences.

collagen cross-linking in Shn3 (-/-) tissue is decreased. This implicates the bone matrix as being more mineralized than the normal case. It appears that accretion of extra-mineral occurs at all surfaces, both internal and external surfaces, consistent with the fact that osteoblastic activity is confined to these surfaces as well. The study of the Shn3 (-/-) mice model indicates that Shn3 is an essential regulator of mineralization in the TGF-β signaling family and the effects of these molecular deficiencies are observed at the tissue level.

4.2.2 Neurofibromatosis-1 model

Differing from the Shn3 mice model, the neurofibromatosis (NF1) model is a mutation of a gene that expresses the neurofibromin protein (**Chapter 2.7.2**). This protein is a negative regulator in the Ras pathway of intracellular signaling and mutations of this regulator results in uncontrolled cell proliferaction and malignant transformation.

At the material level, a prominent phenotype of NF1 (-/-) skeletal tissues is the non-mineralized "holes" which are located throughout the microstructure of the tissues. As observed with X-ray radiography on a section of cortical femoral mice bone in **Figure 4.10**, areas in the bone tissue do not mineralize and are filled instead with an organic matrix (**Figure 4.11**), presumably the same organic matrix the tissue uses as an extracellular matrix for mineralization (**Chapter 2.1, 2.2**). It is not surprising that the mechanical properties of these samples are also affected (**Figure 4.13**). With a more in depth examination of the microstructure, the other "holes" in the material, the osteocytic lacunae, are also disrupted in the NF1 (-/-) animals (**Figure 4.13**, **Table 4.6**). In **Figure 4.13**, an SEM micrograph shows the morphological differences of the osteocyte lacunae between normal and NF1 (-/-) cases. In tissues with the NF1 (-/-) genotype, the osteocytic lacunae are more oblique, less uniform and in some instances, are coupled with neighboring lacunae. In addition, the mineralization around the osteocytic lacunae also appear to be less integrated with the rest of the material as "loose" clumps of mineral appear at the edges of the osteocyte lacunae. These results not only strongly implicate osteocytes as a source of the material defect in the NF1 (-/-) animals, but also indirectly show evidence of osteoctyes as active participants of the mineralization process due to the disturbances in mineralization around the lacunae.
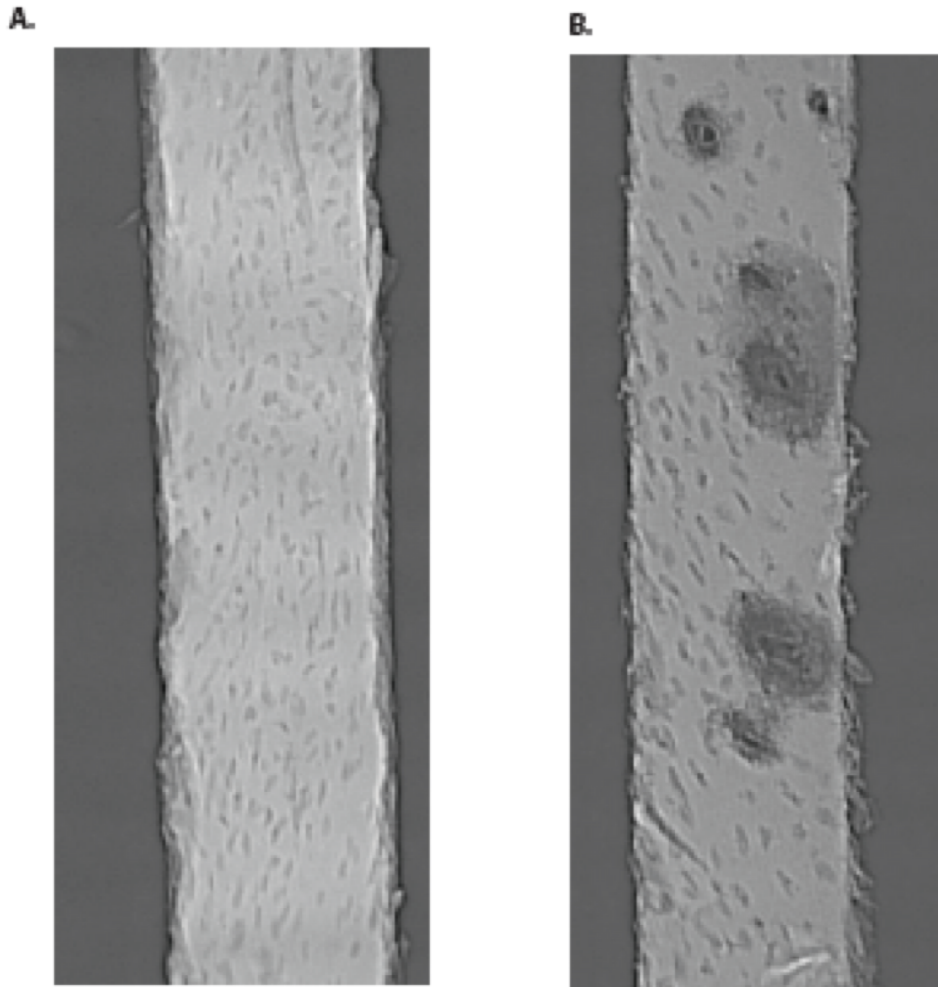
Figure 4.10 Typical samples of NF1 (+/+) and NF1 (-/-) as shown through X-ray radiography. (**A.**) X-ray radiography of a NF1 (+/+) mice sample shows normal patternining from osteocytes, typically oriented along the longitudinal axis of the bone (**B.**) A radiograph of a NF1 (-/-) mice sample showing symptomatic disorganization of the osteocytes as well as the random occurrence of large nonmineralized voids throughout the sample.

When comparing the occurrences of the irregular lacunae to the unmineralized macro-scale holes in the NF1 (-/-) tissues, the unmineralized holes occur less frequently and randomly throughout the tissue. No specific cues relating the macroscopic defects in the tissue to the defects at the osteocytic lacunae are found. It may very well be that the defects are independent where the disrupted lacunae do not contribute to the cause of the macroscopic tissue defects. It is very likely that both these voids as well as the disruption of osteocytic activity are results of a common defect. One possibility is that in NF1 (-/-)
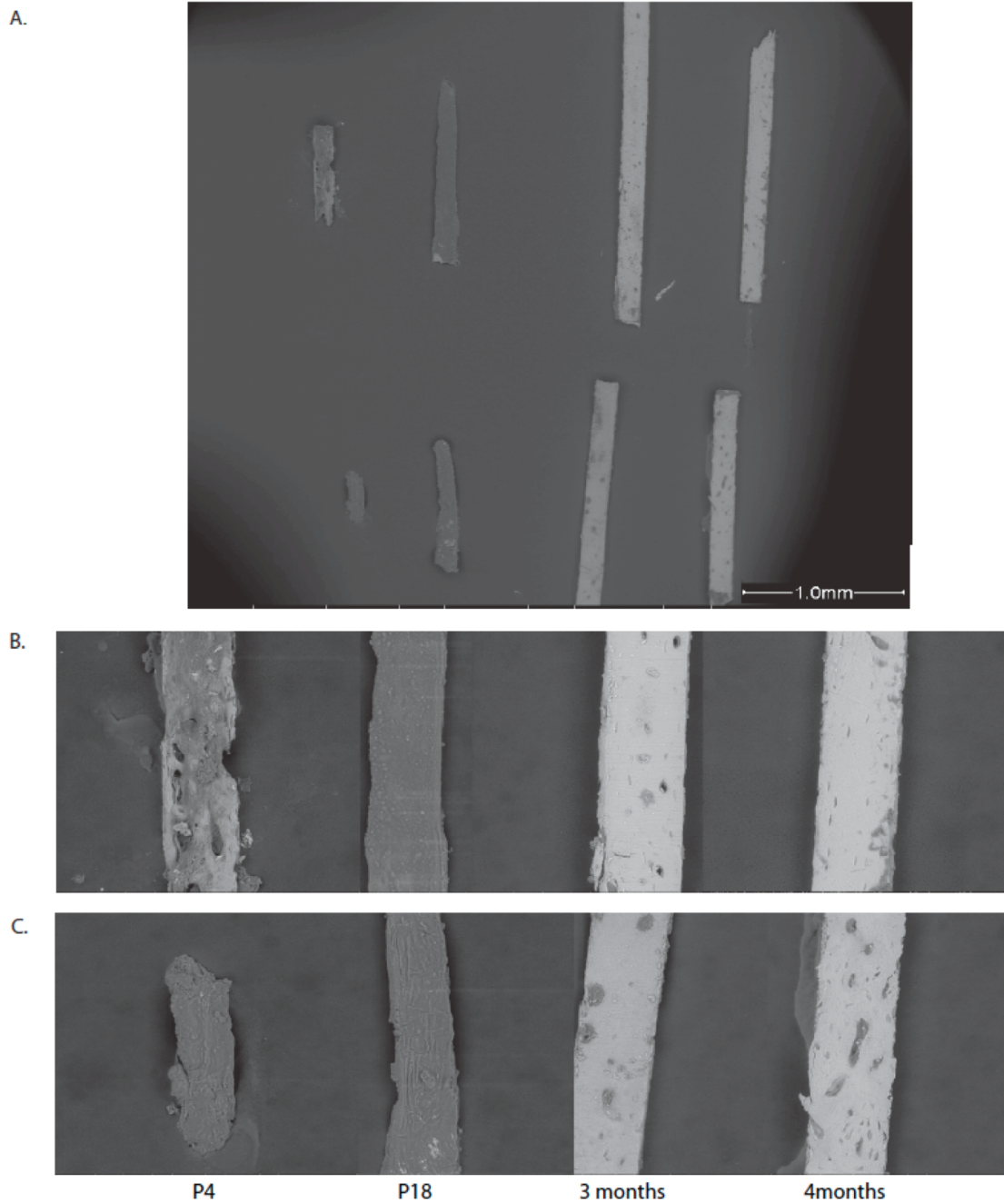
Figure 4.11 An backscatter electron density profile of NF1 (+/+) and NF1 (-/-) samples at P4, P18, 3 months, 4 months (A.) An overview of the NF1 samples measured under backscatter electron microscopy (B.) A NF1 (+/+) showing the differences in mineralization from P4 to 4M of age (C.) A NF1 (-/-) showing a similar trend as in the NF1 (+/+) case, but with more reduced mineralization in the early stages of development.
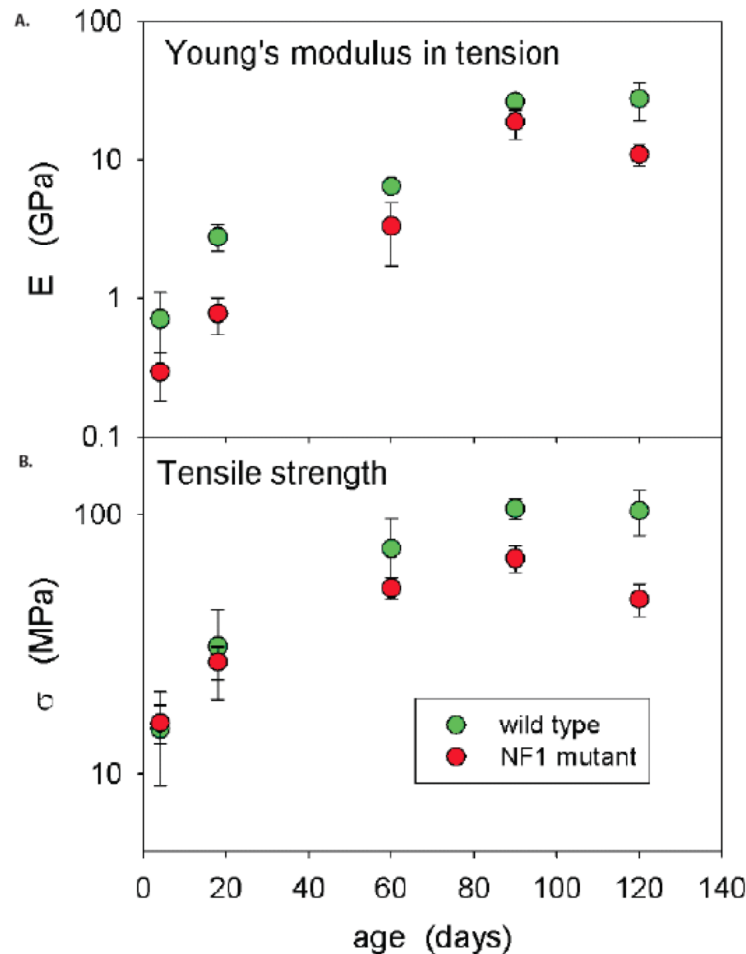
Figure 4.12 Micro-mechanical measurements (tensile) performed on NF1 (-/-) and NF1 +/- at ages P4, P18, 2 months, 3 months, 4 months. (A.) The elastic moduli of the NF1 (+/+) and NF1 (-/-) samples shows a dramatic differences at early stages, but these differences become smaller with increasing age (B.) Strength of NF1 (+/+) and NF1 (-/-) displays a divergence in the later stages of its bone development, possibly due to the defects endowed by the non-mineralized voids in the NF1 (-/-) samples.

tissues, the proper construction of the extracellular bone matrix is disrupted, manifesting itself in both defects in cellular activity as well as mineralization of the tissue.

By way of micro-tensile measurements, the mechanical behavior of NF1 (-/-) bones is found to be compromised at all ages from P4 until 4 months (**Figure 4.12**). Both elastic modulus and ultimate tensile strength are reduced in the NF1 (-/-) samples compared to NF1 (+/+) analogues. The elastic moduli of normal and NF1 (-/-) tibial sections show significant differences (P < 0.001) with the NF1 (-/-) samples being always less stiff and weaker compared to the normal case (**Figure 4.12(A.)**). On average, the normal wildtype sample is about twice stiffer and 1.5- fold stronger than NF1 (-/-)
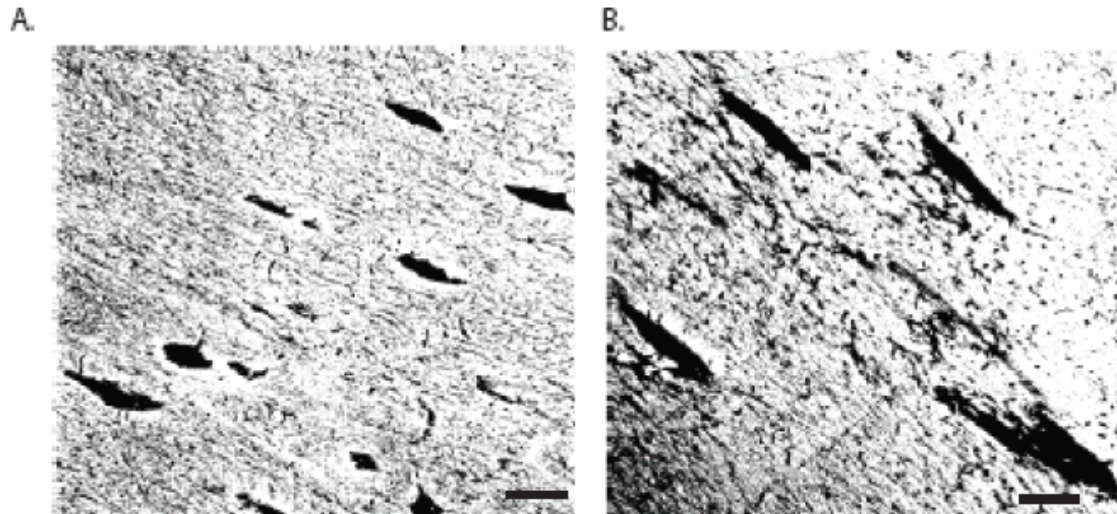
Figure 4.13 Microstructure of bone from NF1(-/-) and NF1 (+/+) mice (**A.**) Scanning electron micrograph of a typical NF1 (+/+) sample and its osteocytes (**B.**) Similar measurement of a NF1 (-/-) sample and its osteocytes, displaying a disorganization as well as a defect in its morphology (scale bar = 10 μm).

analogs. At a closer glance, the elastic modulus of the normal case increases with increasing age. This effect with age is not surprising since the main contributing component affecting the elastic moduli is the organic component, mainly the collagen fibers. With increasing age, the collagen orientation becomes more aligned and inter-fibrillar cross-linking becomes abundant and common [39] [38].

In addition, the degree of mineralization also increases with age acting in a similar effect on the elastic modulus as collagen cross-linking. Specifically, in the wildtype the rate of increase in elastic moduli is most notable between the ages P4 and 3 months, characterized by a pattern of rapid increase interrupted by a slower increase and again a return to a rapid increase. In contrast, the NF1 (-/-) analogs show slow gradual increases that become more rapid with age. Even with these rapid increases in elastic moduli at later ages, the NF1 (-/-) samples never fully recover the same elastic properties as in the wildtype. These notable differences are observed by taking ratios of $E_{wildtype}/E_{NF1}$ at all ages. No notable trends are observed from the ratios which range from 2.4 at P4 to 3.6 at P14 to 1.4 at 3 months (**Table 4.6**). In the NF1 (-/-) samples, the development of the elastic properties is interrupted such that there is an absence of processes responsible for the rapid stiffening of the extracellular matrix at the proper ages. Instead, as observed in

the aforementioned results, the NF1 (-/-) samples undergo a slowed and delayed maturation process of its extracellular matrix, never attaining the same elastic properties as its normal counterpart. The poor quality of mineralization in the tissue is observed to be a result of a disruption in the extracellular matrix.

In continuing the analysis on the micro-tensile data, the ultimate tensile strength is extracted to provide data on fracture strength. Of interest is the correlation between strength and age of the animals. From P4 until 2 months, it is well known that mineralization increases with age in mice [120] [121] [105] [9]. The strengths at these time points also correlate to an increase in strength (**Figure 4.12(B.)**). Indeed, it has been shown that an increase of normal mineralization (non-pathological) does increase the strength of the tissue [76]. The rate of increase in the normal animal is substantial. From ages P4 to P14, the strength doubles. This similar result also occurs for tissue compared at age points P14 and 2 months old. However, from 2 months to 3 months strength increases notably less, to about 1.4 fold, and the differences between 3 and 4 months, the difference in strength is minimal (**Table 4.6**). The initial rapid increases in strength indicate a flood of mineralization activity occurring directly after birth and continues to approximately 2 months, whereby the degree of mineralization markedly decreases. This decrease does not mean an absolute halt in the mineralization processes. In fact, this is known not to be the case as mice continue to mineralize throughout their entire lives unlike humans. This sole fact makes obtaining suitable mice models of osteoporesis problematic [122]. The relative decrease in mineralization compared to the postnatal stages is due to the remodeling processes that occur at later stages in the lives of the animals. Mineralization processes probably do slow down, but are more significantly counter-balanced by osteoclastic activity which appears to negate the effects of mineralization on the UTS. In comparison, the NF1 (-/-) analogs also follow the same trends in strength with increasing age. Like in wildtype animals, an increase in strength is observed such that the NF1 (-/-) samples increase in strength by about 1.72 from P4 to P14 and 1.92 from P14 to 2 months. Similarly, the strength of the NF1 (-/-) from 2 to 3 months also begins to decrease in a manner described in the wildtype animals. At 3 to 4 months, a decrease of mineralization on the order of 70% occurs. Albeit, the magnitude of the strength increases in NF1 (-/-) are not as large compared to that in the wildtype

case, the differences between the ages do follow trends observed in the wildtype mice. The differences are themselves attributed to the defects in the material, the unmineralized holes as well as the microscopically disorganized osteocyte lacunae. The absolute differences in the strength between NF1 (-/-) and wildtype animals are reflected by the ratio of $UTS_{control}/UTS_{NF1}$, where the ratios increase in a linear fashion with gradual increases with increasing age. The behavior of the ratios indicates that the strength, also an indicator of the degree of mineralization, is not entirely affected by the NF1 (-/-) defects. It appears that the process of mineralization is itself unaffected by the NF1 (-/-) defects. In addition, preliminary SAXS investigations into the mineral of NF1 (-/-) and normal mineralized tissues show no characteristic differences between the two types in both T- and ρ- parameters. Thus, when mineralization does occur in the NF1 (-/-) animals, it does so in a regular manner as observed in wildtype animals.

From these results, it is clearly demonstrated that in NF1 (-/-) samples, the defect is localized to the organic matrix of the tissue. The development of this matrix in NF1 (-/-) animals does not occur properly at its embryonic and prenatal stages and results in a disruption of the organic framework. Thus, disrupting the substrate used for tissue growth and development. Significantly, this disruption is observed in the form of

Table 4.6. Summary of mechanical properties of NF1 (-/-) and (+/+) bone Micro-tensile measurements of NF1 (-/-) and NF1 (+/+) samples at several ages showing increasing E and UTS with increasing age.

	E [GPa] (mean ± S.E.M.)					UTS [MPa] (mean ± S.E.M.)				
Sample	P4	P14	2M	3M	4M	P4	P14	2M	3M	4M
Normal	0.709 ± 0.400	2.78 ± 0.597	6.44 ± 0.238	26.3 ± 3.52	27.8 ± 8.26	14.9 ± 5.86	31.0 ± 11.7	74.0 ± 22.1	105 ± 10.1	103 ± 20.0
NF1 (-/-)	0.293 ± 0.111	0.775 ± 0.232	3.31 ± 1.60	18.9 ± 4.61	11.0 ± 1.96	15.7 ± 2.67	27.0 ± 3.94	51.9 ± 4.81	67.8 ± 7.75	47.2 ± 6.63

structural defects in the material at the micro- and macro- scopic length-scales. These defects manifest themselves in the form of inferior materials properties, such as elastic moduli and UTS, and subsequently, poor mechanical properties. This interruption of proper matrix development is clearly shown by the absolute differences in the elastic and ultimate tensile properties of the wildtype and NF1 (-/-) cases. It is notable that although the relative values in elastic and tensile properties in wildtype and NF1 (-/-) analogs are dramatically different, the NF1 (-/-) values follow trends observed in the wildtype case. Specifically, the elastic behavior of the NF1 (-/-) tissues do appear to be delayed developmentally, but the processes involved in the postnatal development of elastic properties occur unhindered and develop like in the wildtype case at all ages. A similar situation occurs in the case of the tensile properties, which happen to be indicative of the degree of mineralization in the tissue, whereby the UTS of NF1 (-/-) and normal animals behave in a similar trend with age. The analysis of the mechanical properties of tissues from NF1 (-/-) and normal animals explicitly suggest that the mineralization processes in NF1 (-/-) proceed normally, but the significant structural anomaly is in the organic matrix which is disrupted by defects in processes that occur during the initial organization and formation of the matrix in utero.

4.2.3 α-Heremans-Schmid glycoprotein/Fetuin-A model

α2-HS-glycoprotein is implicated in direct interactions with mineral ions in order to regulate the amount of mineral ion concentration in blood serum (**Chapter 2.7.3**). Ahsg is a major component of the bone extracellular matrix although it is not expressed by osteoblasts. In an attempt to understand the role of Ahsg in the mineralization of bone, Ahsg mutant mice models are mechanically and structurally investigated for insights of this molecule in bone. In the following pages, a comparative study between Ahsg bone samples and Ahsg deficient bone samples using mechanical measurements, backscatter electron microscopy, synchrotron X-ray scattering and in-situ micro-mechanical tensile measurements is presented.
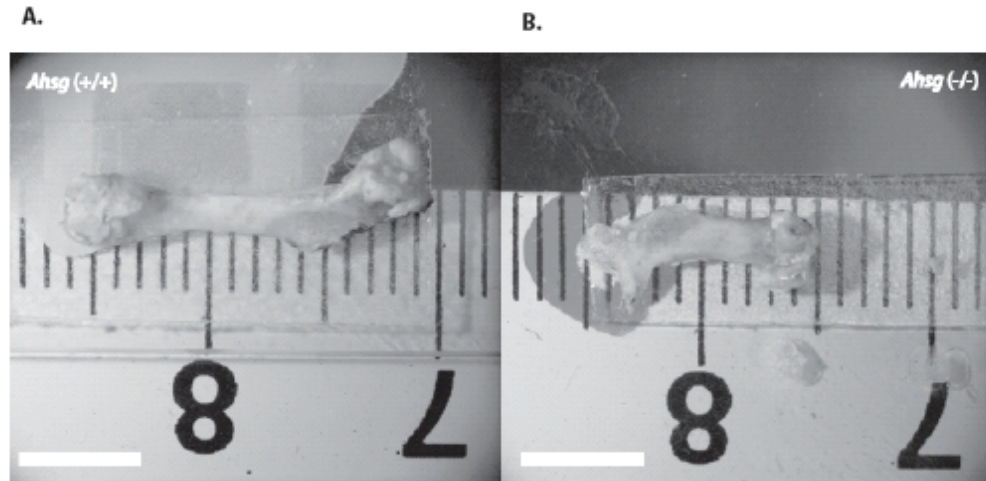
Figure 4.14 Comparison of bone tissue from Ahsg (+/+) and Ahsg (-/-) (A.) Typical femur from a Ahsg (+/+) animal where its length is ~15 mm (**B.**) The phenotype of a femur from an Ahsg (-/-) animal is evidence that the disorder is a form of dysplasia, such that its length is reduced approximately ~50%.

The differences between the *Ahsg* (-/-) and *Ahsg* (+/+) cannot be seen at the microstructure of the samples, but are apparent at the tissue level (**Figures 4.14**, **4.15**). A major phenotype is the lengths of the bone samples where *Ahsg* (-/-) samples are always shorter than those in *Ahsg* (+/+). Typical *Ahsg* (+/+) and *Ahsg* (-/-) samples observed with the scanning confocal microscope revealed no characteristic microstructural differences (**Figure 4.16(A.-D.)**). No differences were observed in either the morphology or frequency of osteocyte lacunae nor the canaliculae in both the *Ahsg* (+/+) and *Ahsg* (-/-) samples (**Figure 4.16(C.-F.)**). Moreover, no clear differences are observed in the amount of organic-inorganic components via Raman microspectroscopic techniques (**Figure 4.17**). Since the characteristic osteocyte lacunae, purported sites of microcracking and crack propagation under extreme loads [79, 123], in both sample populations appear to be equally distributed and abundant, this implies that during plastic deformation of the tissue, fracture mechanisms in both *Ahsg* (+/+) and *Ahsg* (-/-) would not be significantly different (**Figure 4.18** and **Table 4.7**).
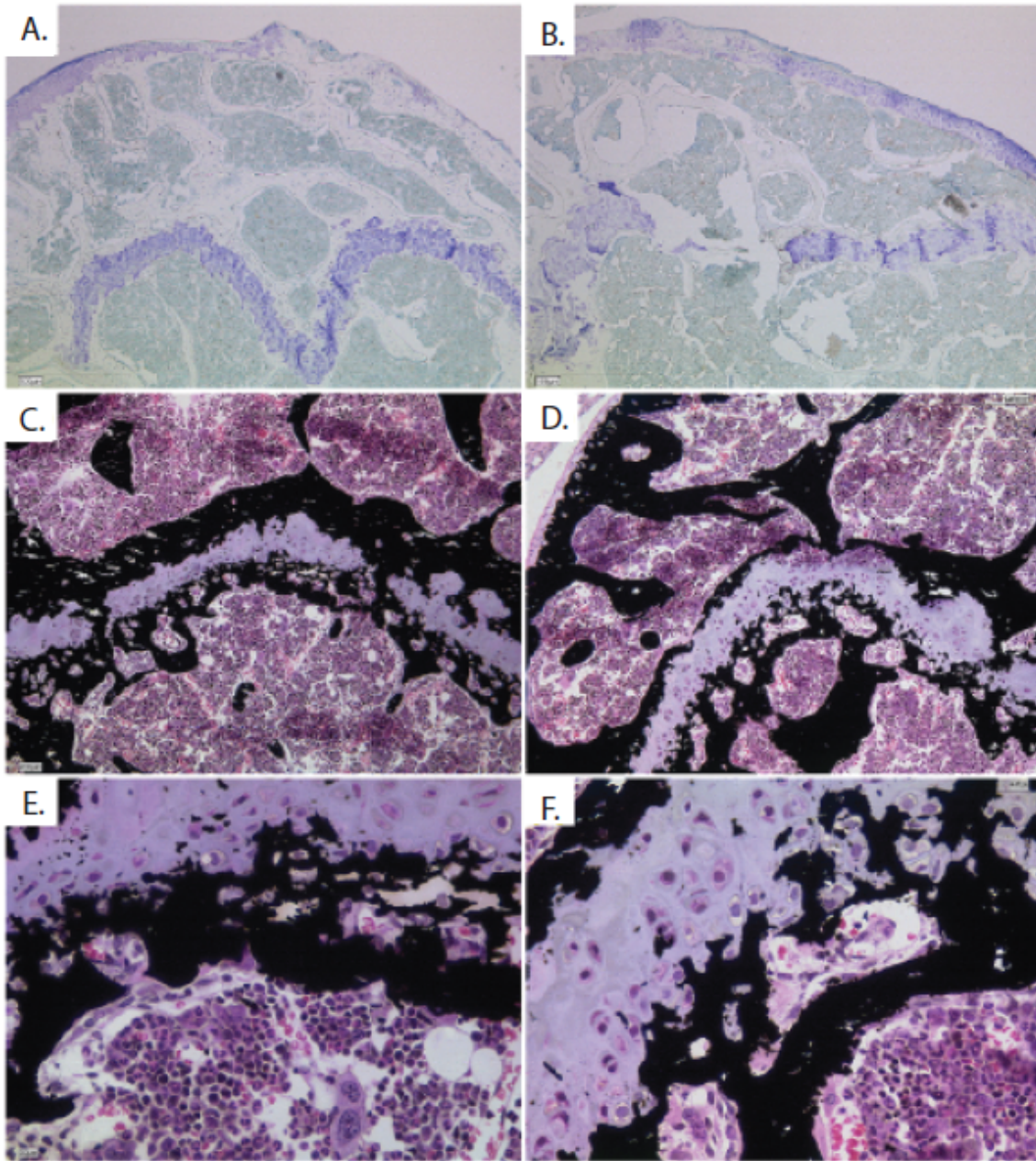
Figure 4.15 Histology of the epiphyseal growth plate in Ahsg (-/-) and Ahsg (+/+) mice (A.-B.) Sections were stained with toluidine blue to visualize the growth plate (scale bar: 500 microns) (C.-F.) Sections with safranin O for comparative staining of the growth plate (scale bar: ((**C.-D.**) 200 microns, (E.-F.)50 microns, respectively) (**B., C., E.**) Shown are growth plate discontinuities affecting secondary endochondral ossification in Ahsg (-/-) bones.
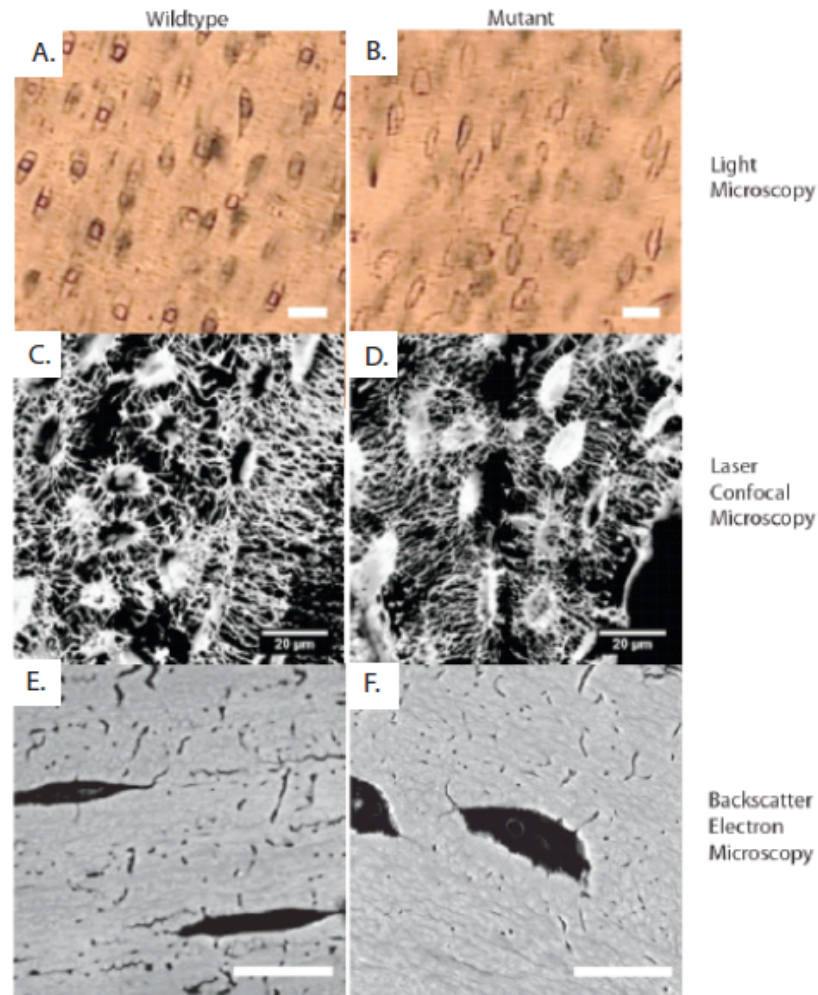
Figure 4.16 Microstructure of Ahsg (-/-) and Ahsg (+/+) cortical bone (A.-B.). Light microscopy of osteocyte lacunae in Ahsg (+/+) and Ahsg (-/-) samples, respectively (scale bar: 20 microns) (C.-D.). Laser scanning confocal microscopy using rhodamine-b as a contrasting agent showing osteocyte and canaliculi networks of Ahsg (+/+) and Ahsg (-/-) samples (light areas are intensely stained with rhodamine) (scale bar: 20 microns) (E.-F.) Backscatter scanning electron microscopy revealing the microstructure at the surface and no significant differences in density (scale bar: 10 microns).

Further complementing observations from confocal microscopy, X-ray radiography was used to examine the microstructure in the *Ahsg* (+/+) and *Ahsg* (-/-) samples. *Ahsg* (+/+) and *Ahsg* (-/-) samples did not display any differences in microstructure as well. In addition, fractured samples used in the micro-mechanical tensile measurements are examined under scanning electron microscopy to analyze the fracture surfaces. Samples
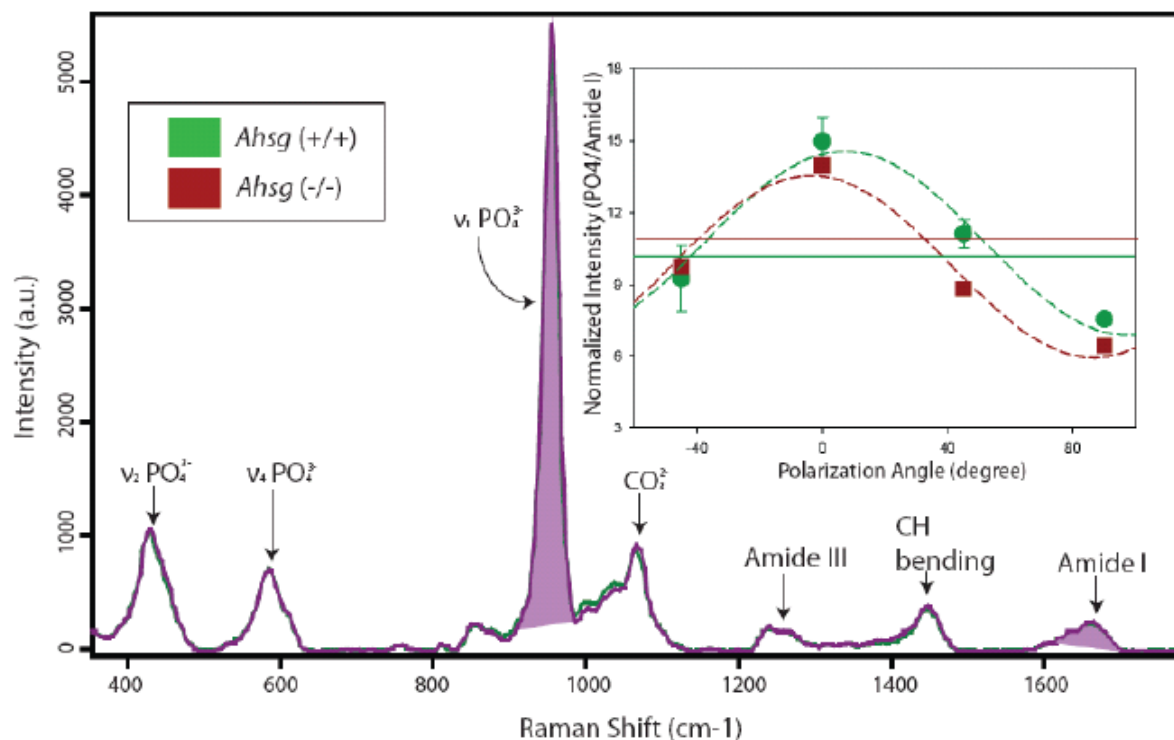
Figure 4.17 Micro-Raman spectroscopy of Ahsg (-/-) (red) and Ahsg (+/+) (green) A typical Raman spectrum of representative Ahsg (+/+) and Ahsg (-/-) samples with peaks at 910-990 cm^{-1} and 1600-1700 cm^{-1} representing PO$_4$ (mineral) and Amide I (organic matrix) groups, respectively. Inset: Normalized intensity measurements at polarization angles of -45, 0, 45, 90 were made to address the orientation artefacts of Raman intensity of type 1 collagen for both Ahsg (+/+) and Ahsg (-/-). The dashed lines are fits which estimate parameters characteristic of sample orientation and mineralization. The solid lines are mean intensity values of mineralization in the samples.
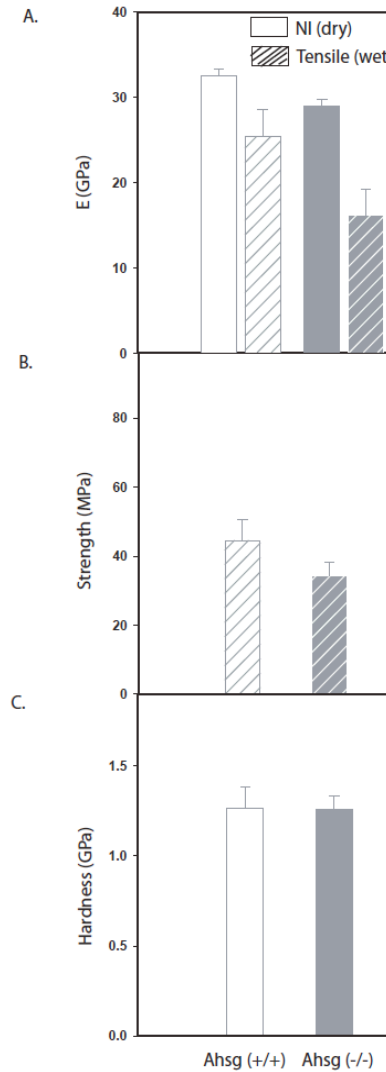
Figure 4.18 Mechanical measurements of Ahsg (-/-) and Ahsg (+/+) bone (A.). Nanoindentation (n=80) and microtensile (n=20) measurements of the elastic moduli of the wildtype and mutant samples (B.) Ultimate tensile strengths of Ahsg (+/+) and Ahsg (-/-) samples as well as (C.) hardness measurements of Ahsg (+/+) and Ahsg (-/-)

from both *Ahsg* (+/+) and *Ahsg* (-/-) showed fracture surfaces that are typical of brittle fractures (**Figure 4.19**). At higher magnifications, the collagen fiber bundles are observed in both samples and do not show any differences in orientations or structure. Furthermore, laboratory based small angle X-ray scattering was performed to analyze the dimensions of the mineral crystallites in the *Ahsg* (+/+) and *Ahsg* (-/-) samples. The T-parameter was analyzed from the scattering data to provide a value of 2.15 nm ± 0.05 for *Ahsg* (+/+) samples, whereas a value of 2.19 nm ± 0.09 was obtained for the *Ahsg* (-/-)

samples. The differences in T-parameters are not significant (P=0.061). In addition, to complement the X-ray attenuation coefficients measured by μCT, the amount of the X-ray absorbed and transmitted through the sample as measured during SAXS measurements provides information on the absorption of the sample which correlate to the amount of mineral in the sample. In comparing the transmission profiles normalized to the background profile, it was found that no significant differences exist between the *Ahsg* (+/+) and *Ahsg* (-/-) samples (**Table 4.8**). The lack of structural differences between *Ahsg* (+/+) and *Ahsg* (-/-) tissues, although *Ahsg* is indeed found in cortical bone [62], indicates that the effect of *Ahsg* on the mineralization process may be reduced in 12 month old femoral cortices. This may be attributed to several possible reasons, such as the presence of nucleation sites in bone tissue which override the effect of fetuin or the blockage of fetuin from actual nucleation events in bone tissue. Similar NCPs in bone such as osteopontin and osteocalcin do undergo enzymatic digestion and in effect, are inactivated from further use to prevent unwanted mineralization [31, 32]. Indeed, *Ahsg* is known to have little effect on mineral crystal growth once a nucleus is formed [124].

In addition, mechanical measurements in the form of NI as well as micro-tensile measurements are performed to characterize the mechanical behaviors of *Ahsg* (-/-) and *Ahsg* (+/+) tissue types (**Figure 4.18**). In the case of NI, each sample is indented a total of 10 indents transverse to the tangential-longitudinal plane. The moduli of *Ahsg* (+/+) samples are found to be 32.5 GPa ± 0.813, whereas the null mutant are found to be 29.0 GPa ± 0.832. The respective hardness values were 1.26 GPa ± 0.0613 and 1.26 GPa ± 0.0362 for wildtype and null mutant samples (**Figure 4.18**). (Both the indentation moduli and hardness values are not significantly different (P=0.122, P=0.647, respectively)) (**Table 4.7**. Additionally, samples from *Ahsg* (+/+) and *Ahsg* (-/-) animals are measured under tension until failure in physiological wet conditions. A total of 10 measurements for each genotype are averaged. The elastic moduli of *Ahsg* (+/+) samples are found to be 25.4 GPa ± 3.22 and 16.2 GPa ± 3.10 for *Ahsg* (-/-) samples. UTS values of *Ahsg* (+/+) and *Ahsg* (-/-) samples are found to be 44.5 MPa ± 6.22 and 34.4 MPa ± 3.78, respectively (**Figure 4.18**). (The differences between the *Ahsg* (+/+) and *Ahsg* (-/-) are not significantly different (P=0.108, P=0.334, for the tensile moduli and UTS, respectively)) (**Table 4.7**). Using synchrotron X-ray diffraction, the D period of collagen
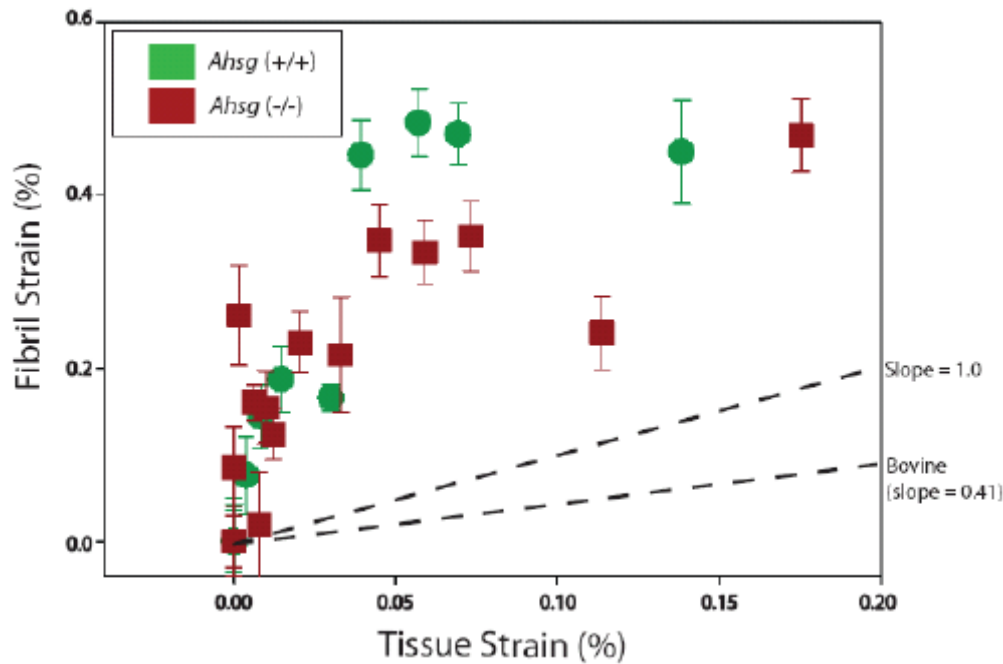
Figure 4.19 Fibril versus tissue strain measurements via in situ X-ray diffraction
Samples were measured with synchrotron radiation coupled with a micro-tensile apparatus to determine the amount of strain contributed by the collagenous fibrils between Ahsg (+/+) and Ahsg (-/-) samples (dashed lines are guides for the eye).

molecules in the fibril are measured and the deformation in each sample is tracked by following the positions of the diffraction peaks which allowed for a measurement of the fibril strain (**Figure 4.19**) (**Chapter 3.3.5**). When normalized with respect to the tissue strains of the sample, we find little differences in strain between the populations of *Ahsg* (+/+) and *Ahsg* (-/-) samples.

Tissue strains in both *Ahsg* (+/+) and *Ahsg* (-/-) samples are observed to occur within a small range of 0-0.2% before failure. No plastic deformation is observed in either sample types before failure. The normalized fibril-tissue strains of *Ahsg* samples

Table 4.7. Summary of Mechanical Measurements of Ahsg Measurements from micro-tensile and NI are performed to compare materials properties in Ahsg (-/-) and Ahsg (+/+) samples

Genotype	Micro-Tensile		Nanoindentation	
	E [GPa]	Strength [MPa]	E_i [GPa]	Hardness [GPa]
Ahsg (+/+)	25.4 ± 3.22	44.5 ± 6.22	32.5 ± 1.63	1.26 ± 0.123
Ahsg (-/-)	16.2 ± 3.09	34.4 ± 3.78	29.0 ± 1.66	1.26 ± 0.0724

tend to be $\dfrac{\varepsilon_{fibril}}{\varepsilon_{tissue}} > 1.0$ and significantly higher than values for the bovine case where

$\dfrac{\varepsilon_{fibril}}{\varepsilon_{tissue}} \sim 0.41$ [48]. This indicates that deformation behaviors of murine and bovine bones

differ considerably, while the null mutant and wildtype *Ahsg* murine samples showed the same behavior.

Histomorphometrical analysis revealed that Ahsg-deficient bones are indistinguishable from wildtype controls in terms of bone volume and bone cell numbers. However, *Ahsg*-deficient bones are found to have improved biomechanical properties in a three-point bending assay (Force to failure is 20.44 ± 5.03 in *Ahsg* (-/-) mice vs. 13.28 ± 2.16 in wildtype controls, p<0.001). This is most likely explained by the fact that Ahsg-deficient bones have an increased bone mineral content (Ash weight as a percentage of dry weight is 59.7 ± 4.7 vs. 53.0 ± 2.76, p <0.01) which is consistent with the function of *Ahsg* as a systemic inhibitor of mineralization. It is also found that the calcium to phosphate ratio in the ash of *Ahsg*-deficent bones is increased compared to wildtype controls (1.72 ± 0.05 vs. 1.64 ± 0.03, P=0.07) showing *Ahsg* has an influence on bone mineral composition.

The present data show that *Ahsg* has little effect on bone mineral or matrix quality in the cortex, but it is known to affect the growth plate (**Figure 4.15**). At the tissue level, null mutant animals possess shorter long bones (**Figure 4.14(B.)**). In comparing the lengths of the femurs in null mutant and wildtype samples, the wildtype femurs are ~50% longer than the null mutant femurs (**Figure 4.14(A.)**). This phenotype of *Ahsg* (-/-) indicates a form of dysplasia and implicates the epiphysis of long bones as an area likely to be affected by the fetuin null mutant. These differences between *Ahsg* (+/+) and *Ahsg* (-/-) samples exist specifically in the growth plate region, showing differences in

112

Table 4.8. Summary of Mineral and Tissue properties of Ahsg (-/-) and (+/+) bones
Properties of the mineral in Ahsg samples from SAXS, SAXS absorption, and Raman measurement revealing no significant differences between Ahsg (-/-) and Ahsg (+/+). (ANOVA statistical results a. P = 0.061, b. P = 0.895, c. P = 0.359, d. P = 0.462)

Sample	index	T-parameter [nm]	Avg. T-parameter [nm][a]	SAXS Transmission [counts]	Avg. SAXS Transmission [counts][b]	X-ray Attenuation Coefficients [cm^{-1}]	Avg. Attenuation coefficients[c] [cm^{-1}]	Raman ratios [PO4/Amide I]	Avg. Raman ratios [PO$_4$/Amide I][d]
Ahsg (+/+)	A	2.08 ± 0.0325		0.836 ± 0.0122		42.8 ± 3.51		10.1 ± 0.732	
	B	2.34 ± 0.0123	2.15 ± 0.0482	0.807 ± 0.00131	0.821 ± 0.00851	46.1 ± 1.16	47.0 ± 1.67	8.36 ± 0.612	9.80 ± 0.194
	C	n/a		n/a		52.3 ± 2.87		9.25 ± 0.114	
	D	2.04 ± 0.0160		0.820 ±0.0225		n/a		10.5 ± 0.324	
Ahsg (-/-)	E	2.33 ± 0.0186		0.747 ± .00794		48.2 ± 2.26		11.0 ± 0.612	
	F	2.41 ± 0.0334	2.19 ± 0.0934	0.878 ± 0.0484	0.816 ± 0.0237	28.82 ± 1.93	46.0 ± 3.17	9.26 ± 0.529	9.56 ± 0.271
	G	n/a		n/a		60.9 ± 5.49		8.03 ± 0.310	
	H	1.84 ± 0.0937		0.821 ± 0.00280		n/a		9.99 ± 0.130	

chrondrocyte organization (**Figure 4.15(A.),(B.)**). Previous work has implicated *Ahsg* as necessary for differentiation and development of chondrocytes in the growth plate [125] [126]. Staining of the epiphyseal growth plate with safranin O and toluidine blue reveal a discontinuous growth plate and cartilage islands in the *Ahsg* (-/-) samples (**Figure 4.15**). This suggests that secondary endochondral ossification is unable to proceed and the subsequent lengthening processes of long bones are inhibited. These results show that *Ahsg* has a developmental rather than a structural role in murine bone.

Ahsg is known to hinder the precipitation of calcium phosphate in blood serum and subsequently, prevent ectopic calcification of soft tissues. The influence of fetuin in bone mineralization seems, however, minimal in the present model, despite the fact that fetuin is deposited in cortical bone in fairly large amounts [127] [123]. Structural and mechanical analyses of bone material in *Ahsg* null mutant and wildtype do not reveal

significant influences from this protein and its derivatives on the material quality (**Figure 4.16**, **4.18**).

Mechanical differences in bovine and murine bones

Surprisingly, an unexpected difference in mechanical behavior is found between cortical bone of *Ahsg* bones in comparison to other available model systems, such as bovine fibrolamellar bone studied earlier. *Ahsg* murine bone appears to be stiffer and harder than bovine fibrolamellar bone, while the latter is considerably stronger than murine bone (**Figure 4.18**). Nanoindentation results indicate similarities in both indentation moduli and hardness of samples from *Ahsg* (-/-) and *Ahsg* (+/+) bones. Furthermore, micro-tensile measurements also corroborate the similar elastic moduli as well as ultimate tensile behaviors in both null mutants and wildtype (**Figure 4.21**). Fracture behaviors in both sample types also indicate similar mechanisms of brittle failure (**Figure 4.20**). The differences between samples *Ahsg* (+/+) and *Ahsg* (-/-) are not significant. The ratio of indentation moduli from bovine and *Ahsg* (+/+) mice samples

reveal, $\dfrac{E_{indentation,bovine}}{E_{indentation,Ahsg(+/+)}} \approx 0.71$, while the ratio of hardness and strengths were found to

be, $\dfrac{H_{indentation,bovine}}{H_{indentation,Ahsg(+/+)}} \approx 0.54$ and $\dfrac{\sigma_{uts,bovine}}{\sigma_{uts,Ahsg(+/+)}} \approx 1.7$, respectively. This suggests that

bovine fibrolamellar bone is indeed a less stiff and hard material compared to murine cortical bone. Specifically, remarkable differences in this context are results obtained by synchrotron X-ray diffraction and in-situ mechanical deformation measurements. Bovine cortical bone [97] consistently show a smaller strain in collagen fibrils than in the total tissue, indicating a shearing mechanism between fibrils mediated by a softer organic matrix connecting the fibrils [65]. In the *Ahsg* mouse, this deformation behavior is not observed in either the null mutant nor wildtype cases (**Figure 4.19**). Specifically, both *Ahsg* (+/+) and *Ahsg* (-/-) samples fracture at strains of ~0.2% tissue strains, unlike the ~2% tissue strains observed in bovine fibrolamellar bone. Moreover, during deformation
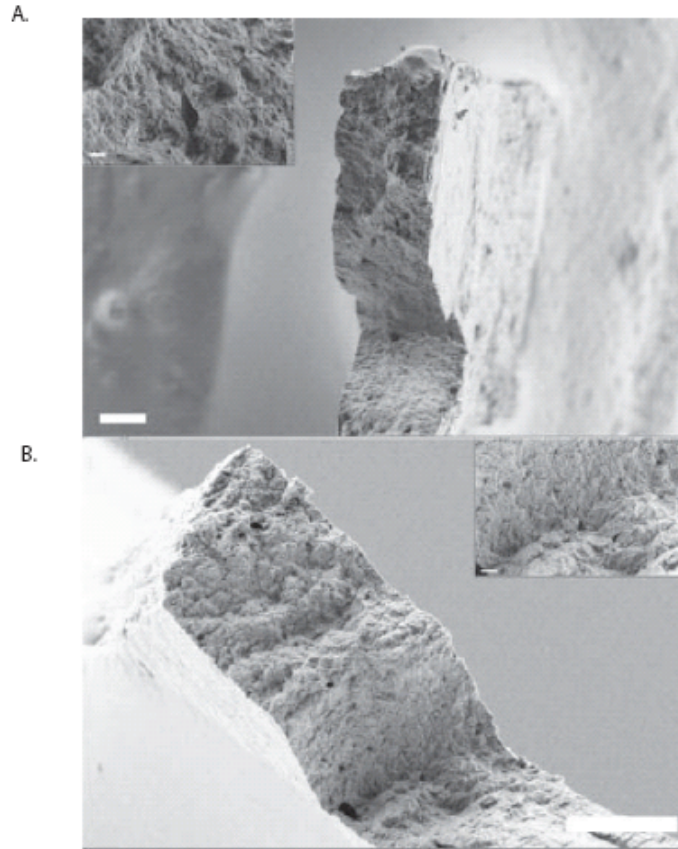
Figure 4.20 Fracture surfaces of Ahsg (-/-) and Ahsg (+/+) bone samples (A). Representative Ahsg (+/+) fracture surface showing evidence of brittle failure (B). Representative Ahsg (-/-) fracture surface revealing similar fracture behavior in (A).

the collagen fibrils seemed to strain more rather than the tissue as a whole, unlike the case of bovine cortex where the opposite was found (**Figure 4.19**). This effect can only be explained if the fibrils themselves are connected by a stiffer and comparably undeformable matrix. The only logical explanation for this is higher mineralization of the matrix between the fibrils in *Ahsg* bone. The origin of this effect may reside in the fact that murine cortical bone is essentially oriented woven bone which is known to have higher mineral contents [128] [76]. This would suggest that murine bone due to its woven character has larger amounts of extra-fibrillar mineral, making the matrix effectively stiffer than the mineralized collagen fibrils and the bone material harder and less extensible (**Figure 4.21**). This indicates that bone microstructure itself differs significantly in murine compared to bovine bone, leaving open the possibility that these differences are not unique to these
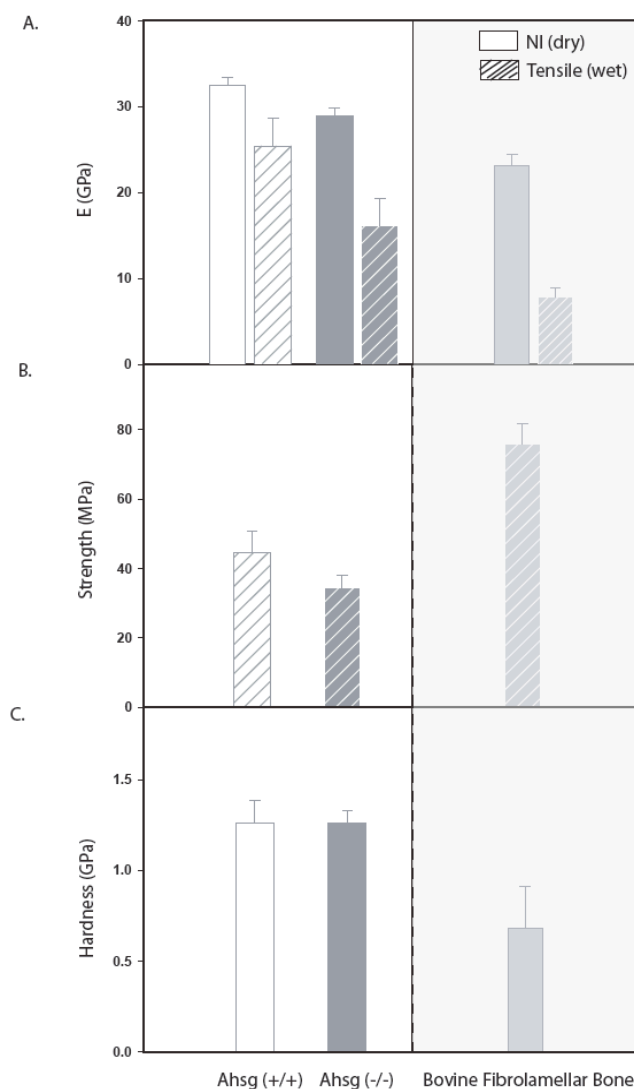
Figure 4.21 Mechanical measurements of Ahsg (-/-) and Ahsg (+/+) bone compared to bovine fibrolamellar bone. (**A.**) Nanoindentation (n=80) and microtensile (n=20) measurements of the elastic moduli of the wildtype and mutant samples (in comparison with similar measuremens on bovine fibrolamellar bone) (**B.**) Ultimate tensile strengths of Ahsg (+/+) and Ahsg (-/-) samples as well as (C.) hardness measurements of Ahsg (+/+), Ahsg (-/-), and bovine fibrolamellar samples.

two specific model systems. By retaining primary bone, murine cortical bone inadvertently possesses more woven than lamellar bone type. This more mineralized bone exists as extra-fibrillar mineral in the tissue and is highly oriented. As a consequence, the shearing behavior of mineralized collagen fibrils does not occur as a result of the surrounding stiff extra-fibrillar matrix, making examination of bone NCPs and their effects on bone deformation behavior complicated.

116

In this chapter, the strategies utilized by Nature in constructing the material bone to withstand the normal mechanical demands for day-to-day functionality as well as accommodating the necessary biological components that actively participate in growth, development, and wound healing are revealed. This work on bovine fibrolamellar bone has elucidated some of these architectural strategies in making bone more defect- and fracture- resistant. From understanding that the degree of anisotropy in bone tissue is highly regulated and is directly affected by both the orientation of collagen fibers and the interfacial boundaries to an organization scheme utilizing cooperative, hierarchical structures where each length-scale cooperatively distributes excess force away from sensitive constituents [97], bone has evolved as a tissue able to cope with the diverse functionalities which subject it to extreme mechanical conditions. Bone also must contend to spatial constraints as well, incorporating the aforementioned organization schemes with its components as well as integrating the biological components that maintain and regulate these strategies.

In an effort to understand mechanisms of biological control in bone materials properties as well as structure are regulated, gene frameworks are examined and their protein products are specifically removed and the tissues compared with their wildtype analogs. This work deals with determining which gene frameworks are vital to sustaining bone material quality and performance. Several types of long bones from mice mutant strains bred with deletions of specific genes and subsequently, their protein products, are compared to their respective wildtype analogs to determine phenotypical differences. From the Shn3 (-/-) mice model, where negative regulators of the TGF-β pathway are inactivated, osteoblastic activity is unchecked and appears to effectively increase the amount of mineral in bone [52]. To the NF1 (-/-) mice model, a disruption in the organization of the extracellular matrix during its embryonal stages introduces a defect in its mineralized tissues present throughout the lifespan of the organism. The *Ahsg* (-/-) mice model, where all vascular tissues are subject to nonspecific ectopic mineralization and specifically, the growth plate in long bones is disorganized so longitudinal tissue growth is inhibited. All the aforementioned mice models provide systems to study specific perturbations of biological processes to understand the necessity of particular genes, proteins, and regulatory molecules that orchestrate the mechanisms used in

maintaining the materials properties of "normal" mineralized tissue. These investigations seemingly are paradoxical to the approach mentioned in the beginning of this chapter, where strategies are investigated in making bone stronger and tougher. The latter part of this chapter, genes are deleted or mutated to inhibit strength and toughness in bone in order to understand the cascade of control that is spread throughout an organism. In summary, as with all tissues, the complexity in bone as an organ represented by the diverse and varied biological processes that maintain organization, as well as growth and development, disruption in one gene invariably can and often cause a disruption in another organ too. These questions indicate that there is still much to be done to fully understand biological control of bone growth, development, and regeneration.

5   Concluding Remarks

The origins of form have occupied early scientific thought for two centuries. This fascination in form is itself the basis of the modern classification system that catalogues all life, used to recognize the diversity of forms and organize lineages by these unique features. Form has given organisms function. Specifically, organisms are themselves dominated by characteristic structures and utilized for specialized tasks such as protection, support, or growth. Such examples of these structures are observed in birds, turtles, and sharks, in their feathers, shells, and teeth—materials in these respective organisms which have come to represent the organisms themselves. Not only do these materials influence functionality (i.e. feathers=flight, shells=defense, teeth=predation), these features confer an ability to provide an ever so slight advantage in an organism's fitness.
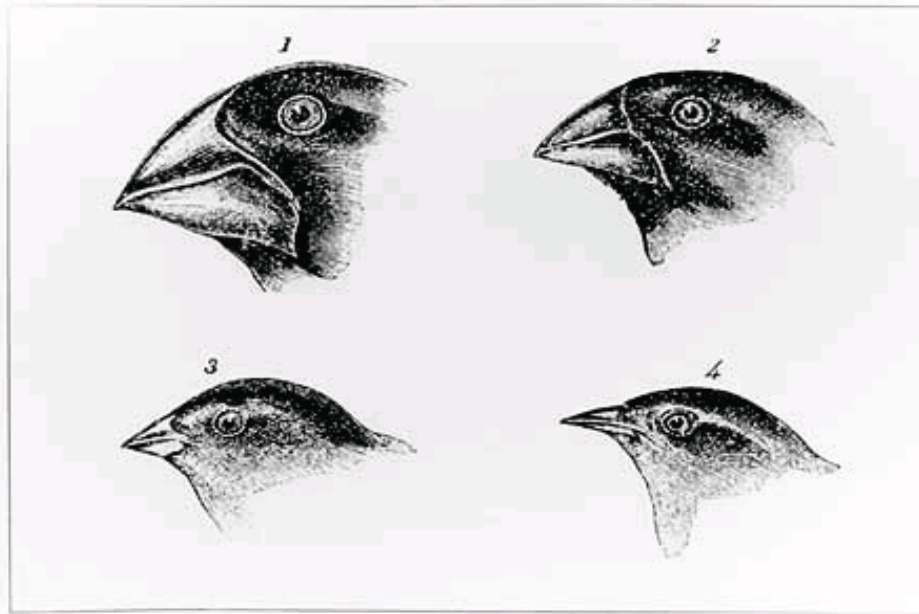
Figure 5.1 Darwin's sketches of finches' beaks during his stay in the Galapagos Islands Speciation, in the form of beak morphology, is observed from the different islands of the Galapagos Islands. Recent evidence points to a specific modification of the Calmoudlin gene as the source of this variation in beak morphology [Adapted from Darwin On the Origin of Species 1859].

Furthermore, these features are not static and do undergo natural changes. As observed in Darwin's finches, functionality is itself an environmental pressure in natural selection, often manifesting itself as an optimization process in biological materials (**Figure 5.1**) [129, 130]. Simply, function also induces form. Whether it is making the material harder, tougher, more elastic, or resilient, optimization of these materials by natural selection takes hold at the lowest length-scales. In the previous pages, techniques have been employed to examine the micro- and nano- structures which provide these exceptional materials and mechanical properties present in bone.

Bone's extraordinary materials properties include high strength to fracture, tissue toughness, as well as the ability to remodel and heal. In several attempts to emulate these bone's materials properties, many groups have tried to reconstitute bone-like materials from constituent bone components, only to realize that organic matrix assembly, mineralization in collagen fibrils, and cellular proliferation processes are multifaceted and far complex [49, 86] [83]. The limitations encountered in these studies stem from the lack of understanding on the hierarchical structures that assemble to create the material bone. In an attempt to elucidate the structures involved in the hierarchical architecture and their behaviors, this dissertation presents structure-function relationships in the material bone at the micro- and nano- length-scales.

5.1   Summary

This work aims at investigating the material bone and the origins of its mechanical behaviors at multiple length-scales. In this detailed study, bone's mechanical behavior has been attributed directly to the hierarchical architecture—structuring its constituent elements over multiple length-scales to incorporate strengthening mechanisms into the composite material. At the level of the whole tissue, bone is surrounded by epithelial and connective tissues that act as a layer of compliance, reducing the mechanical load bone experiences. This load is transferred to the lower length-scales of bone. At the micro-scale of cortical bone, the level of fibrolamellar units, weak interfaces modulate the strength and stiffness of the material. Furthermore, into the nano-scale, the shearing between mineral platelets is found to dissipate mechanical energy such that the

stiff platelets are not exposed to excess forces. In examining these mechanical strategies in bone in more detail with mechanical and structural probes, the following mechanical behaviors at the micro- and nano- length-scales in the hierarchical bone structure are found:

- a remarkable degree of mechanical anisotropy is mediated by weak, organic interfaces in bone such that the anisotropy of the elastic modulus and strength are found to be $\frac{1}{8}$ and $\frac{1}{7}$ in dry conditions and $\frac{1}{15}$ and $\frac{1}{20}$ in wet conditions, respectively

- scaling effects in fibrolamellar bone along the main bone axis reveal an increase in both $E_{\parallel}$ and $UTS_{\parallel}$ with increasing sample size, but in the orthogonal direction $E_{\perp}$ is found to increases and $UTS_{\perp}$ is constant with increasing sample dimension

- a load transfer scheme is found to have a ratio of strain in proportions of 12: 5: 2 whereby strain is distributed to the tissue: fibrils: mineral platelets, respectively, to prevent irreversible damage leading to catastrophic tissue failure

- mineralization defects result from the deletion of the neurofibromin gene NF1 such that unmineralized voids fill the cortical bone space due to disruption of the signaling and differentiation of osteoblastic cells

- the gene deletion of α-HS glycoprotein/fetuin-α is found to have no defects in its bone materials properties, but results in a lengthening defect in its long bones and is a result of a disruption in transport of phosphate mineral to mineralization centers

- the development of bone in bovine and murine model systems are vastly different, contributing to divergent mineral deposition and remodeling processes–resulting in unexpected variations in materials properties as well as mechanical behaviors in the material bone in the bovine and murine models

From these observed mechanical behaviors, the role of specific structures involved in the deformation mechanisms of bone in bovine and murine model systems is delineated and better understood. Specifically, this work implicates structures in the hierarchical bone architecture that actively provide mechanical compliance in bone tissue. These structures, like the weak, organic interfaces, contribute directly to the extreme mechanical anisotropy found in fibrolamellar bone as well as the effective load transfer from the tissue to the fibril and eventually, the mineral platelet. By critically examining these structures and their deformation behaviors, the mechanical behavior of bone is understood.

5.2   Future work

Many structural questions regarding compact bone have been answered by this dissertation, but there are questions about the material bone that have also arisen from this work. These questions include further investigating the roles of non-collagenous protein in mineralized tissues, the mechanical roles of the lamellar and woven regions in bone, and as well as the specific components that are necessary in reconstructing a material with bone-like materials properties. The following section expands on some of these questions and the work required to properly address them.

- On understanding the role of non-collagenous proteins in bone, the methodology shown in this dissertation in deciphering the gene-function relationships in mineralized tissues, mice knockout models are utilized, to delineate the roles of NCPs in bone. Specifically, necessary NCP proteins required in bone homeostasis are examined for effects in the materials properties of bone tissue. Using methods established in this dissertation, as

well as methods probing beyond the micro- and nano- length-scales are used, such as molecular methods to elucidate the mechanisms in which these NCPs affect the materials properties at these small length-scales.

- On reconciling the differences between lamellar and woven bone regions, high-resolution methods must be utilized. The roles of lamellar and woven bone regions *in vivo* remain undetermined. Through uses of high-resolution scanning SAXS as well as atom probe-based microscopy techniques, the ability to examine the nano-scale structures of woven and lamellar bone as well as probe the mineral-matrix interactions in these respective structures can provide more organizational and structural information on these regions in the material bone. These experiments would aid in understanding the roles of these structures in bone tissue. These high-resolution techniques would also reveal the effects of growth and development on these structures in the material bone at the nano-scale.

- On creating a nano-structured bone-like material, organizational schemes observed in Nature's material can be used as a template for ordered, mineralized tissues. Recent work by various groups has shown the ability to synthesize mineralized tissue with a similar composition and structure found in native mineralized tissue. The mechanical behaviors of these synthetic mineralized tissues are, at best, competent to undergo the minimal mechanical loads experienced by native tissues. To endow synthetic materials with the same strengthening mechanisms found in native materials, these synthetic materials need to be structured at the lowest length-scales of its structure. Utilizing current nano-patterning techniques, like electro-spinning methods, these synthetic tissues are structured from the nano-scale and up, organizing mineral components to effectively interact with mechanical loads. This strategy attempts to create structurally and mechanically competent synthetic materials by organizing the constituent elements in a similar manner found in Nature.

Materials in Nature optimize mechanical behavior from use of organizational and structural schemes to pack constituent elements efficiently and effectively. By implementing these lessons learned from these structure and function relationships, novel man-made materials are made stronger and tougher with these architectural schemes inspired from Nature's materials. More questions remain since the material bone itself is not a static tissue. Its capacity to repair and grow is often ignored, but is an aspect that will keep bone as a material revisited by many for years to come.

6   Appendix

6.1   Index of Figures

6.2   Index of Tables

6.3 Index of Equations

6.4 Index of Publications

1.   HS Gupta, J Seto, W Wagermaier, P Zaslansky, P Boesecke, P Fratzl "Cooperative deformation of mineral and collagen at the nanoscale" Proc Nat Acad Sci USA 2006,103(47), 17741.

2.   J Seto, HS Gupta, P Zaslansky, HD Wagner, P Fratzl "Tough lessons from bone: extreme mechanical anisotropy at the mesoscale" Adv. Func. Mat. 2008, 18(13), 1905.

3.   HS Gupta, J Seto, S Krauss, P Boesecke, HRC Screen "In-situ multilevel analysis of viscoelastic deformation mechanisms in tendon collagen" J. Structural Biology 2010, 169, 183-191.

4.   N Nassif, F Gobeaux, J Seto E Belamie, P Davidson, P Panine, G Mosser, P Fratzl, MM Giraud-Guille "Self-assembled collagen-apatite matrix with bone-like hierarchy" Chem Mater 2010, accepted.

5.   J Seto, HS Gupta, S Krauss, JWC Dunlop, M Kerschnitzki, A Masic, P Zaslansky, T Schinke, P Catala, B Busse, C Schaefer, P Boesecke, P Fratzl, W Jahnen-Dechent "The plasma protein fetuin-A/α2HS-glycoprotein is a physiologic regulator of bone mineralization" in preparation.

7   Bibliography

1.   Fratzl, P. and R. Weinkamer, *Nature's hierarchical materials.* Progress in Materials Science, 2007. **52**(8): p. 1263-1334.

2.   Andrews, E.W. and L.J. Gibson, *The influence of cracks, notches and holes on the tensile strength of cellular solids.* Acta Materialia, 2001. **49**(15): p. 2975-2979.

3.   Currey, J.D., *Bones.* 2002, Princeton: Princeton University Press.

4.   Jurist, J.M., Foltz A.S., *Human ulnar bending stiffness, mineral content, geometry and strength.* Journal of Biomechanics, 1977. **10**: p. 455-459.

5.   Currey, J.D., *The mechanical consequences of variation in the mineral content of bone.* Journal of Biomechanics, 1969. **2**: p. 1-11.

6.   Burr, D.B.a.M., R.B., *The effects of composition, structure and age on the torsional properties of the human radius.* Journal of Biomechanics, 1983. **16**(8): p. 603-608.

7.   Evans, F.G.L.H.R., *Stresscoat deformation studies of the femur under static vertical loading.* Anatomical Record, 1948. **100**(2): p. 159-190.

8.   Reilly, D.T. and A.H. Burstein, *Elastic and Ultimate Properties of Compact Bone Tissue.* Journal of Biomechanics, 1975. **8**(6): p. 393-&.

9.   Cowin, S., *Bone Mechanics Handbook.* 2nd ed. 2001, New York: CRC Press.

10.   Rubin, C., Gross T., Qin Y., Fritton S., Guilak F., McLeod K., *Differentiation of the bone-tissue remodeling response to axial torsional loading in the turkey ulna.* Journal of Bone and Joint Surgery-American Volume, 1996. **78**: p. 1523-33.

11.   Liu, D.M., S. Weiner, and H.D. Wagner, *Anisotropic mechanical properties of lamellar bone using miniature cantilever bending specimens.* Journal of Biomechanics, 1999. **32**(7): p. 647-654.

12.   Weiner, S. and H.D. Wagner, *The material bone: Structure mechanical function relations.* Annual Review of Materials Science, 1998. **28**: p. 271-298.

13.   Ramshaw, J.A.M., N.K. Shah, and B. Brodsky, *Gly-X-Y tripeptide frequencies in collagen: A context for host-guest triple-helical peptides.* Journal of Structural Biology, 1998. **122**(1-2): p. 86-91.

14. Shoulders, M.D. and R.T. Raines, *Collagen Structure and Stability.* Annual Review of Biochemistry, 2009. **78**: p. 929-958.

15. Hodge, A.J., Petruska J.A., *Recent studies with the electron microscope on ordered agregates of the tropocollagen macromolecule.* Aspects of Protein Structure, ed. G.N. Ramachandran. 1963, New York: Academic Press.

16. Hulmes, D.J.S. and A. Miller, *Quasi-Hexagonal Molecular Packing in Collagen Fibrils.* Nature, 1979. **282**(5741): p. 878-880.

17. Landis, W.J., Silver F.H., *Mineral Deposition in the Extracellular Matrices of Vertebrate Tissues: Identification of Possible Apatite Nucleation Sites on Type 1 Collagen.* Cells Tissues Organs, 2008. **189**: p. 20-24.

18. Nyman, J.S., et al., *Measurements of mobile and bound water by nuclear magnetic resonance correlate with mechanical properties of bone.* Bone, 2008. **42**(1): p. 193-199.

19. Leaver, A.G., J.T. Triffitt, and I.B. Holbrook, *NEWER KNOWLEDGE OF NON-COLLAGENOUS PROTEIN IN DENTIN AND CORTICAL BONE MATRIX.* Clinical Orthopaedics and Related Research, 1975(110): p. 269-292.

20. Hassell, J.R., Kimura J.H., Hascall V.C., *Proteoglycan core protein families.* Ann. Rev. Biochem, 1986. **55**: p. 539-67.

21. Iozzo, R.V., *Matrix Proteoglycans: From Molecular Design to Cellular Function.* Annual Review of Biochemistry, 1998. **67**: p. 609-52.

22. Lamoureux, F., Baud'huin M., Duplomb L., Heymann D., Redini F., *Proteoglycans: key partners in bone cell biology.* BioEssays, 2007. **29**(8): p. 758-771.

23. Heinegard D., O.A., *Structure and biology of cartilage and bone matrix noncollagenous macromolecules.* FASEB, 1989. **3**: p. 2042-2051.

24. Boskey, A., *Mineral-Matrix Interactions in Bone.* Clinical Orthopaedics and Related Research, 1992. **281**: p. 244-274.

25. Hunter, G.K., C.L. Kyle, and H.A. Goldberg, *MODULATION OF CRYSTAL-FORMATION BY BONE PHOSPHOPROTEINS - STRUCTURAL SPECIFICITY OF THE OSTEOPONTIN-MEDIATED INHIBITION OF HYDROXYAPATITE FORMATION.* Biochemical Journal, 1994. **300**: p. 723-728.

26. Gordon, J.A.R., et al., *Bone sialoprotein expression enhances osteoblast differentiation and matrix mineralization in vitro.* Bone, 2007. **41**(3): p. 462-473.

27. Tye, C.E., et al., *Delineation of the hydroxyapatite-nucleating domains of bone sialoprotein.* Journal of Biological Chemistry, 2003. **278**(10): p. 7949-7955.

28.   Sodek, J., B. Ganss, and M.D. McKee, *Osteopontin.* Critical Reviews in Oral Biology & Medicine, 2000. **11**(3): p. 279-303.

29.   Steitz, S.A., et al., *Osteopontin inhibits mineral deposition and promotes regression of ectopic calcification.* American Journal of Pathology, 2002. **161**(6): p. 2035-2046.

30.   Boskey, A.L., et al., *Growth plate proteins and biomineralization*, in *Growth Plate*, I.M. Shapiro, B. Boyan, and H.C. Anderson, Editors. 2002, I O S Press: Amsterdam. p. 139-149.

31.   Zappone, B., et al., *Effect of Ca2+ ions on the adhesion and mechanical properties of adsorbed layers of human osteopontin.* Biophysical Journal, 2008. **95**(6): p. 2939-2950.

32.   Fantner, G.E., et al., *Nanoscale ion mediated networks in bone: Osteopontin can repeatedly dissipate large amounts of energy.* Nano Letters, 2007. **7**(8): p. 2491-2498.

33.   Carrillo, F., et al., *Nanoindentation of polydimethylsiloxane elastomers: Effect of crosslinking, work of adhesion, and fluid environment on elastic modulus.* Journal of Materials Research, 2005. **20**(10): p. 2820-2830.

34.   Fantner, G.E., et al., *Sacrificial bonds and hidden length dissipate energy as mineralized fibrils separate during bone fracture.* Nature Materials, 2005. **4**(8): p. 612-616.

35.   Frost, H., *The bone dynamics in osteoporosis and osteomalacia*. The Henry Ford Hospital monographs. 1966: C.C. Thomas.

36.   Weiner, S. and P.A. Price, *DISAGGREGATION OF BONE INTO CRYSTALS.* Calcified Tissue International, 1986. **39**(6): p. 365-375.

37.   Fratzl, P., et al., *MINERAL CRYSTALS IN CALCIFIED TISSUES - A COMPARATIVE-STUDY BY SAXS.* Journal of Bone and Mineral Research, 1992. **7**(3): p. 329-334.

38.   Rinnerthaler, S., et al., *Scanning small angle X-ray scattering analysis of human bone sections.* Calcified Tissue International, 1999. **64**(5): p. 422-429.

39.   Tesch, W., et al., *Orientation of mineral crystallites and mineral density during skeletal development in mice deficient in tissue nonspecific alkaline phosphatase.* Journal of Bone and Mineral Research, 2003. **18**(1): p. 117-125.

40.   Arnold, W., *The nature of precipitated calcium phosphates.* Trans. Faraday Soc., 1950. **46**: p. 1061-1072.

41. Brown, W.E., *Octacalcium phosphate and hydroxyapatite.* Nature, 1962. **196**: p. 1048-1050.

42. Brown, W.E., Smith J.P., Lehr J.R., Frazier A.W., *Crystallographic and chemical reactions between octacalcium phosphate and hydroxyapatite.* Nature, 1962. **196**: p. 1050-1055.

43. Herman, H., Dallegane M.J., *The main mineral constituent of bone and teeth.* Arch. oral Biol., 1961. **5**: p. 137-144.

44. Takano, Y., et al., *Elastic anisotropy and collagen orientation of osteonal bone are dependent on the mechanical strain distribution.* Journal of Orthopaedic Research, 1999. **17**(1): p. 59-66.

45. Hasegawa, K., C.H. Turner, and D.B. Burr, *CONTRIBUTION OF COLLAGEN AND MINERAL TO THE ELASTIC-ANISOTROPY OF BONE.* Calcified Tissue International, 1994. **55**(5): p. 381-386.

46. Giraudguille, M.M., *TWISTED PLYWOOD ARCHITECTURE OF COLLAGEN FIBRILS IN HUMAN COMPACT-BONE OSTEONS.* Calcified Tissue International, 1988. **42**(3): p. 167-180.

47. Ascenzi, A. and E. Bonucci, *A QUANTITATIVE INVESTIGATION OF BIREFRINGENCE OF OSTEON.* Acta Anatomica, 1961. **44**(3): p. 236-&.

48. Gourrier, A., et al., *Scanning X-ray imaging with small-angle scattering contrast.* Journal of Applied Crystallography, 2007. **40**: p. S78-S82.

49. Cui, W.U., et al., *In situ growth of hydroxyapatite within electrospun poly(DL-lactide) fibers.* Journal of Biomedical Materials Research Part A, 2007. **82A**(4): p. 831-841.

50. Zioupos, P., et al., *EXPERIMENTALLY DETERMINED MICROCRACKING AROUND A CIRCULAR HOLE IN A FLAT-PLATE OF BONE - COMPARISON WITH PREDICTED STRESSES.* Philosophical Transactions of the Royal Society of London Series B-Biological Sciences, 1995. **347**(1322): p. 383-396.

51. Balooch, G., et al., *TGF-beta regulates the mechanical properties and composition of bone matrix.* Proceedings of the National Academy of Sciences of the United States of America, 2005. **102**(52): p. 18813-18818.

52. Jones, D.C., et al., *Regulation of adult bone mass by the zinc finger adapter protein Schnurri-3.* Science, 2006. **312**(5777): p. 1223-1227.

53. Vashishth, D., *Small animal bone biomechanics.* Bone, 2008. **43**(5): p. 794-797.

54. Kolanczyk, M., et al., *Multiple roles for neurofibromin in skeletal development and growth.* Human Molecular Genetics, 2007. **16**(8): p. 874-886.

55.   Kolanczyk, M., et al., *Modelling neurofibromatosis type 1 tibial dysplasia and its treatment with lovastatin.* Bmc Medicine, 2008. **6**: p. -.

56.   Elefteriou, F., et al., *Skeletal Abnormalities in Neurofibromatosis Type 1: Approaches to Therapeutic Options.* American Journal of Medical Genetics Part A, 2009. **149A**(10): p. 2327-2338.

57.   Price, P.A., T.M.T. Nguyen, and M.K. Williamson, *Biochemical characterization of the serum fetuin-mineral complex.* Journal of Biological Chemistry, 2003. **278**(24): p. 22153-22160.

58.   Price, P.A., et al., *Evidence for a serum factor that initiates the re-calcification of demineralized bone.* Journal of Biological Chemistry, 2004. **279**(18): p. 19169-19180.

59.   Toroian, D., J.E. Lim, and P.A. Price, *The size exclusion characteristics of type I collagen - Implications for the role of noncollagenous bone constituents in mineralization.* Journal of Biological Chemistry, 2007. **282**(31): p. 22437-22447.

60.   Toroian, D. and P.A. Price, *The essential role of fetuin in the serum-induced calcification of collagen.* Calcified Tissue International, 2008. **82**(2): p. 116-126.

61.   Schafer, C., et al., *The serum protein alpha(2)-Heremans-Schmid glycoprotein/fetuin-A is a systemically acting inhibitor of ectopic calcification.* Journal of Clinical Investigation, 2003. **112**(3): p. 357-366.

62.   Jahnen-Dechent, W., et al., *Mineral chaperones: a role for fetuin-A and osteopontin in the inhibition and regression of pathologic calcification.* Journal of Molecular Medicine-Jmm, 2008. **86**(4): p. 379-389.

63.   Hull D, C.T., *An Introduction to Composite Materials.* 2nd ed. 1996, Cambridge: Cambridge University Press.

64.   Jager, I. and P. Fratzl, *Mineralized collagen fibrils: A mechanical model with a staggered arrangement of mineral particles.* Biophysical Journal, 2000. **79**(4): p. 1737-1746.

65.   Gao, H.J., et al., *Materials become insensitive to flaws at nanoscale: Lessons from nature.* Proceedings of the National Academy of Sciences of the United States of America, 2003. **100**(10): p. 5597-5600.

66.   Ji, B.H., H.J. Gao, and K.J. Hsia, *How do slender mineral crystals resist buckling in biological materials?* Philosophical Magazine Letters, 2004. **84**(10): p. 631-641.

67.   Peterlik, H., et al., *From brittle to ductile fracture of bone.* Nature Materials, 2006. **5**(1): p. 52-55.

68.   McCrum NG, B.C., Bucknall CB, *Principles of Polymer Engineering*. 2nd ed. 1999, Oxford: Oxford University Press.

69.   Kruzic, J.J., et al., *Mechanistic aspects of in vitro fatigue-crack growth in dentin.* Biomaterials, 2005. **26**(10): p. 1195-1204.

70.   Koester, K.J., J.W. Ager, and R.O. Ritchie, *The true toughness of human cortical bone measured with realistically short cracks.* Nature Materials, 2008. **7**(8): p. 672-677.

71.   Zimmermann, E.A., et al., *Mixed-mode fracture of human cortical bone.* Biomaterials, 2009. **30**(29): p. 5877-5884.

72.   Mercer, C., R.Z. Wang, and A.G. Evans, *An investigation of the inelastic deformation of cortical bone.* Advanced Engineering Materials, 2005. **7**(8): p. 719-723.

73.   Ebacher, V. and R.Z. Wang, *A Unique Microcracking Process Associated with the Inelastic Deformation of Haversian Bone.* Advanced Functional Materials, 2009. **19**(1): p. 57-66.

74.   Griffith, A., *The phenomena of rupture and flow in solids.* Phil. Trans. Roy. Soc. London, 1920. **A221**: p. 163-168.

75.   Zioupos, P., M. Gresle, and K. Winwood, *Fatigue strength of human cortical bone: Age, physical, and material heterogeneity effects.* Journal of Biomedical Materials Research Part A, 2008. **86A**(3): p. 627-636.

76.   Currey, J.D., *The many adaptations of bone.* Journal of Biomechanics, 2003. **36**(10): p. 1487-1495.

77.   Taylor, D., J.G. Hazenberg, and T.C. Lee, *Living with cracks: Damage and repair in human bone.* Nature Materials, 2007. **6**(4): p. 263-268.

78.   Nalla, R.K., et al., *Role of microstructure in the aging-related deterioration of the toughness of human cortical bone.* Materials Science & Engineering C-Biomimetic and Supramolecular Systems, 2006. **26**(8): p. 1251-1260.

79.   Nicolella, D.P., et al., *Osteocyte lacunae tissue strain in cortical bone.* Journal of Biomechanics, 2006. **39**(9): p. 1735-1743.

80.   Al-Sawalmih, A., et al., *Microtexture and Chitin/Calcite Orientation Relationship in the Mineralized Exoskeleton of the American Lobster.* Advanced Functional Materials, 2008. **18**(20): p. 3307-3314.

81.   Galileo, G., *Discourses and mathematical demonstrations concerning two new sciences*. 1638, Madison, WI: University of Wisconsin Press.

82. Wolff, J., *Die Lehre von der functionellen Knochengestalt*. Das Gesetz der Transformation der Knochen. 1868, Berlin: Universitaet zu Berlin.

83. Gentleman, E., et al., *Comparative materials differences revealed in engineered bone as a function of cell-specific differentiation*. Nature Materials, 2009. **8**(9): p. 763-770.

84. Burg, K.J.L., S. Porter, and J.F. Kellam, *Biomaterial developments for bone tissue engineering*. Biomaterials, 2000. **21**(23): p. 2347-2359.

85. Jang, J.H., O. Castano, and H.W. Kim, *Electrospun materials as potential platforms for bone tissue engineering*. Advanced Drug Delivery Reviews, 2009. **61**(12): p. 1065-1083.

86. Hutmacher, D.W. and S. Cool, *Concepts of scaffold-based tissue engineering-the rationale to use solid free-form fabrication techniques*. Journal of Cellular and Molecular Medicine, 2007. **11**(4): p. 654-669.

87. Matthews, S.J.E., V.S. Nikolaou, and P.V. Giannoudis, *Innovations in osteosynthesis and fracture care*. Injury-International Journal of the Care of the Injured, 2008. **39**(8): p. 827-838.

88. Huiskes, R., *If bone is the answer, then what is the question?* Journal of Anatomy, 2000. **197**: p. 145-156.

89. Krauss, S., et al., *Inhomogeneous fibril stretching in antler starts after macroscopic yielding: Indication for a nanoscale toughening mechanism*. Bone, 2009. **44**(6): p. 1105-1110.

90. Abe, Y., et al., *Synthesis, structures and ion-association properties of a series of Schiff base Oxidovanadium(V) complexes with 4-substituted long alkoxy chains*. European Journal of Inorganic Chemistry, 2008(13): p. 2148-2157.

91. Cheng, S., et al., *The role of collagen abnormalities in ultrasound and densitometry assessment: In vivo evidence*. Calcified Tissue International, 1999. **64**(6): p. 470-476.

92. Evans, F.G. and M. Lebow, *REGIONAL DIFFERENCES IN SOME OF THE PHYSICAL PROPERTIES OF THE HUMAN FEMUR*. Journal of Applied Physiology, 1951. **3**(9): p. 563-572.

93. Chung, S.H. and E. Mazur, *Surgical applications of femtosecond lasers*. Journal of Biophotonics, 2009. **2**(10): p. 557-572.

94. Chung, S., I. Maxwell, and E. Mazur, *Subcellular surgery and nanoneurosurgery*. 2007 Conference on Lasers & Electro-Optics/Quantum Electronics and Laser Science Conference (Cleo/Qels 2007), Vols 1-5, 2007: p. 1055-1056.

95.   Chung, S.H. and E. Mazur, *Femtosecond laser ablation of neurons in C. elegans for behavioral studies.* Applied Physics a-Materials Science & Processing, 2009. **96**(2): p. 335-341.

96.   Gupta, H.S., et al., *Nanoscale deformation mechanisms in bone.* Nano Letters, 2005. **5**(10): p. 2108-2111.

97.   Gupta, H.S., et al., *Cooperative deformation of mineral and collagen in bone at the nanoscale.* Proceedings of the National Academy of Sciences of the United States of America, 2006. **103**(47): p. 17741-17746.

98.   Nalla, R.K., et al., *Aspects of in vitro fatigue in human cortical bone: time and cycle dependent crack growth.* Biomaterials, 2005. **26**(14): p. 2183-2195.

99.   Nalla, R.K., et al., *Fracture in human cortical bone: local fracture criteria and toughening mechanisms.* Journal of Biomechanics, 2005. **38**(7): p. 1517-1525.

100.   Benecke, G., et al., *Digital image correlation shows localized deformation bands in inelastic loading of fibrolamellar bone.* Journal of Materials Research, 2009. **24**(2): p. 421-429.

101.   Oliver, W.C. and G.M. Pharr, *Measurement of hardness and elastic modulus by instrumented indentation: Advances in understanding and refinements to methodology.* Journal of Materials Research, 2004. **19**(1): p. 3-20.

102.   Rho, J.Y., et al., *Elastic properties of microstructural components of human bone tissue as measured by nanoindentation.* Journal of Biomedical Materials Research, 1999. **45**(1): p. 48-54.

103.   Ball, D.W., *Theory of Raman spectroscopy.* Spectroscopy, 2001. **16**(11): p. 32-+.

104.   Fratzl, P., et al., *ABNORMAL BONE MINERALIZATION AFTER FLUORIDE TREATMENT IN OSTEOPOROSIS - A SMALL-ANGLE X-RAY-SCATTERING STUDY.* Journal of Bone and Mineral Research, 1994. **9**(10): p. 1541-1549.

105.   Fratzl, P., et al., *Bone mineralization in an osteogenesis imperfecta mouse model studied by small-angle x-ray scattering.* Journal of Clinical Investigation, 1996. **97**(2): p. 396-402.

106.   Porod, G., *X-Ray and Light Scattering by Chain Molecules in Solution.* Journal of Polymer Science, 1953. **10**(2): p. 157-166.

107.   Fratzl, P., S. Schreiber, and A. Boyde, *Characterization of bone mineral crystals in horse radius by small-angle X-ray scattering.* Calcified Tissue International, 1996. **58**(5): p. 341-346.

108.   Zizak, I., et al., *Characteristics of mineral particles in the human bone/cartilage interface.* Journal of Structural Biology, 2003. **141**(3): p. 208-217.

109. Burstein, A.H., et al., *ULTIMATE PROPERTIES OF BONE TISSUE - EFFECTS OF YIELDING.* Journal of Biomechanics, 1972. **5**(1): p. 35-&.

110. Turner, C.H., et al., *The elastic properties of trabecular and cortical bone tissues are similar: results from two microscopic measurement techniques.* Journal of Biomechanics, 1999. **32**(4): p. 437-441.

111. Rho, J.Y. and G.M. Pharr, *Effects of drying on the mechanical properties of bovine femur measured by nanoindentation.* Journal of Materials Science-Materials in Medicine, 1999. **10**(8): p. 485-488.

112. Martin RB, B.D., *Structure, Function, and Adaptation of Compact Bone.* 1989, New York: Raven Press.

113. Haire, T.J., et al., *A comparison of porosity, fabric and fractal dimension as predictors of the Young's modulus of equine cancellous bone.* Medical Engineering & Physics, 1998. **20**(8): p. 588-593.

114. Hodgskinson, R. and J.D. Currey, *Young Modulus, Density and Material Properties in Cancellous Bone over a Large Density Range.* Journal of Materials Science-Materials in Medicine, 1992. **3**(5): p. 377-381.

115. Urban, V., et al., *Two-dimensional camera for millisecond range time-resolved small-and wide-angle X-ray scattering.* Journal of Applied Crystallography, 2003. **36**: p. 809-811.

116. Wegst, U.G.K. and M.F. Ashby, *The mechanical efficiency of natural materials.* Philosophical Magazine, 2004. **84**(21): p. 2167-2181.

117. Zok, F.W. and A. Miserez, *Property maps for abrasion resistance of materials.* Acta Materialia, 2007. **55**(18): p. 6365-6371.

118. Olsen, B.R., A.M. Reginato, and W.F. Wang, *Bone development.* Annual Review of Cell and Developmental Biology, 2000. **16**: p. 191-220.

119. Lander, E.S., et al., *Initial sequencing and analysis of the human genome.* Nature, 2001. **409**(6822): p. 860-921.

120. Ackert-Bicknell, C.L., et al., *Mouse-to-Human Strategy to Identify Bone Strength QTL Genes.* Journal of Bone and Mineral Research, 2008. **23**: p. S157-S157.

121. Rittling, S.R., et al., *Mice lacking osteopontin show normal development and bone structure but display altered osteoclast formation in vitro.* Journal of Bone and Mineral Research, 1998. **13**(7): p. 1101-1111.

122. Xu, J.F., et al., *Evidence for a prostate cancer susceptibility locus on the X chromosome.* Nature Genetics, 1998. **20**(2): p. 175-179.

123. Ashton, B.A., H.J. Hohling, and J.T. Triffitt, *PLASMA-PROTEINS PRESENT IN HUMAN CORTICAL BONE - ENRICHMENT OF ALPHA-2HS-GLYCOPROTEIN.* Calcified Tissue Research, 1976. **22**(1): p. 27-33.

124. Rochette, C.N., et al., *A Shielding Topology Stabilizes the Early Stage Protein-Mineral Complexes of Fetuin-A and Calcium Phosphate: A Time-Resolved Small-Angle X-ray Study.* Chembiochem, 2009. **10**(4): p. 735-740.

125. Szweras, M., et al., *alpha 2-HS glycoprotein/fetuin, a transforming growth factor-beta/bone morphogenetic protein antagonist, regulates postnatal bone growth and remodeling.* Journal of Biological Chemistry, 2002. **277**(22): p. 19991-19997.

126. Ishikawa, Y., et al., *FETUIN AND ALPHA-2HS GLYCOPROTEIN INDUCE ALKALINE-PHOSPHATASE IN EPIPHYSEAL GROWTH PLATE CHONDROCYTES.* Journal of Cellular Physiology, 1991. **149**(2): p. 222-234.

127. Dickson, I.R., A.R. Poole, and A. Veis, *LOCALIZATION OF PLASMA ALPHA-2HS GLYCOPROTEIN IN MINERALIZING HUMAN BONE.* Nature, 1975. **256**(5516): p. 430-432.

128. Boyde, A. and M.H. Hobdell, *Scanning Electron Microscopy of Lamellar Bone.* Zeitschrift Fur Zellforschung Und Mikroskopische Anatomie, 1969. **93**(2): p. 213-&.

129. Darwin, C., *On the Origin of Species.* 1859, London.

130. Zimmer, C., *ORIGIN On the Origin of Tomorrow.* Science, 2009. **326**(5958): p. 1334-1336.

8   Acknowledgements

This dissertation is a culmination of many enlightening interactions with participants from several continents—whose conversations and stories have made my stay in Berlin pleasureable and meaningful.

I am eternally grateful to Prof. Peter Fratzl and Dr. Himadri Gupta for their patience and tireless efforts in directing and often re-directing my science. Without their advice and confidence, this work would not be where it is today.

I have been fortunate enough to meet people who have become colleagues, friends, and confidants. I would like to send my deepest regards to Drs. Wolfgang Wagermaier, John Dunlop, Barbara Aichmayer, Damien Faivre, Oskar Paris, Richard Weinkamer, Helmut Coelfen, Nadine Nassif, Fred Wilt, Adele Boskey, Mason Dean, Admir Masic, Paul Zaslansky, Yael Politi, Nicole Gehrke, Ingo Burgert, Geoffrey Catalano, Dileep Varma, Roberto Neisa, Arun Witta, Jitendra Pandey, Steve Weiner, Julia Muhammid, Stuart Stock, Arthur Veis, Angelo Valleriani, Volker Knecht, Michaela Eder, and James Weaver.

And of course, there are more names than space to list those who have helped me along the way—Johannes Prass, Jens Baumgartner, Andre Koernig, Caroline Lukas, Magdalena Titiricci, Markus Hartmann, Markus Rueggeberg, Cecile Bidan, Matt and Laura Harrington, Krishna Kommareddy, Kevin Eckes, Antje Reinecke, Meriam Bezohora, Nicole Schreiber, Silke Karojet, Nadia Timofeeva, Brad and Elie Huang, Michael Kerschnitzski, Petra Leibner, Anke Maerton, Annemarie Martens, Ingrid Zenke, Heike Runge, Christine Pilz-Allen, Ana Heilig, Staffan Persson, Susanne Weichert, Stefanie Krauss, Claudia Lange, Anna Schenk, Khasayar Razghandi, and Kerstin Gabbe.

Lastly, I would like to acknowledge my family and Dr. Ozlem Sel for their constant reminders of where I am from and where I am headed. *Ich danke Ihnen vielmals.*